Cyclic Characterisation and Plasticity Modelling of AM30 Magnesium Alloy Extrusion

by

Ali Asghar Roostaei

A thesis
presented to the University of Waterloo
in fulfillment of the
thesis requirement for the degree of
Doctor of Philosophy
in
Mechanical and Mechatronics Engineering

Waterloo, Ontario, Canada, 2017

Examining Committee Membership

The following served on the Examining Committee for this thesis. The decision of the Examining Committee is by majority vote.

External Examiner	Yanyao Jiang Professor
Supervisor	Hamid Jahed Professor
Internal Member	Mary Wells Professor
Internal Member	Duane Cronin Professor
Internal-External Member	Marianna Polak Professor

Author’s Declaration

This thesis consists of material all of which I authored or co-authored: see Statement of Contributions included in the thesis. This is a true copy of the thesis, including any required final revisions, as accepted by my examiners.

I understand that my thesis may be made electronically available to the public.

Statement of Contributions

Presented material in this thesis; planning and performing experiments, analyzing acquired experimental and numerical data, and writing journal papers (listed below) are, in their entirety, contributions of myself as the first author. Professor Hamid Jahed, my supervisor and the only co-author of the listed papers, helped with planning experiments, discussing results and reviewing write-ups.

1. A.A. Roostaei, H. Jahed, Role of loading direction on cyclic behaviour characteristics of AM30 extrusion and its fatigue damage modelling, Materials Science and Engineering: A. 670 (2016) 26–40. doi:10.1016/j.msea.2016.05.116.

2. A.A. Roostaei, H. Jahed, Multiaxial cyclic behaviour and fatigue modelling of AM30 Mg alloy extrusion, International Journal of Fatigue. 97 (2017) 150–161. doi:10.1016/j.ijfatigue.2016.12.037.

3. A.A. Roostaei, H. Jahed, Constitutive plastic modelling of wrought magnesium alloys under general loading conditions considering asymmetry/anisotropy, submitted for publication in International Journal of Plasticity.

Abstract

Reducing fuel consumption and, thereby, greenhouse gas pollution has been the main thrust of lightweighting endeavours by transportation industries, particularly, automotive sector. Wrought magnesium alloys, being the lightest engineering alloys, are potential candidates for manufacturing automobile components. That said, more critical testing is still required to assess their mechanical and structural attributes toward new product development for a broad range of applications.

Anisotropic fatigue and cyclic behaviour of AM30 Mg alloy extrusion is investigated by performing fully-reversed strain-controlled tension-compression cyclic tests at strain amplitudes between 0.3% and 2.3%, along extrusion (ED) and transverse (TD) directions. The shapes of half-life hysteresis loops suggest the predominance of slip and twinning/de-twinning mechanisms below and above the strain amplitude of 0.5%, respectively. The twinning/de-twinning occurrence is found to be more extensive during straining along ED, which results in higher asymmetry of hysteresis loops, and thereby, higher induced mean stress. This adversely affects the fatigue resistance and yields lower number of cycles before failure in ED. Optical microscopy and texture analysis are employed to validate the findings. In addition, fracture surfaces are studied by scanning electron microscopy to identify the sources of fatigue crack initiation. Persistent slip bands (PSBs) and twin lamellae interfaces are evidenced as crack initiation sites at low and high strain amplitudes, respectively. Cracks emanated from debonded inclusion interface are also observed. Lastly, estimated fatigue life by the Smith-Watson-Topper (SWT) and Jahed-Varvani (JV) fatigue models are compared with experimental life obtained

through this study as well as the ones reported in the literature. The JV energy model is proven to yield better life predictions.

Moreover, multiaxial fatigue characteristics of AM30 Mg alloy extrusion are studied through fully-reversed strain-controlled cyclic experiments including pure torsional and combined axial-torsional at 0, 45 and 90° phase angle shifts. Under pure torsional cyclic loading, AM30 extrusion is realized to exhibit better fatigue properties than AZ31B and AZ61A extrusions, especially in low-cycle fatigue regime. Under proportional axial-torsional cyclic loading, twinning/de-twinning in axial mode results in asymmetric shear hysteresis loop. The effect of non-proportionality of biaxial loading on various aspects of material response is also examined and observed to be depending on the magnitude of axial strain amplitude. Finally, the life prediction capabilities of two critical plane models, i.e., modified SWT and Fatemi-Socie (FS), as well as JV energy-based approach are assessed, employing fatigue life data of AM30 extrusion. Correlation data between experimental and estimated lives are found to lie within narrow scatter band.

Basal-textured wrought magnesium alloys are inherently prone to mechanical twinning/de-twinning during cyclic deformation at room temperature. They, subsequently, exhibit distinctive flow curve attributes, which are impossible to describe using conventional plasticity models. A purely phenomenological plasticity model is herein proposed, in such way that accounts for various asymmetric/anisotropic aspects of cyclic flow response of wrought magnesium alloys. The proposed model entails an isotropic von Mises yield function which evolves in stress space according to a new generalized anisotropic kinematic hardening rule,

based on Ziegler's rule. The phenomenological concept of plastic moduli matrix introduced in the kinematic rule is viewed as the key factor in representing material yield/hardening behaviour in different directions. The components of this matrix can independently be calibrated by conducting uniaxial experiments along each direction. An efficient and stable numerical algorithm is developed and then coded into both MATLAB®, and user material subroutine (UMAT) to use within Abaqus®/Standard finite element software. Thereafter, model validation has been successfully done using two different types of experiments: proportional and non-proportional biaxial axial-torsional cyclic tests on AZ31B, AZ61A, and AM30 Mg alloy extrusions, and notched plate tensile loading-unloading test on AM30 extrusion.

Acknowledgments

First and foremost, I would like to sincerely thank my supervisor, Professor Hamid Jahed, for his insightful guidance and supervision.

My heartfelt gratitude goes to my family, in particular, my parents, parents-in-law, brothers and sister for their boundless love and encouragement all through my PhD career. I would like to offer my special thanks to my beautiful wife, Atekeh, whose love, patience, and inspiration have made this work possible.

I deeply appreciate the help of all my colleagues in Fatigue and Stress Analysis Lab, especially Dr. Behzad Behravesh, and Elfaitori Ibrahim for sharing their knowledge, advice, and comments.

I am also grateful to Richard Gordon, Andy Barber, Mark Kuntz, Charlie Boyle, Rick Forgett, Martha Morales, and William Penney for their technical supports.

The financial support of the Government of Ontario through Ontario Trillium Scholarship (OTS) program is also acknowledged.

To my beloved family,

My parents, Ali & Narjes

&

My dear wife, Atekeh

Table of Contents

List of Figures

List of Tables

Chapter 1

Introduction

1.1 Research motivation

In recent years, the automotive industries' commitment to reduce vehicle's weight, and thereby fuel consumption, has brought more attention to light structural metals. Other than saving energy, weight reduction reduces greenhouse gas emissions, which, in turn, contributes to the conservation of environment. Assuming the appropriate adjustment of engine and gearbox performance, diminishing vehicle's mass by 10% would bring about a saving of approximately 5% in fuel consumption [1]. Magnesium (and its alloys), being the lightest structural metal (with the density of 1.75 g/cm^3, less than steel and aluminum) has been the focal point for this increased interest [2].

AM30 Mg alloy extrusion is a rather new wrought magnesium alloy developed in 2007 [3]. Experimental studies showed that AM30 Mg alloy has superior formability compared to the commonly-used AZ31 wrought Mg alloy, making it more interesting to automotive industries due to higher productivity potential [4]. Despite this, there has been scarce experimental data on their uniaxial cyclic plastic behaviour [4,5]. More importantly, there are no multiaxial cyclic studies on AM30 Mg alloy, which is essential for future cyclic plasticity investigations.

Currently, magnesium alloys are widely being applied to automotive components used in vehicle interior, housings and trim parts [1,6]. Extending current application of wrought magnesium alloys to load-bearing components such as suspension arms requires comprehensive understanding of their plastic behaviour. Fatigue modelling is also necessary to estimate the component's life under cyclic loading conditions. To this end, an essential tool in the design procedure of magnesium components is finite element simulation, the key to its success is an accurate constitutive cyclic plasticity model. Nonetheless, available material models in commercial finite element packages cannot satisfy such accuracy requirement and thus, are not suitable for describing the unusual cyclic plastic behaviour of wrought magnesium alloys. Therefore, developing a constitutive model which closely follows the cyclic response of such alloys under general loading condition is of significance.

1.2 Research objectives

In the following, the major objectives of the present research are listed and briefly described:

1.2.1 Uniaxial and multiaxial cyclic response study of AM30 extrusion

One of the objectives of the current research is to systematically characterise the response of AM30 Mg alloy extrusion under various cyclic loading scenarios, including uniaxial tension-compression, pure torsional, and biaxial axial-torsional. For this purpose, strain-controlled tests are carried out in a wide range of axial and shear strain amplitudes. The

influence of phase angle shift during biaxial axial-torsional tests is also examined. In addition, the dependency of the mechanical behaviour of AM30 extrusion on loading direction (with respect to extrusion direction) is explored and the results are discussed in relation with basal texture induced by extrusion process. Microstructure and fracture surface observations are made in order to understand underlying deformation mechanisms.

1.2.2 Fatigue characterisation and modelling of AM30 extrusion

The low-cycle fatigue response of experimental alloy is investigated by constructing strain-life plots and comparing with other common wrought magnesium alloys. A number of available fatigue damage models are contrasted on the basis of their ability to predict the fatigue crack initiation life of AM30 Mg alloy extrusion under various uniaxial and multiaxial loading conditions.

1.2.3 Constitutive modelling of wrought Mg alloys

The main objective of this study is to develop a cyclic plasticity model capable of describing anisotropy and asymmetry features associated with the cyclic behaviour of wrought magnesium alloys. An important aspect of such a model would be its generality, meaning that it can be exploited to predict the cyclic stress-strain response of any wrought magnesium alloy under general loading condition, given the appropriate parameter calibration.

1.2.4 Numerical implementation and component-level verification of developed constitutive model

Another objective of the current research is to numerically implement the proposed constitutive model in the user material subroutine (UMAT) in order to use it inside commercial finite element software packages such as Abaqus®. This enables analyzing the response of a wrought magnesium alloy component under cyclic loading, for purposes of optimizing its process parameters and estimating the component's fatigue life (when pairing with a fatigue damage model).

In order to attain the ultimate objective of this research, which is the development and verification of an accurate cyclic plasticity model for wrought magnesium alloys, in-depth understanding of their uniaxial and multiaxial cyclic stress-strain responses is crucial. Most of conventional wrought magnesium alloys have exhibited common macroscopic flow features. However, due to more pronounced anisotropic response, compared to rolled Mg alloys, AM30 extrusion is selected here. The study of uniaxial cyclic behaviour along different material orientations sets the stage for incorporating anisotropy in the proposed plasticity formulation. Multiaxial combined loading study provides insight into contributions from direction-dependent properties to overall material response, which can be exploited in the adjustment and verification of the developed plasticity model.

1.3 Thesis overview

In addition to current chapter, there are five more chapters herein, which includes but not limited to three manuscripts either published or submitted for publication in peer-reviewed journals.

Chapter 2 begins with giving brief introductory information on the plastic deformation of wrought magnesium alloys. Available cyclic plastic models developed in the framework of continuum plasticity for wrought Mg alloys (mostly sheets) are categorized and briefly reviewed in the rest of this chapter.

Chapter 3 presents and compares the results of fully reversed strain-controlled cyclic tension-compression experiments on AM30 Mg alloy extrusion along two orthogonal directions, i.e., extrusion and transverse. Microstructure, texture and fracture surfaces of specimens tested at different conditions are analyzed. Axial fatigue properties of AM30 extrusion is compared with other common wrought Mg alloys. At the end of the chapter, two fatigue damage models, one strain-based (Smith-Watson-Topper) and one energy-based (Jahed-Varvani) are evaluated on the basis of life prediction for anisotropic materials. This chapter covers the published manuscript in the journal of Materials Science and Engineering: A [7].

Chapter 4 investigates multiaxial cyclic behaviour of AM30 Mg alloy extrusion by conducting combined biaxial axial-torsional cyclic experiments at different amplitudes and varying phase angle shifts. Pure torsional cyclic behaviour is also characterised in this chapter. The ability of three different fatigue damage models for predicting the crack initiation life of

AM30 extrusion under multiaxial loading conditions is studied. This chapter consists of the published manuscript in the journal of International Journal of Fatigue [8].

Chapter 5 puts forward a new phenomenological cyclic plasticity model and its implementation, calibration and verification. The fundamental ingredients of any continuum plasticity theory, yield function, flow rule, and hardening rule are formulated for proposed cyclic plasticity model. An efficient numerical implementation scheme entailing stress update algorithm and continuum tangent stiffness formulation is developed. Model calibration and verification are performed through cyclic biaxial axial-torsional strain-controlled as well as notched plate loading-unloading tests' results. The contents of this chapter constitute the submitted manuscript for possible publication in International Journal of Plasticity.

Chapter 6, finally, recommends potential subjects for continuing and complementing current research in the future.

Chapter 2

Background and literature review

This chapter first gives a brief introduction to wrought magnesium alloys, including different deformation mechanisms operating in the microstructural level and their representation in macro level. In this sense, unusual characteristics of magnesium flow curves during cyclic plastic loading are also pointed out. Then, a comprehensive review of available cyclic plasticity models for wrought magnesium alloys is presented.

2.1 Background on wrought Mg alloys

Die casting has been the main manufacturing process for magnesium components [9–11]. Compared to cast products, wrought magnesium alloys (manufactured mainly by rolling, forging and extrusion processes [9,12]) possess strong basal texture and have subsequently shown enhanced mechanical properties, such as tensile and fatigue properties [13]. Taking advantage of these characteristics, in addition to their lightweight property, wrought magnesium alloys have potential for automotive applications. There are, however, some complexities associated with wrought magnesium alloys in the process design stage regarding constitutive modelling of their unusual plastic behaviour. These unusual plastic characteristics, which will be mentioned later, are ascribed to the Hexagonal Close-Packed (HCP) crystal structure of magnesium [14]. To better understand the role of HCP cell structure, different deformation mechanisms are briefly discussed in the following.

2.1.1 Deformation mechanisms

In order to accommodate deformation, when atomic movements are restricted, crystal structures undergo slip and twinning. In cubic crystals, slip is the dominant deformation mechanism, whereas this is not the case for HCP metals. In magnesium alloys, there are a few active slip systems at room temperature, which is presumed the main reason for their low formability. Different slip planes in magnesium alloys are illustrated in Figure 2.1. Among these slip systems, only basal slip in $< 11\bar{2}0 >$ direction on the basal plane (0001) is active at the room temperature [15]. Critical Resolved Shear Stress (CRSS) for this basal slip is measured to be 0.5 *MPa* [16]. Although prismatic and pyramidal slip systems are also feasible in magnesium alloys [17,18], they are hard to activate at low temperatures due to their high CRSS values, which are two orders of magnitude higher than that of the basal slip [16]. The CRSS for second-order pyramidal $< c + a >$ type slip (shown with the Burgers vector of $[\bar{1}\bar{1}23]$ in Figure 2.1) is even much higher [19,20], and thereby, their activation is less probable at low temperatures.

Through slip, four independent deformation systems are provided for magnesium alloys at room temperature. However, according to von Mises criterion [21], at least five independent systems are needed in order for the deformation to be homogeneously accommodated within the polycrystalline material. Twinning in magnesium provides an extra independent deformation mechanism to meet the von Mises criterion requirements.

Unlike slip, twinning is a polar mechanism, meaning that it can cause shear to happen only in one direction [13]. Shear direction during $\{10\bar{1}2\}$ twinning in HCP metals is dependent upon the ratio c/a of their cell structure. The value of c/a ratio at which the shear direction

changes is $\sqrt{3}$ [22]. Magnesium crystal structure has $^{c}/_{a}$ ratio of 1.624 which is less than $\sqrt{3}$, hence, $\{10\bar{1}2\}$ twinning in magnesium is of tensile nature [23]. This means that twinning in magnesium cell occurs through extension along its c-axis direction or contraction along the direction normal to the c-axis direction [19,24]. However, it should be noted that twinning can accommodate a finite amount of strain before the microstructure saturates. It is reported that theoretical maximum extension that can be accommodated by $\{10\bar{1}2\} < 10\bar{1}\bar{1} >$ twinning (excluding double twinning) is 6.5% [13]. A $\{10\bar{1}2\}$ twin habit plane inside a HCP unit cell is shown in Figure 2.1.

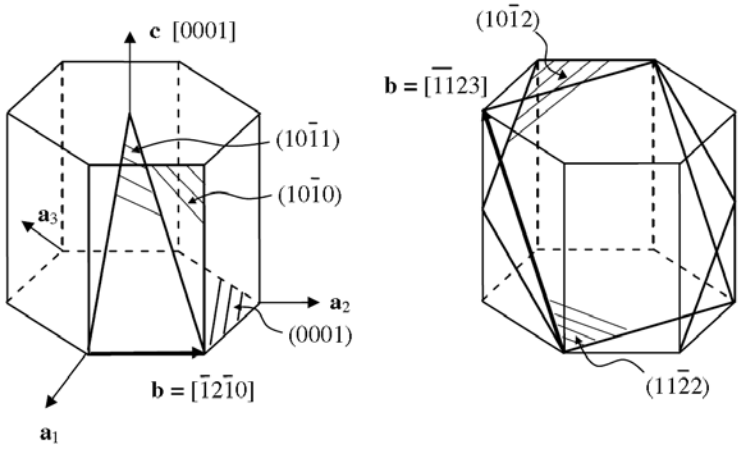

Figure 2.1 Various slip planes and a $\{10\bar{1}2\}$ twin habit plane in a HCP crystal [13]**.**

Another deformation mechanism reported for wrought magnesium alloys is de-twinning [22,24,25]. De-twinning may occur in a twinned portion of the microstructure upon reverse deformation. Twins may disappear or become narrower during de-twinning. Twinning and de-twinning both have similar crystal processes and thus, have the same effect on plastic behaviour of magnesium alloys.

2.1.2 Plastic Behaviour

Owing to the strong propensity of magnesium alloys to mechanical twinning at room temperature, they exhibit exceptional macroscopic characteristics during plastic deformation. In this regard, one unusual behaviour of wrought magnesium alloys is yield asymmetry; that is, the initial yield stress in tension is much higher than the initial yield stress in compression ($\sigma_T > \sigma_C$ in Figure 2.2). For instance, the 0.2% offset yield strength for extruded AZ31B Mg alloy in extrusion direction was reported to be 213 *MPa* in tension, while 108 *MPa* in compression [26]. This difference in the yield strength is attributed to the occurrence of twinning when compressing along extrusion direction.

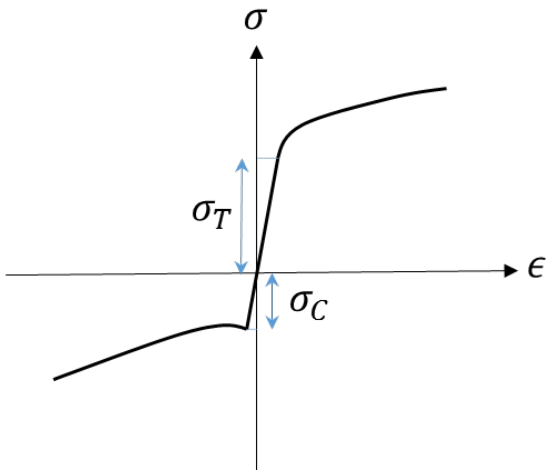

Figure 2.2 Schematic illustration of typical tension/compression stress-strain curves of wrought magnesium alloys.

Plastic flow asymmetry during cyclic axial deformation is another unique feature of wrought magnesium alloys. During uniaxial tension, as is shown in Figure 2.2 , the flow curve is normal concave shape. Similar to cubic metals, this is due to the dominance of slip mechanism

(basal slip in magnesium). On the contrary, during in-plane compression or tension after compression (Figure 2.3), one can observe the unusual sigmoidal shape of stress-strain curve. The upward concavity of the curve is characteristic of twinning/de-twinning. The inflection (increase in the strain hardening rate) seen in Figure 2.3 is the result of a change in dominant deformation mechanism from de-twinning to slip, upon exhaustion of de-twinning [27]. The same transition can happen during in-plane compression, when twinning is the dominant mechanism. Continuation of compressive deformation results in the exhaustion of twinning, i.e. no further un-rotated crystals left, after which, slip starts to dominantly operate again.

In addition to yield asymmetry and plastic flow asymmetry, wrought magnesium alloys exhibit different behaviour along different directions. The so-called directional anisotropy in extruded AZ31B Mg alloy can be seen from Figure 2.4. Under both compressive and tensile loading, hardening behaviour differs from one orientation to another. This is especially noticeable for compression along extrusion direction (ED) and tension along 45° with concave-up shape of the flow curve, which is characteristic of deformation twinning. Another significant difference in behaviour along different directions is observed for yield strength under tensile loading. The yield strength difference along ED and TD orientations was reported to be 74% [28,29].

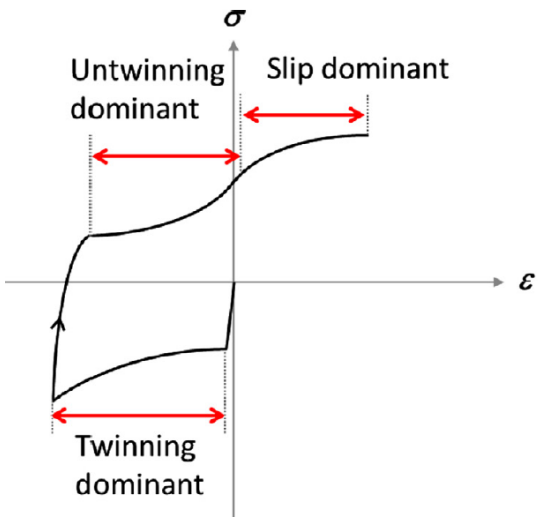

Figure 2.3 Schematic representation of typical flow curve of wrought magnesium alloy under compression followed by tension showing regions associated with different dominant deformation mechanisms [27]**.**

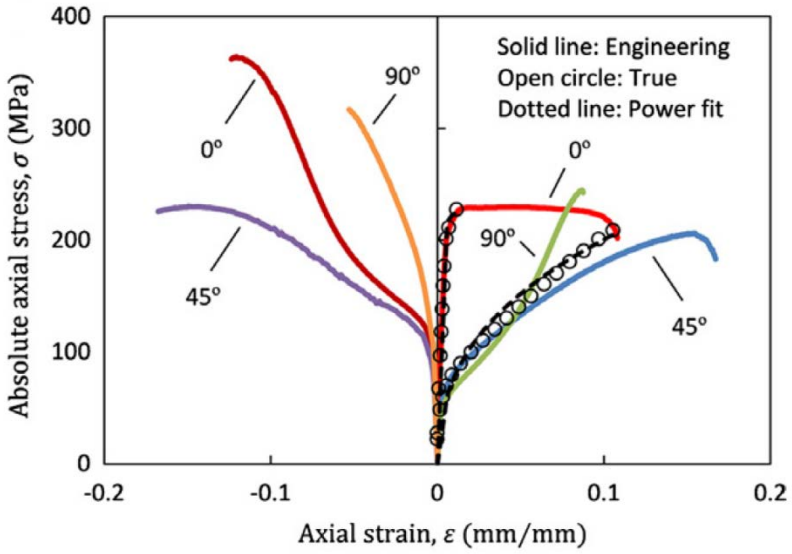

Figure 2.4 Monotonic compressive and tensile flow curves of AZ31B Mg alloy extrusion along different directions [26]**.**

In contrast to the unusual asymmetric axial hysteresis, wrought magnesium alloys exhibit normal symmetric shear cyclic curves. This is illustrated in Figure 2.5, where shear and axial cyclic hysteresis results are plotted for extruded AZ31B Mg alloys over a range of strain amplitude. Although the Masing behaviour is not perfectly followed for cyclic shear loading, especially at low shear strain amplitudes [26], it is reasonable to assume Masing behaviour for the sake of simplicity and thereby, employ hysteresis doubling principle to model the shear hysteresis loops for magnesium alloys.

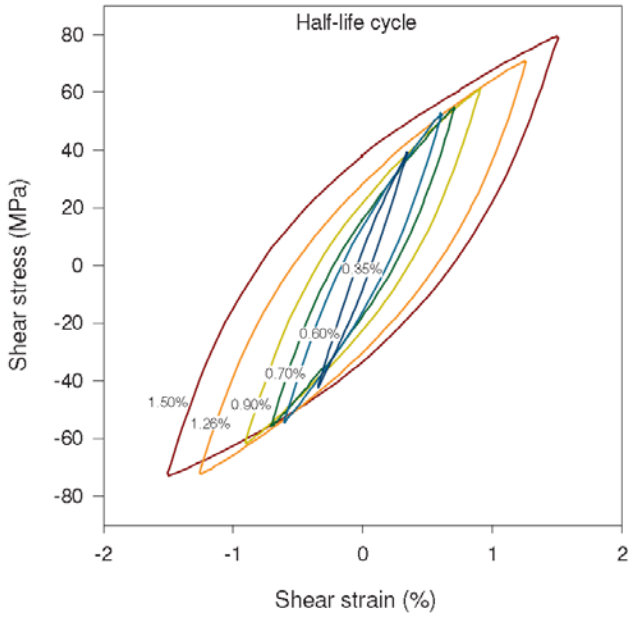

Figure 2.5 Shear cyclic hysteresis curves of AZ31B Mg alloy extrusion [28]

2.2 Review of continuum cyclic plastic models for wrought Mg alloys

In the context of cyclic plasticity modelling of magnesium alloys, there are two major approaches employed by different researchers, namely crystal plasticity approach and continuum phenomenological plasticity approach.

Crystal plasticity is a very useful method to study the effects of underlying microstructure-related features on the macroscopic behaviour of materials [30–33]. This theory is based on the fact that the plastic deformation of the bulk material as an aggregate of crystals is the resultant of plastic deformations of each individual crystal. The main constituents of this approach are local deformation systems and interaction between them, the activation of different deformation mechanisms under various conditions as well as distribution of crystallographic orientations interpreted as preferred texture in the microstructure [32].

Continuum plasticity is based upon two principal concepts: defining a yield surface, which determines the onset of plastic deformation; and adopting a hardening rule, which mathematically describes the change in yield stress with further plastic deformation and, in other words, governs the movement of the yield surface in stress space. Flow rule (normality hypothesis to designate the direction of plastic strain increment) may be regarded as another major constituent of continuum plasticity [34]. The ability of this approach to model the cyclic behaviour of initially isotropic metals under various loading conditions is verified. On the other hand, there have been a number of recent endeavors to extend the application of continuum plasticity approach for modelling the unusual behaviour of anisotropic and asymmetric metals

such as magnesium alloys. One group of researchers contributed to this extension by making use of an anisotropic yield function that can account for yield asymmetry and direction-dependent behaviour. The alternative approach was to introduce anisotropic hardening rules capable of describing different hardening behaviour during tensile and compressive reversals.

In the current chapter, available continuum-based constitutive models capable of describing the unusual plastic behaviour of wrought magnesium alloys are comprehensively reviewed, in chronological order. It should be emphasized here that these models are generally aimed for sheet metal forming applications (the assumption of plane stress condition is inferred), in which material behaviour during loading from unstressed state, unloading and loading in reversed direction is considered.

2.2.1 Anisotropic yield criteria

The most common isotropic yield functions for metals were proposed by von Mises and Tresca [35]. These yield functions may be represented in the general form of Hershey's criterion [36], in terms of the principal values of stress tensor ($\boldsymbol{\sigma}$) or its deviator ($\boldsymbol{S}$):

$$\begin{aligned} \emptyset &= |\sigma_1 - \sigma_2|^a + |\sigma_2 - \sigma_3|^a + |\sigma_1 - \sigma_3|^a - 2\mathrm{Y}^a \\ &= |S_1 - S_2|^a + |S_2 - S_3|^a + |S_1 - S_3|^a - 2\mathrm{Y}^a = 0 \end{aligned} \quad \textbf{(2.1)}$$

where Y is the uniaxial yield stress. Equation (2.1) results in von Mises yield condition for $a = 2$ or $a = 4$, and reduces to Tresca criterion for $a = 1$ or $a = \infty$. Drucker [37] also proposed another isotropic yield criterion by making use of the invariants of stress deviator:

$$\emptyset = {J_2}^3 - c{J_3}^2 - {\tau_Y}^6 \quad \textbf{(2.2)}$$

where $J_2 = \frac{1}{2} trace(\boldsymbol{S}^2)$ and $J_3 = \frac{1}{3} trace(\boldsymbol{S}^3)$ are, respectively, the second and third invariants of the stress deviator $\boldsymbol{S}$ and τ_Y is the yield stress under pure shear loading.

The von Mises, Tresca and Drucker yield criteria are independent of choice of reference frame. For anisotropic materials, on the contrary, due to their direction-dependent behaviour, the yield criterion should be dependent upon the reference frame. The simplest form of anisotropy in materials is called orthotropic symmetry which is exhibited by rolled sheets. The axes of reference frame for such materials are aligned with three axes of symmetry, namely, rolling, normal and transverse directions. In 1948, Hill [38] proposed a quadratic version of von Mises isotropic yield function for orthotropic materials:

$$\emptyset = F\left(\sigma_{yy} - \sigma_{zz}\right)^2 + G(\sigma_{zz} - \sigma_{xx})^2 + H\left(\sigma_{xx} - \sigma_{yy}\right)^2 + 2L\sigma_{yz}^2 + 2M\sigma_{zx}^2 + 2N\sigma_{xy}^2 - \mathrm{Y}^a = 0 \quad \textbf{(2.3)}$$

where F, G, H, L, M and N are material parameters, which are calculated from Lankford's coefficients (r_0, r_{45}, and r_{90}). This yield function was showed to properly describe the behaviour of steels [39]. In 1979, Hill [40] proposed another yield function in a non-quadratic form which was capable of describing the behaviour of materials other than steels. One description of this yield criterion which accounts for planar isotropy under plane stress condition is:

$$\emptyset = |\sigma_1 + \sigma_2|^a + (1 + 2\bar{r})|\sigma_1 - \sigma_2|^a - 2(1 + \bar{r})\mathrm{Y}^a = 0 \quad \textbf{(2.4)}$$

where $\bar{r}$ is average Lankford's coefficient. Hosford [41] proposed a generalization of Hershey's yield criterion, Equation (2.1), to apply to the materials with orthotropic symmetry:

$$\emptyset = F\left|\sigma_{\mathrm{yy}} - \sigma_{\mathrm{zz}}\right|^{a} + G\left|\sigma_{\mathrm{zz}} - \sigma_{\mathrm{xx}}\right|^{a} + H\left|\sigma_{\mathrm{xx}} - \sigma_{\mathrm{yy}}\right|^{a} - \mathrm{Y}^{a} = 0 \quad \textbf{(2.5)}$$

where F, G and H are material constants. Before this generalized yield function, Hosford [42] presented another criterion through modification of Hill's 1948 criterion, Equation (2.3), to account specifically for the strength differential effect (difference in yield stress in tension and compression) and anisotropy exhibited by HCP metals:

$$\emptyset = A\sigma_{xx} + B\sigma_{yy} - (A+B)\sigma_{zz} + F\left(\sigma_{yy} - \sigma_{zz}\right)^{2} + G(\sigma_{xx} - \sigma_{zz})^{2} + H\left(\sigma_{xx} - \sigma_{yy}\right)^{2} = 1 \quad \textbf{(2.6)}$$

where A, B, F, G and H are material constants.

Hill's 1979 and Hosford's criteria, Equations (2.4) and (2.6), have shared the same deficiency: ignoring shear stress components. A yield function which does not consider shear stress components, is limited to the cases of planar isotropy or cases where anisotropy axes coincide with the principal axes of stress. Accordingly, Liu et al. [43] attempted to address this deficiency by modifying Hill's 1948 criterion into a form that considers strength differential effects (yield asymmetry) as well as anisotropy and includes shear stress components. As discussed by Banabic et al. [35], strength differential effects in Liu's and Hosford's formulations are as a result of hydrostatic pressure (first invariant of stress), while, in fact, for pressure-insensitive HCP metals it is due to twinning-induced shear mechanisms. The description of tension-compression yield asymmetry related to twinning is stated to be the main difficulty in developing proper yield functions for HCP metals [35].

More recently, there have been efforts to develop a macroscopic yield criterion capable of describing yield asymmetry due to twinning in pressure-insensitive HCP metals. In this context, the first attempt made by Cazacu and Barlat in 2004 [44] who proposed an isotropic yield function as a generalization of von Mises criterion:

$$\emptyset = (J_2)^{3/2} - cJ_3 - {\tau_Y}^3 \qquad \textbf{(2.7)}$$

where c is a material constant depending on the yield stresses in tension (Y_T) and compression (Y_C):

$$c = \frac{3\sqrt{3}\left({Y_T}^3 - {Y_C}^3\right)}{2\left({Y_T}^3 + {Y_C}^3\right)} \qquad \textbf{(2.8)}$$

When the yield in tension and compression are the same (i.e., $c = 0$), Equation (2.7) reduces to von Mises yield criterion. Yield surface predictions from this isotropic criterion were reported [45] to be in accordance with the polycrystalline calculations of Hosford and Allen [46].

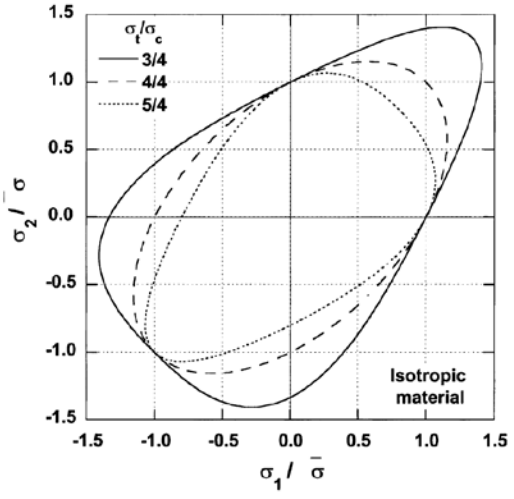

Figure 2.6 Yield surfaces predicted by Cazacu-Barlat's 2004 criterion under plane stress conditions [44]**.**

In order to extend their isotropic yield criterion to be used for anisotropic materials, Cazacu and Barlat employed the method proposed in 2001 [47]. According to this method, the generalizations of J_2 and J_3, which are applicable to anisotropic conditions, are presented using theory of representation of tensorial functions. For instance, generalized version of J_2 to take into account orthotropy would be:

$$J_2^0 = \frac{a_1}{6}\left(\sigma_{xx} - \sigma_{yy}\right)^2 + \frac{a_2}{6}\left(\sigma_{xx} - \sigma_{yy}\right)^2 + \frac{a_3}{6}\left(\sigma_{xx} - \sigma_{yy}\right)^2 + a_4{\sigma_{xy}}^2 + a_5{\sigma_{xz}}^2 + a_6{\sigma_{yz}}^2 \quad \textbf{(2.9)}$$

where the coefficients a_k reduce to unity in isotropic conditions. Cazacu and Barlat used the experiments of Kelly and Hosford [48] to verify their proposed anisotropic and asymmetric yield function. As is shown in Figure 2.7, the predictions were in agreement with the experimental results.

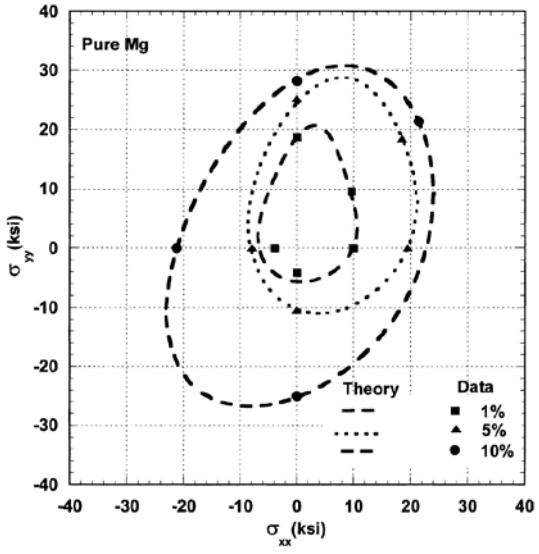

Figure 2.7 Comparison between yield loci predictions of Cazacu-Barlat's 2004 criterion and experimental data for pure magnesium sheet [44]**.**

In 2006, Cazacu and Barlat [49] introduced another isotropic yield function (CPB06) capable of describing yield asymmetry. It was formulated in terms of principal deviatoric stresses:

$$\emptyset = (|S_1| - kS_1)^a + (|S_2| - kS_2)^a + (|S_3| - kS_3)^a - Y = 0 \quad \textbf{(2.10)}$$

where Y is the size of the yield surface and k is a material parameter expressible as a function of ratio of tensile to compressive uniaxial yield stresses (Y_T/Y_C):

$$k = \frac{1 - h(\frac{Y_T}{Y_C})}{1 + h\left(\frac{Y_T}{Y_C}\right)} \quad \textbf{(2.11)}$$

$$h\left(\frac{Y_T}{Y_C}\right) = \left(\frac{2^a - 2\left(\frac{Y_T}{Y_C}\right)^a}{\left(2\frac{Y_T}{Y_C}\right)^a - 2}\right)^{\frac{1}{a}} \quad \textbf{(2.12)}$$

In contrast to their 2004 criterion (which was a homogeneous function of degree three), Equation (2.7), Cazacu-Barlat's 2006 criterion is a homogeneous function of degree a in stress. This made the yield criterion more suitable to describe HCP metals for which the yield surface is better represented by a quadratic function, e.g., Titanium alloys [50]. One other difference between these two yield criteria is in the way they are extended to include anisotropy. In the case of 2006 criterion, Cazacu and Barlat used linear transformation approach by applying a fourth-order linear transformation operator on the stress deviator and they substituted principal stress deviators (S_i) with principal values of the transformed tensor (Σ_i):

$$\boldsymbol{\Sigma} = [\boldsymbol{B}]\boldsymbol{S} \tag{2.13}$$

where $\boldsymbol{B}$ is a fourth order constant tensor. With this approach, the convexity of the anisotropic yield function is automatically ensured, after the original convex isotropic function. With the previous approach, however, as mentioned by Cazacu and Barlat [49], the convexity of the anisotropic yield function is imposed only numerically.

Plunkett et al. [50] argued that nine anisotropy coefficients in CPB06 criterion, Equation (2.10), may not be enough to accurately describe metals with pronounced in-plane anisotropy. Hence, they suggested to consider n linear transformations ($n \geq 2$) of stress deviator instead of only one, in order to increase the number of coefficients. The comparison of predicted yield loci by CPB06ex2 and experimental results for AZ31B sheet is depicted in Figure 2.8. It was concluded that an increase in the number of anisotropy coefficients enhances the description of yield asymmetry as well as anisotropic behaviour displayed by HCP metals.

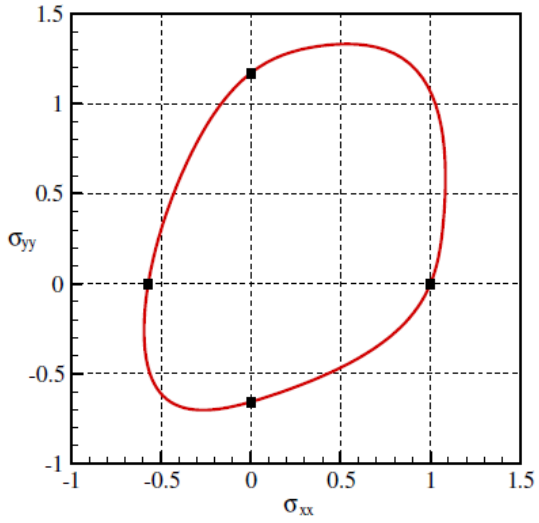

Figure 2.8 Plane stress yield surface for AZ31B sheet constructed by CPB06ex2 [50]**.**

Introducing pressure dependency to the isotropic form of Cazacu-Barlat's 2004 criterion through first invariant of stress tensor I_1, Yoon et al. [51] proposed a general asymmetric yield function, which was further extended to include orthotropic behaviour.

$$f(\sigma_{ij}) = \tilde{I}_1 + \left(J_2'^{3/2} - J_3''\right)^{1/3} \tag{2.14}$$

where $\tilde{I}_1$ represents the anisotropic-weighted first stress invariant, J_2' is the second stress invariant of a transformed stress tensor $\boldsymbol{s}'$, and J_3'' is the third stress invariant of another transformed stress tensor $\boldsymbol{s}''$. Yield surface predicted by Equation (2.14) was compared with experimental results for AZ31 Mg alloy and is shown here in Figure 2.9.

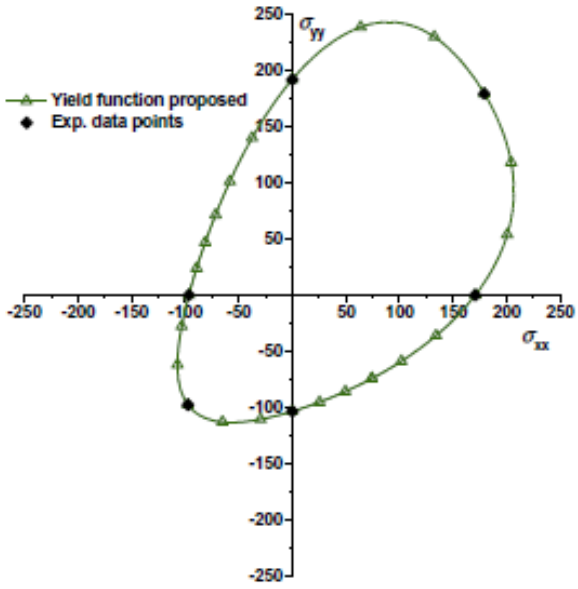

Figure 2.9 Yield surface prediction for AZ31 by Yoon et al. yield function [51]**.**

2.2.2 Anisotropic hardening rule

Complemented with a varying uniaxial yield stress as a function of equivalent plastic strain, the so-called isotropic hardening, all the reviewed yield functions can give an accurate description of plastic behaviour of HCP metals (magnesium alloys, in particular) solely under proportional loading conditions, i.e., when the stress tensor is obtainable by multiplying a scalar by a constant tensor [52,53]. However, for non-proportional loading it is reported that predictions deviate from experimental observations and thus, isotropic hardening is not enough to capture plastic behaviour. Especially for reverse loading condition, when metals usually display the Bauschinger effect (yielding at a lower absolute stress compared to the flow stress just prior to the reversal, as is shown in Figure 2.10) upon load reversal, an anisotropic hardening rule needs to be coupled with any definition of the yield surface.

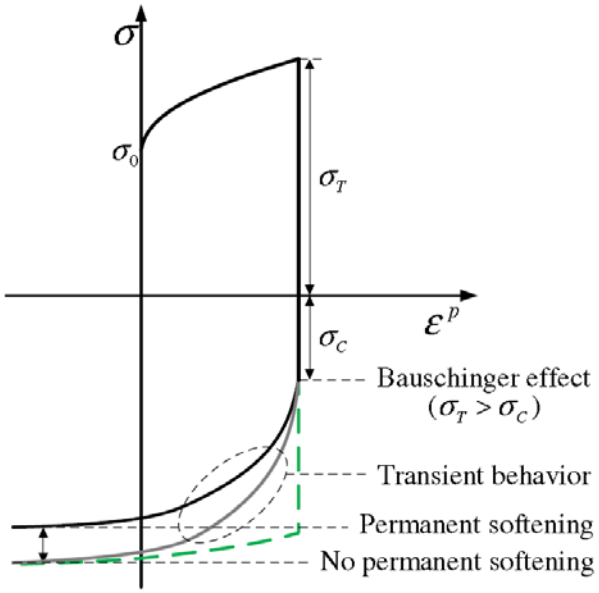

Figure 2.10 Schematic illustration of flow characteristics observed during reversed loading [34]**.**

Kim et al. [27] proposed a temperature-dependent elastic-plastic constitutive model for describing the cyclic behaviour of AZ31B Mg alloy sheets. They decomposed the yield locus in stress space into two separate regions, i.e., twinning/de-twinning dominant region and slip dominant region, each being defined by a separate yield function. Cazacu-Barlat's 2006 criterion, Equation (2.10), was chosen for the former region and Hill's 1948 criterion, Equation (2.3), was selected for the latter region (Figure 2.11).

Moreover, to describe the uniaxial behaviour of AZ31B Mg alloy sheet, empirical reference flow stress equations were suggested based on the experimental uniaxial curves under tension, compression and tension following compression corresponding to slip, twinning and de-twinning-dominated flow regions, respectively. Under compressive deformation, they suggested Equation (2.15) for the reference flow stress in the twinning-dominated region:

$$\hat{\sigma}_t = a_t + b_t \exp\left(c_t(\bar{\varepsilon}_t - d_t\bar{\varepsilon}_s)\right) - e_t\bar{\varepsilon}_s \qquad \textbf{(2.15)}$$

where a_t, b_t, c_t, d_t and e_t are material parameters and $\bar{\varepsilon}_t$ and $\bar{\varepsilon}_s$ are equivalent plastic strains for twinning and slip-dominated (tensile pre-straining) regions, respectively. Then, the yield criterion can be expressed by:

$$\phi_t = \bar{\sigma}_t - \hat{\sigma}_t = 0 \qquad \textbf{(2.16)}$$

where $\bar{\sigma}_t$ is the effective stress in compression derived from CPB06 yield criterion.

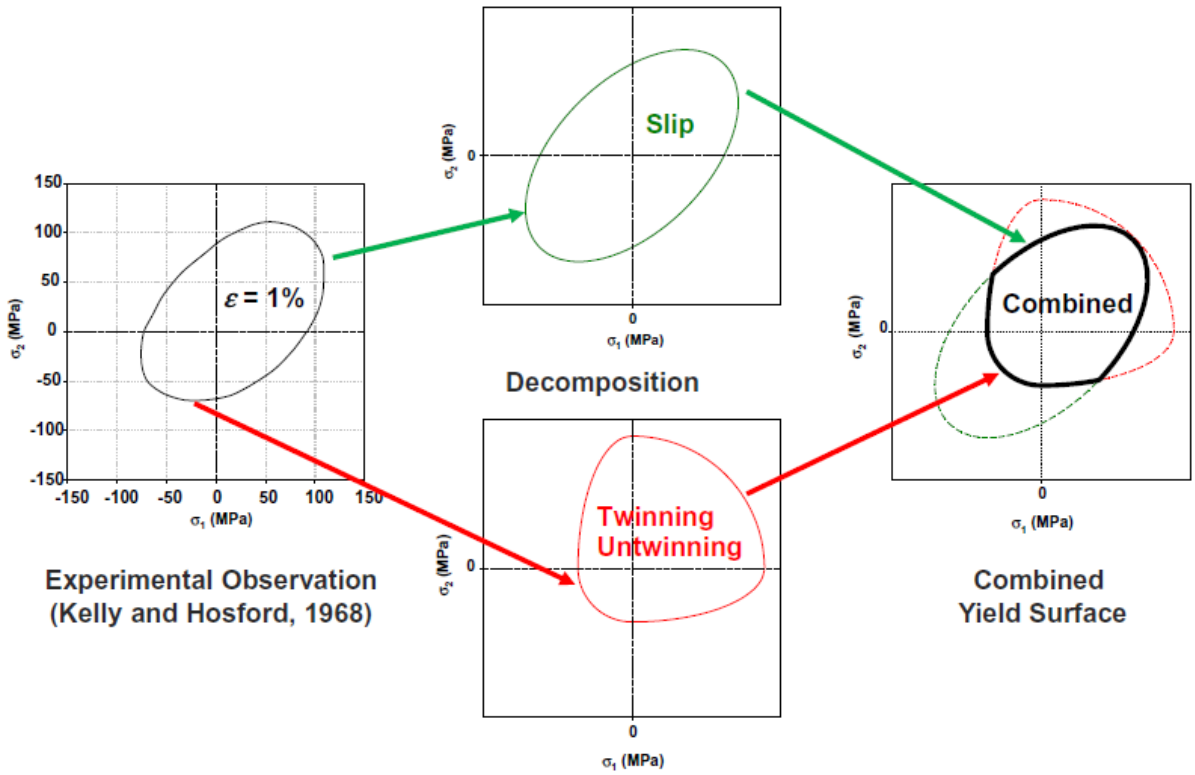

Figure 2.11 Yield surface decomposition suggested by Kim et al. [27].

They also suggested two other empirical equations for reference flow stresses under tension (slip) and tension following compression (de-twinning), with the yield criteria similar to Equation (2.16). A temperature-dependent term was added only to the reference flow stress equation of the slip-dominated region, assuming temperature insensitivity of twinning and de-twinning mechanisms. To decide on the dominant deformation mode the following criterion was employed:

$$\text{Twinning: } \Delta\varepsilon_t^{11} + \Delta\varepsilon_t^{22} \leq 0 \qquad \textbf{(2.17)}$$

$$\text{De-twinning: } \Delta\varepsilon_t^{11} + \Delta\varepsilon_t^{22} > 0,\ \bar{\varepsilon}_t > 0$$

The slip dominates when none of the twinning/de-twinning criteria are met.

After numerical implementation of their proposed model into ABAQUS/Explicit via user material subroutine VUMAT, Kim et al. validated its prediction capability by conducting simple shear and cyclic tension-compression-tension and compression-tension-compression tests on a single-element model at various temperatures and comparing with experiments on AZ31B sheets. Although the correlation between predictions and experimental results was fairly good, the elastic-plastic transient behaviour as well as smooth transition between dominant deformation mechanisms were not correctly captured by the model (See Figure 2.13).

Khayamian et al. [54] developed a simple axisymmetric plasticity model, based on total deformation plasticity approach, capable of considering the asymmetric feature of wrought magnesium alloys during cyclic loading. This model was an extension of 'Variable Material Property' (VMP) method proposed by Jahed and Dubey [55,56]. In the VMP method, plasticity is modelled through degrading material elastic properties at plastic material points. The model by Khayamian et al. consists of asymmetric Cazacu and Barlat's 2004 yield criterion and two different hardening curves corresponding to uniaxial tension and compression. In a proportional biaxial loading condition, an interpolated curve is assumed to represent the material response. Employing experimental data on cylindrical samples of cast AZ80 under internal pressure and axial tension/compression [57], the model predictions were validated, as shown in Figure 2.12. The same extension logic was used by Kalatehmollaei et al. [58] and Marzbanrad et al. [59] to predict the stress-strain curves of wrought magnesium alloys during load-controlled rotating-bending tests.

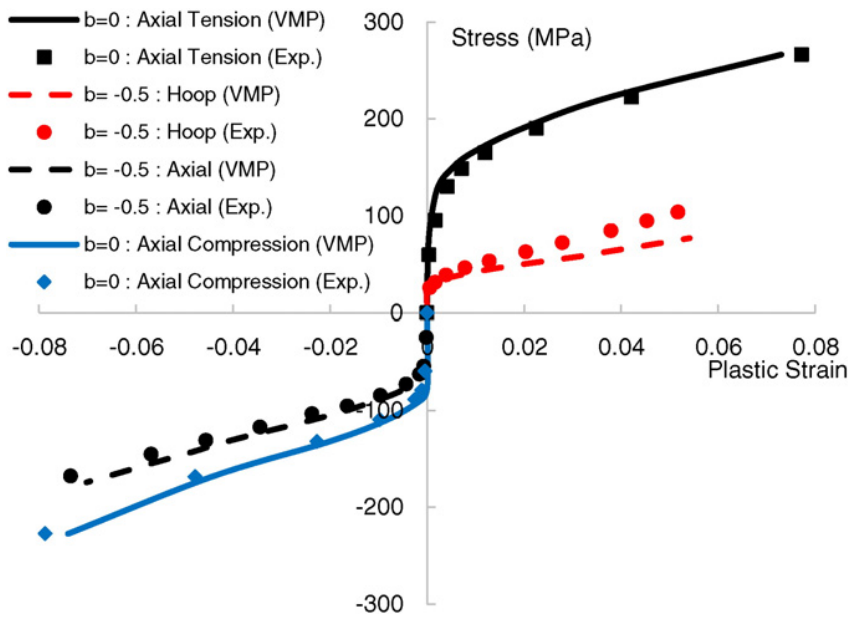

Figure 2.12 Comparisons between predictions by Khayamian et al. [54] **model with experimental results from** [57]**.**

Other developed cyclic plasticity models for wrought magnesium alloys in the literature can be categorized into three groups based on different ways of describing the anisotropic hardening behaviour. These models are reviewed in the following sections.

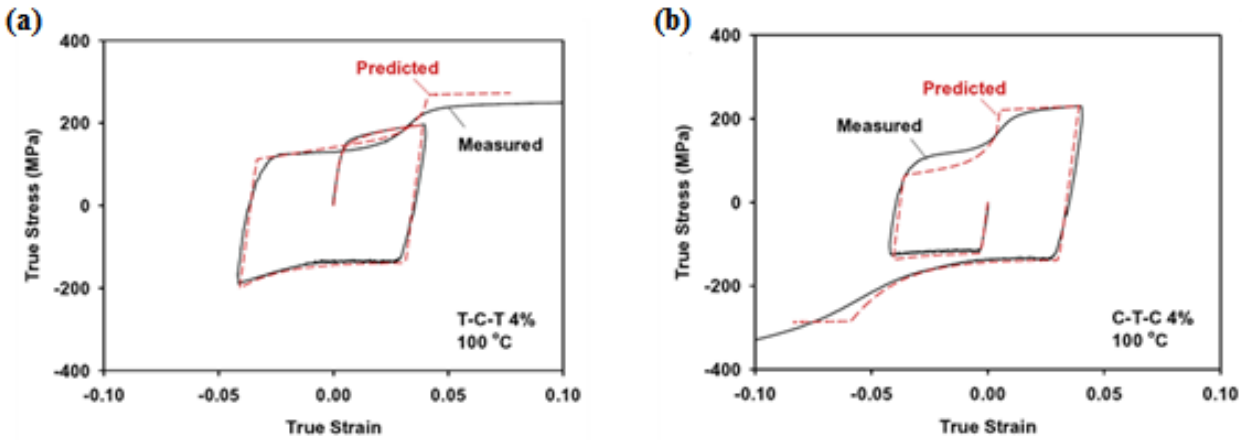

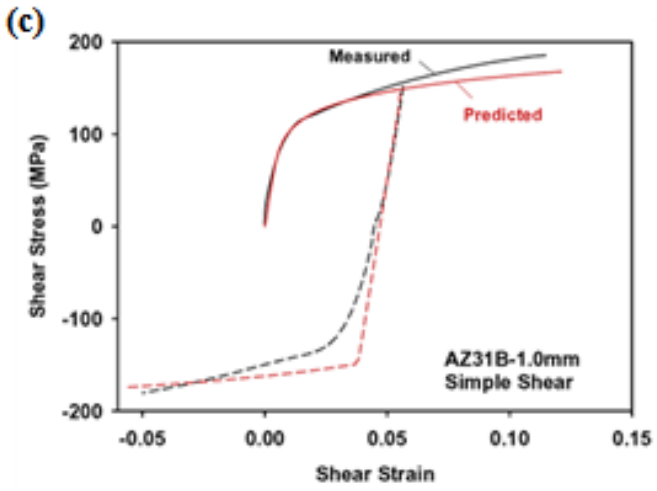

Figure 2.13 Experimental vs. predictions from model proposed by Kim et al. for AZ31B Mg alloy under (a) tension-compression-tension, (b) compression-tension-compression and (c) shear cyclic loading [27].

2.2.2.1 Nonlinear kinematic hardening

To account for the Bauschinger effect, kinematic hardening was proposed. According to the simplest form of kinematic hardening, plastic deformation is controlled by the back stress tensor ($\boldsymbol{\alpha}$) representing the center of the yield surface, the evolution of which translates the yield surface in stress space:

$$\emptyset(\boldsymbol{\sigma} - \boldsymbol{\alpha}) - Y = 0 \qquad \textbf{(2.18)}$$

Prager [60] proposed that the back stress evolves in the direction of the plastic strain increment tensor ($d\boldsymbol{\varepsilon}^{\boldsymbol{p}}$), which is the direction of normal to the yield surface assuming associated flow rule (will be explained later). Prager's rule was modified later by Ziegler [61], who proposed that the evolution of back stress happens in the radial direction:

$$d\boldsymbol{\alpha} = d\mu(\boldsymbol{\sigma} - \boldsymbol{\alpha}) \tag{2.19}$$

The evolution of the von Mises yield surface according to the Prager's and Ziegler's rules are illustrated in Figure 2.14. As is depicted in Figure 2.14(a), during uniaxial loading Prager's hardening rule creates hardening or softening in the lateral directions, which has no experimental evidence [62]. It is worth mentioning that Prager and Ziegler's rules give the same back stress evolution equation when the von Mises yield function is coupled with the hardening rule and the formulation is done in 3D stress space [62].

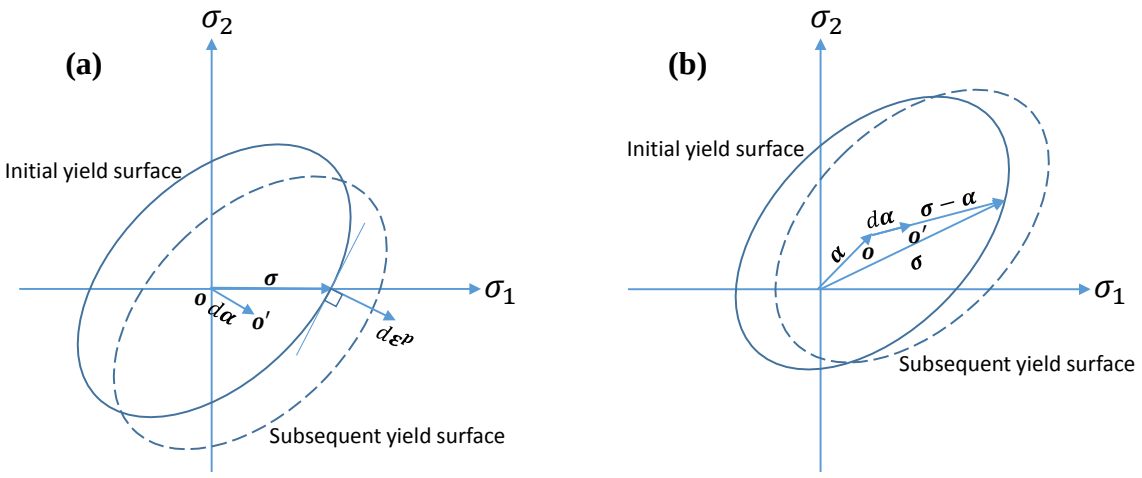

Figure 2.14 (a) Prager's and (b) Ziegler's hardening rules under plastic straining.

Bauschinger effect can be sufficiently modeled by linear kinematic hardening, however, to account for transient behaviour, i.e., smooth transition from elastic to plastic region (Figure 2.10), a nonlinear evolution of the back stress tensor has been proposed originally by Armstrong and Frederick [63] and modified later by Chaboche et al. [64] through superposing multiple hardening rules of the same type as the original Armstrong-Frederick's:

$$d\boldsymbol{\alpha}_i = \sum_{i=1}^{M} \frac{2}{3} C_i d\boldsymbol{\varepsilon^p} - \gamma_i \boldsymbol{\alpha}_i dp \qquad d\boldsymbol{\alpha} = \sum_{i=1}^{M} d\boldsymbol{\alpha}_i \tag{2.20}$$

where C_i and γ_i are material constants, M is the number of back stress terms and dp is accumulated plastic strain increment.

There are a number of investigations attempted to include permanent softening, i.e., when reversed flow stress does not reach to the level of monotonic curve just before reversal, (shown in Figure 2.10) as an anisotropic feature into the nonlinear kinematic hardening rule, among which are studies by Geng and Wagoner [65], Chun et al. [66,67] and Moosbrugger [68]. Since these generalizations are performed with the purpose of describing cyclic curves of cubic metals, they are not herein reviewed in detail.

Noban and Jahed [69] proposed an anisotropic form of Equation (2.20) to account for the strong anisotropy of AZ31B extrusion during cyclic axial and torsional experiments. They made use of a von Mises yield surface evolving in stress space through kinematic hardening rule of the following:

$$d\tilde{\alpha}_i = \sum_{i=1}^{M} \sqrt{\frac{2}{3}} [C_i] \tilde{n} dp - [\gamma_i] \tilde{\alpha}_i dp \qquad d\tilde{\alpha} = \sum_{i=1}^{M} d\tilde{\alpha}_i \tag{2.21}$$

where $\tilde{n}$ is the normal to the yield surface vector, $[C_i]$ and $[\gamma_i]$ are diagonal matrices of material constants representing behaviour in different directions. In order to model asymmetric yield in tension and compression, they assumed dependency of material constants to the sign of axial back stress. They also demonstrated that by adjusting the hardening rule in Equation (2.21),

various shapes for the bounding surface of back stress can be modelled, as is shown in Figure 2.14, for three cases of isotropic, symmetric anisotropic, and asymmetric anisotropic materials. The model predictions under proportional axial-torsional cyclic tests were shown to be in good agreement with experimental results. However, it was stated that the model is not able to give the sigmoidal shape of axial hysteresis loops at high strain amplitudes, and further work is needed for simulating response under non-proportional cyclic axial-torsional conditions.

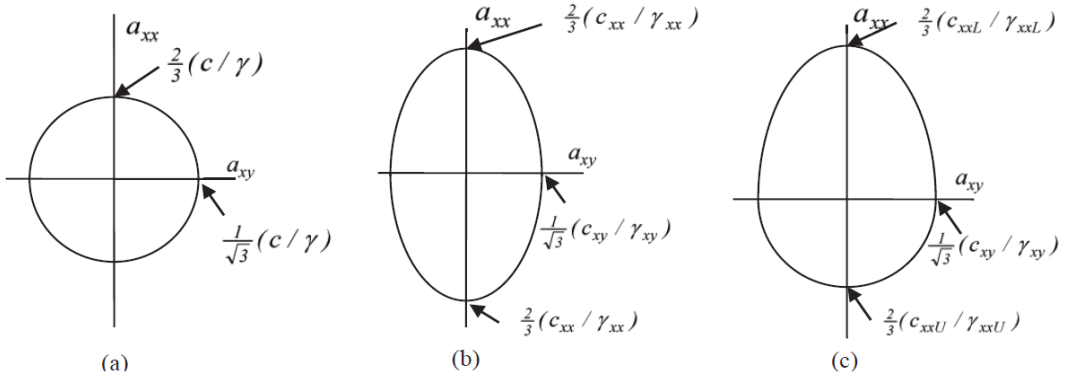

Figure 2.15 Various simulated shapes of back stress bounding surfaces by Noban and Jahed [69] **cyclic plasticity model: (a) isotropic, (b) symmetric anisotropic, (c) asymmetric anisotropic cases.**

Li et al. [70] developed a model, called "TWINLAW" for HCP metal sheets, AZ31B Mg alloy in particular, capable of modelling their unusual plastic deformation characteristics. The yield asymmetry was incorporated into their model using a von Mises yield surface with off-origin center (initial non-zero back stress), as illustrated in Figure 2.16:

$$\boldsymbol{\alpha}_{initial} = \left(\sqrt{2}(Y_T - |Y_C|)\right)\boldsymbol{\Lambda} \qquad \textbf{(2.22)}$$

where:

$$\mathbf{\Lambda} = \frac{1}{\sqrt{2}}\begin{bmatrix} 1 & 0 & 0 \\ 0 & 1 & 0 \\ 0 & 0 & 0 \end{bmatrix} \tag{2.23}$$

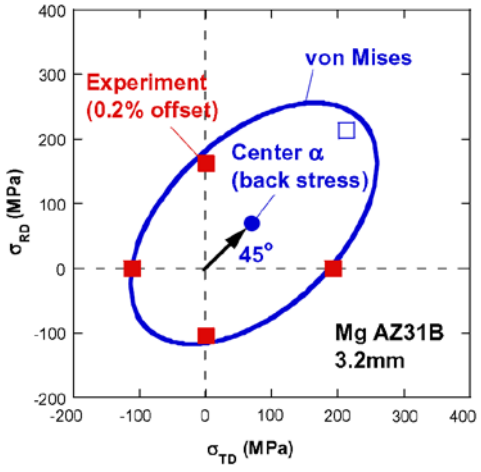

Figure 2.16 Correlation of off-centered von Mises yield surface and experimental initial yielding points for AZ31B Mg alloy [70]**.**

Furthermore, to allow for unusual hardening behaviour of magnesium alloys, Li et al. made use of modified Armstrong-Frederick nonlinear kinematic hardening rules combined with isotropic hardening rule. Their plane stress phenomenological model treated the evolution of the yield surface size and position differently for different loading conditions, including in-plane tension, in-plane compression, and tension following compression corresponding to slip, twinning and de-twinning deformation modes, respectively. During in-plane tension with slip-dominated flow, a rule for the evolution of the back stress was proposed as a modified Armstrong-Frederick's rule:

$$d\boldsymbol{A} = dp\left(\boldsymbol{B}_{\boldsymbol{S}}' - \frac{\boldsymbol{A} - \boldsymbol{A}_{\boldsymbol{c}}}{0.1}\right) \tag{2.24}$$

where $\boldsymbol{A}_{\boldsymbol{c}}$ is the deviatoric back stress corresponding to the current texture, the introduction of which was to maintain the differential yield strength in tension and compression and $\boldsymbol{B}_{\boldsymbol{S}}'$ is a tensor depending on the current plastic strain rate and texture. For twinning-dominated flow, the back stress evolution rule was proposed:

$$d\boldsymbol{A} = dp\left(\boldsymbol{B}_{\boldsymbol{T}}' - \frac{d\varepsilon_3}{\varepsilon_{twin}dp}\boldsymbol{A}\right) \tag{2.25}$$

where $d\varepsilon_3$ is the principal strain increment in the sheet normal direction. Finally, for de-twinning-dominated deformation mode the back stress evolution was assumed:

$$d\boldsymbol{A} = dp\left(\boldsymbol{B}_{\boldsymbol{U}}' - \frac{|d\varepsilon_3|}{\varepsilon_{untwin}dp}\boldsymbol{A}_{\boldsymbol{d}}\right) \tag{2.26}$$

where:

$$\boldsymbol{A}_{\boldsymbol{d}} = \begin{bmatrix} A_{11} - A_{22} & A_{12} & 0 \\ A_{12} & -A_{11} + A_{22} & 0 \\ 0 & 0 & 0 \end{bmatrix} \tag{2.27}$$

Equation (2.27) was defined with the purpose of recovering the isotropy upon de-twinning. Different evolution equations related to each deformation mode were being employed according to a set of criteria. For instance, the criterion for the use of Equation (2.25) was designated as follows:

$$\Delta\varepsilon_1 + \Delta\varepsilon_2 < 0, \qquad W(\hat{x}_3) > 0 \tag{2.28}$$

where $\Delta\varepsilon_1$ and $\Delta\varepsilon_2$ are the major and minor principal in-plane strain increments and $W(\hat{x}_3)$ is the cumulative distribution of *c*-axes parallel to the sheet normal direction ($\hat{x}_3$). Second inequality in Equation (2.28) determines if there are still regions available for further twinning.

Texture evolution and reorientation of *c*-axes during twinning and de-twinning (no texture evolution was considered by Li et al. during slip-dominated flow), was represented through rules explicitly introduced into the proposed model. These explicit rules were also utilized in determining the exhaustion of twinning/de-twinning, after which the abrupt transition (contrary to the gradual transition observed in experiments) of dominant deformation mode from twinning/de-twinning to slip was assumed to occur.

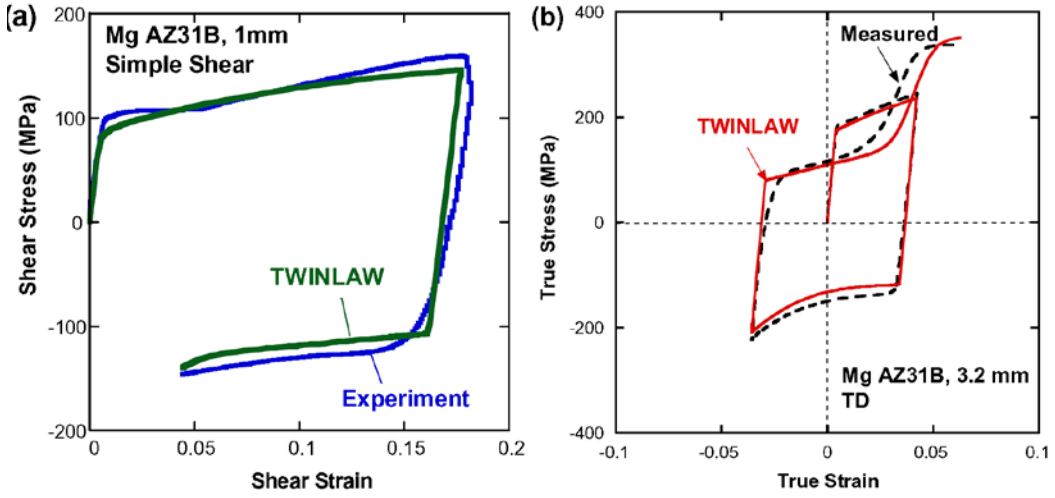

Figure 2.17 Comparison between experimental and predicted flow curves by TWINLAW for AZ31B alloy under (a) simple shear, (b) tension-compression-tension [70]**.**

After implementing the model into ABAQUS/Standard user material subroutine, Li et al. verified their model by cyclic tension-compression-tension and simple shear experiments on

AZ31B Mg alloy. A single element model and a mesh of 20 elements were employed for cyclic T-C-T and simple shear tests, respectively. The comparisons are shown in Figure 2.17. Correlation between model predictions and experimental results were good, however the transient behaviour was not accurately reproduced. Also, in Figure 2.17(a), the predicted curve showed a normal shape, while the experimental curve exhibits upward concavity. It was claimed that TWINLAW is two orders of magnitude faster than polycrystalline models, but still one order of magnitude slower than fully phenomenological plasticity models with only isotropic hardening [70].

2.2.2.2 Multi-surface hardening

Mroz [71,72] made use of Prager's linear kinematic hardening rule and proposed a hardening rule by introducing the concept of "field of work hardening moduli" in lieu of a constant modulus. To describe the nonlinear stress-strain curves and smooth transition from elastic to plastic region, Mroz's model divides the flow curve into the small linear regions of constant work hardening moduli. Each linear region with a constant work hardening modulus is represented by a yield surface in stress space. Equation for each yield surface can be written:

$$\emptyset_i(\boldsymbol{\sigma} - \boldsymbol{\alpha}_i) - Y_i = 0 \qquad \textbf{(2.29)}$$

where $\boldsymbol{\alpha}_i$ and Y_i are the centers and radii of yield surfaces, respectively. Upon plastic loading, these surfaces, being initially concentric for an isotropic material, will come into contact with each other and move together as long as plastic straining continues (Figure 2.18). The movement of yield surfaces is along the line connecting current stress point and the stress point on the subsequent yield surface with the same outward normal as the current stress point. Major

drawback of the Mroz's model is that since the stress-strain curve of the material is reproduced in a piecewise linear fashion, an infinite number of yield surfaces are required to give a smooth curve, which in turn requires huge memory capacities.

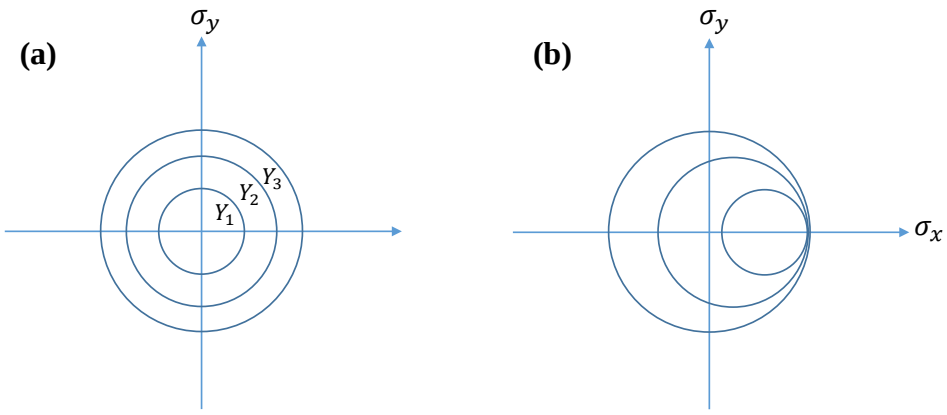

Figure 2.18 Schematic representation of yield surfaces in Mroz's model, (a) unstressed condition, (b) upon uniaxial plastic straining in x-direction.

To overcome the drawback of Mroz's model, Dafalias and Popov [73] and Krieg [74] proposed another hardening rule involving only two yield surfaces: loading surface and bounding surface. These two surfaces, generally, have the same shape and evolve simultaneously in the stress space. In contrast to Mroz's model, they defined plastic modulus under uniaxial loading as a continuous nonlinear function:

$$E^p = \bar{E}^p + h\left(\frac{\delta}{\delta_{in} - \delta}\right) \tag{2.30}$$

where E^p and $\bar{E}^p$ are the plastic moduli of the loading and bounding surfaces, respectively, δ is the gap between current stress point on the loading surface and corresponding stress point on

the bounding surface with the same outward normal as the current stress point, δ_{in} is the initial value of δ (see Figure 2.19) and h is the shape function.

Two-surface hardening model in its original form is not applicable to magnesium alloys with unusual hardening behaviour. To use it with magnesium alloys, Lee et al. [75] modified Dafalias-Popov's model to include three different deformation modes of twinning, de-twinning and slip. In addition to updating δ_{in} upon strain reversal, they considered an update for the gap distance, δ, upon changing the dominant deformation mode. The gap distance, in general, was assumed to depend on initial gap distance, texture evolution history and equivalent plastic strain.

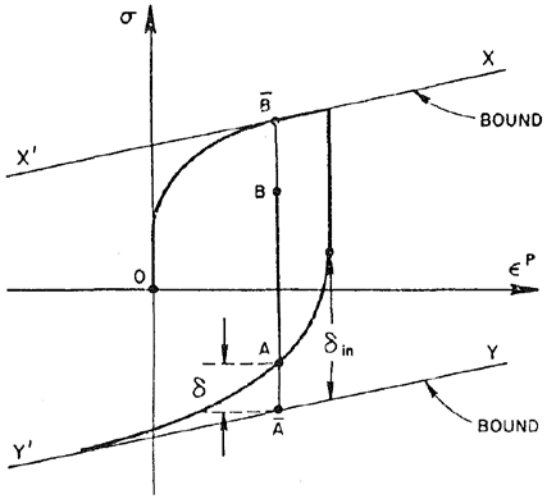

Figure 2.19 Typical stress-plastic strain curve showing δ and δ_{in} [73]**.**

In order to distinguish between three different deformation modes, Lee et al. defined some criteria. The criterion for the onset of twinning under plane stress condition (thickening mode in Figure 2.20) was considered:

$$d\varepsilon^{p}{}_{1} + d\varepsilon^{p}{}_{2} \geq 0 \qquad \textbf{(2.31)}$$

where $d\varepsilon^p{}_{1,2}$ are the principal values of plastic strain increment. On the other hand, de-twinning was assumed to be initiated (thinning mode in Figure 2.20) when following condition is met, provided that the loading history prior to de-twinning satisfies the twinning criterion:

$$d\varepsilon^p{}_1 + d\varepsilon^p{}_2 < 0 \qquad \textbf{(2.32)}$$

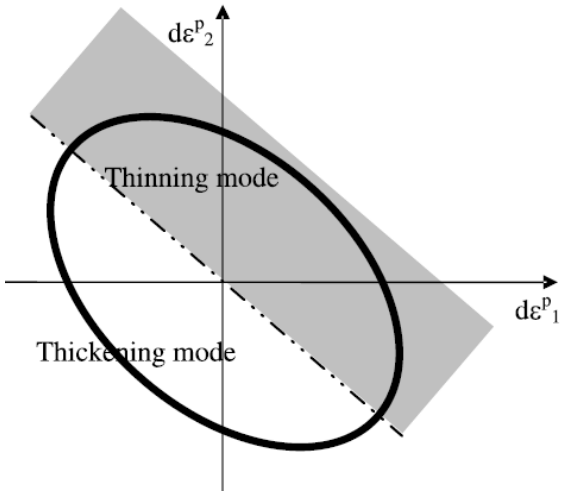

Figure 2.20 Representation of criteria set by Lee et al. for twinning/de-twinning activation [75]

The exhaustion of twinning/de-twinning was assumed to happen when accumulated plastic strain during twinning/de-twinning reaches a critical prescribed value. Deformation states which satisfy neither of the abovementioned criteria were corresponded to slip mode.

In their proposed model, Lee et al. utilized different hardening curves i.e., different functions for gap distances between bounding and loading curves, to account for asymmetry in tension and compression. Under the dominance of de-twinning e.g., during tension following compression, the gap distance was proposed:

$$\bar{\delta} = (1 - \vartheta)(\bar{\Sigma} - \bar{\sigma}_t) \tag{2.33}$$

where, as shown in Figure 2.21, $\bar{\sigma}_t$ is the reference stress, $\bar{\Sigma}$ is corresponding effective stress on bounding surface and ϑ is a sigmoid-type function varying between 0 and 1. Under twinning mode, the gap distance was formulated:

$$\bar{\delta} = \frac{Y^t}{Y^c}\delta_c \tag{2.34}$$

where δ_c is the gap distance during compressive straining and can be found from an equation similar to Equation (2.33). For the slip-dominated mode, a normal exponential-type function for gap distance was utilized:

$$\bar{\delta} = a_s(\bar{\delta}_{in}) + b_s(\bar{\delta}_{in})\exp(-c_s(\bar{\delta}_{in})\bar{\varepsilon}^l) \tag{2.35}$$

where a_s, b_s and c_s are material constants and $\bar{\varepsilon}^l$ is plastic strain updated for each reversal.

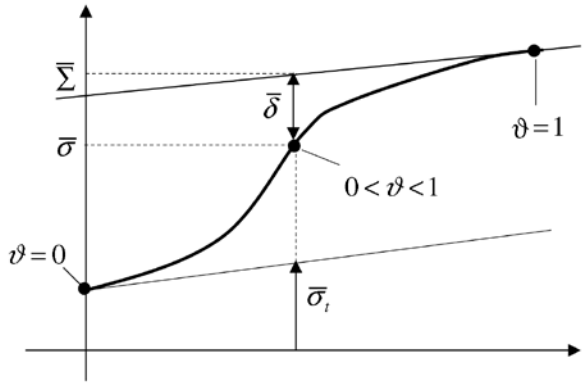

Figure 2.21 Schematic representation of a sigmoid type loading curve defining parameters in Equation (2.32) [75]**.**

Lee et al. employed a modified Drucker-Prager yield criterion for capturing yield asymmetry and anisotropy. Under plane-stress condition, their proposed modification of Drucker-Prager yield criterion included three more anisotropic coefficients; β_2, β_3 and β_4:

$$\phi = p\sqrt{{\sigma_{xx}}^2 - \beta_2\sigma_{xx}\sigma_{yy} + {\beta_2}^2{\sigma_{yy}}^2 + 3{\beta_3}^2{\sigma_{xy}}^2} \qquad \textbf{(2.36)}$$

$$+ q\left(\sigma_{xx} + \beta_4\sigma_{yy}\right) - Y = 0$$

They reported that asymmetry and anisotropy of initial yield stresses for AZ31B magnesium alloys in two different conditions are well-predicted using yield criterion in Equation (2.36) (Figure 2.22(b)).

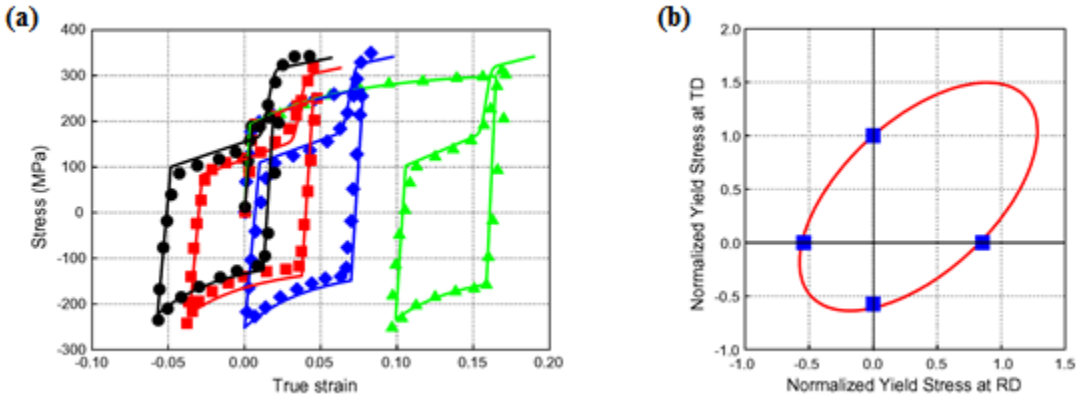

Figure 2.22 (a) Comparisons of the experimental results for AZ31B Mg alloy under tension-compression-tension loading with various amounts of pre-deformation and predictions based on model proposed by Lee et al. (b) Yield locus prediction vs. experimental measurements [76]**.**

Based on the comparisons made between the predicted and experimental uniaxial results under tension-compression-tension and compression-tension with various pre-deformation, Lee et al. concluded that their proposed model was able to reproduce yield asymmetry and unusual

hardening behaviour of AZ31B magnesium alloy. However, as can be seen in Figure 2.22(a), the transient behaviour was not very well captured.

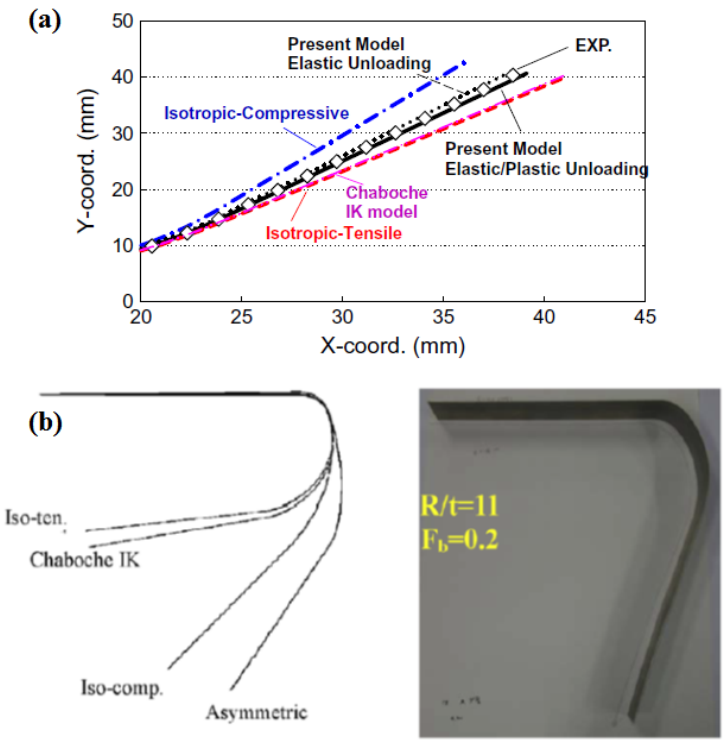

Figure 2.23. Deformed shapes of AZ31B sheets after (a) unconstrained cylindrical bending test, (b) 2D draw bend test.

Furthermore, Lee et al. [76] implemented the proposed model into Abaqus®/Standard with the aid of user material subroutine (UMAT). They employed two different bending tests, i.e., unconstrained cylindrical bending test and 2D draw bend test, to compare springback predictions from their model and other models based on classical isotropic hardening and Chaboche-type nonlinear kinematic hardening. The comparisons are shown in Figure 2.23.

Consequently, they concluded that their developed model gives the best correlation between experimental and simulation results.

Behravesh et al. [77–79] employed two-surface plasticity framework to propose an asymmetric and isotropic model for rolled AZ31B Mg alloy under cyclic loading. To account for yield asymmetry, they used isotropic pressure-insensitive Cazacu-Barlat yield function. Bauschinger effect was incorporated into their model via a combined isotropic-kinematic hardening rule, responsible for adjusting the back stress and the size of the yield surface at the onset of reverse loading.

It was demonstrated by Behravesh et al. that their proposed model implemented into UMAT followed the experimental material response under tension, compression, tension-compression, and tension-compression-tension for different strain amplitudes. They also verified the model results with available solutions, based on VMP method, for one-dimensional and two-dimensional problems.

Utilizing various von Mises yield surfaces, Nguyen et al. [80] made use of the concept of multiple yield surfaces to model the stress-strain response of AZ31B sheets under tension-compression-tension (TCT) and compression-tension-compression (CTC) loading. A separate yield surface was defined for each of the dominant deformation mechanisms, i.e., slip, twinning, and de-twinning. Only one yield surface corresponding to the active dominant mechanism was assumed to be active at any moment. The evolution of yield surfaces was considered according to isotropic hardening, using separate exponential functions for each deformation mode. The validation of the model was performed using TCT tests with different values of pre-tension on

AZ31B sheets, as is depicted in Figure 2.24, and compared with predictions by classical isotropic hardening with a single von Mises yield surface for all deformation modes.

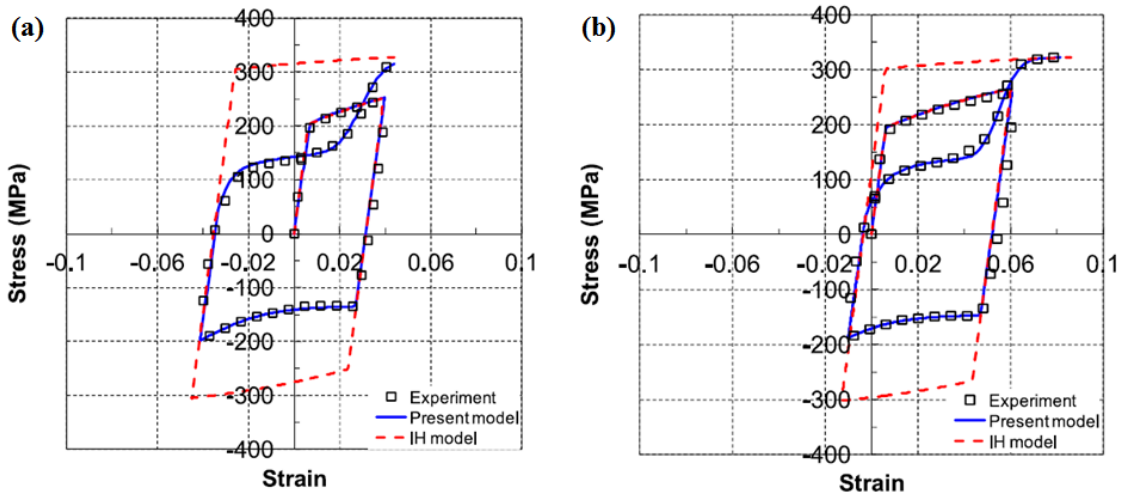

Figure 2.24 Verification of proposed model by Nguyen et al. using TCT tests on AZ31B sheet with different levels of pre-tension [80]**.**

2.2.2.3 Distortional hardening

Muhammad et al. [81] argued that classifying the cyclic hardening behaviour of wrought Mg alloys into different modes according to dominant deformation mechanisms is not general enough for Mg alloys with weaker basal textures, such as ZEK100 containing rare-earth alloying elements. Therefore, they used a classification by applied loading regime, i.e., monotonic loading, reverse compression, and reverse tension. They, however, employed a similar criterion as in Figure 2.20, to determine the active deformation mode.

Three CPB06ex2 yield surfaces corresponding to different deformation modes were defined to evolve by isotropic hardening during monotonic plastic loading. In addition to isotropic expansion of yield surfaces, Muhammad et al. formulated the evolving

anisotropic/asymmetric behaviour of Mg alloy sheets following a methodology proposed by Plunkett et al. [82]. According to this method, anisotropy and strength differential parameters in yield surface formulation was linearly interpolated between discrete levels of accumulated plastic strain, which resulted in yield surface distortion, as in Figure 2.25.

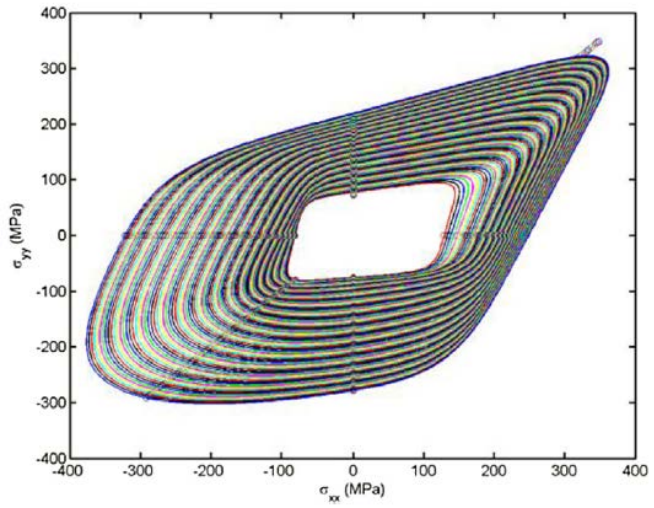

Figure 2.25 Yield surface evolution for annealed ZEK100 sheet during monotonic loading [81]**.**

After implementing into UMAT to use within LS-DYNA® software, the model proposed by Muhammad et al. was utilized to reproduce CTC and TCT experimental results on annealed ZEK100 and AZ31B sheets along RD and TD directions. The model reproductions were deemed acceptable, although some minor discrepancies between results were reported in the unloading-reloading portion of flow curves.

In most previously-reviewed cyclic plasticity models kinematic hardening was responsible for describing Bauschinger effect. Alternatively, Barlat et al. [83] proposed a

constitutive description of cyclic plastic behaviour of materials, called HAH, capable of giving Bauschinger effect, which is not formulated based on kinematic hardening concept, i.e., it does not involve the translation of the yield surface. Through this approach, a homogeneous yield function composed of two distinct parts, namely, a stable part (φ) and a fluctuating part (φ_h), was defined as:

$$\emptyset = (\varphi^q + {\varphi_h}^q)^{\frac{1}{q}} = \left(\varphi^q + {f_1}^q \left|\widehat{\boldsymbol{h}}^{\boldsymbol{s}}{:}\boldsymbol{S} - \left|\widehat{\boldsymbol{h}}^{\boldsymbol{s}}{:}\boldsymbol{S}\right|\right|^q + {f_2}^q \left|\widehat{\boldsymbol{h}}^{\boldsymbol{s}}{:}\boldsymbol{S} + \left|\widehat{\boldsymbol{h}}^{\boldsymbol{s}}{:}\boldsymbol{S}\right|\right|^q\right)^{\frac{1}{q}} = Y \quad \textbf{(2.37)}$$

where q, f_1 and f_2 are parameters and $\widehat{\boldsymbol{h}}^{\boldsymbol{s}}$ is another parameter representing prior deformation history of microstructure, called microstructure deviator, normalized as follows:

$$\widehat{\boldsymbol{h}}^{\boldsymbol{s}} = \frac{\boldsymbol{h}^{\boldsymbol{s}}}{\sqrt{\frac{8}{3}\boldsymbol{h}^{\boldsymbol{s}}{:}\boldsymbol{h}^{\boldsymbol{s}}}} \quad \textbf{(2.38)}$$

For a virgin (unstrained) material, the microstructure deviator was assumed to be equal to the stress deviator after the first increment into the plastic region and stay the same until strain path changes.

Stable component φ in Equation (2.37) can be any homogenous isotropic or anisotropic yield function of degree one, whether symmetric or asymmetric. The homogenous yield function, Equation (2.37), formulated in a way that governs the evolution of yield surface as well as the initial yield locus in stress space. Barlat et al. further explained that this is attained by two evolving parameters f_1 and f_2, as depicted in Figure 2.26, each controlling one side of the yield surface. During forward loading, the yield surface around the active loading state expands in an isotropic hardening manner (side controlled by f_2 in Figure 2.26). At the same

time, f_1 at the opposite side of loading state on the yield surface evolves according to Equation (2.39), making the yield surface flatten on that side:

$$f_1 = (g_1{}^{-q} - 1)^{\frac{1}{q}}, \qquad \frac{dg_1}{dp} = k_2\left(k_3\frac{Y}{\bar{\sigma}} - g_1\right) \tag{2.39}$$

where k_2 and k_3 are constants.

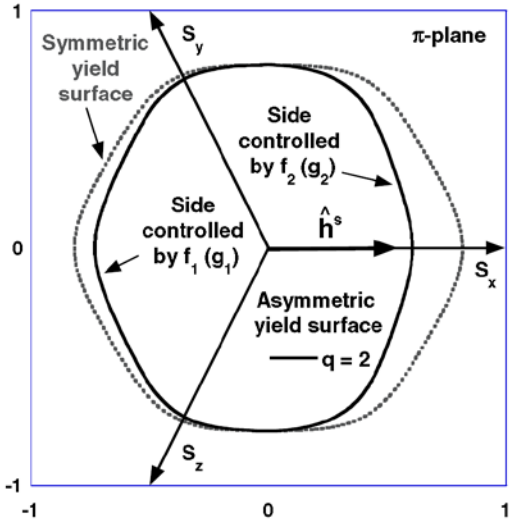

Figure 2.26 Asymmetric yield locus based on HAH model by Barlat et al. with two sides controlling by two different parameters [83]**.**

When loading is reversed (which is manifested in the formulation by a negative value for double-dot product of two tensors $\widehat{\boldsymbol{h}}^{\boldsymbol{s}}$ and $\boldsymbol{S}$), the recovery of flow stress to the approximate level of flow stress during previous loading, takes place. Correspondingly, the evolution rule for g_1 was proposed in the exponential form as:

$$\frac{dg_1}{dp} = k_1\frac{g_1^p - g_1}{g_1} \tag{2.40}$$

where k_1 is a constant, and g_1^p accounts for permanent softening. Similar to the forward loading, flattening of the yield surface occurs on the opposite side to the reverse loading state.

To capture permanent softening, they introduced two extra state variables g_4 and g_5 with evolution equations of the type:

$$\frac{dg_4}{dp} = k_5(k_4 - g_4) \tag{2.41}$$

where k_4 and k_5 are constants. Furthermore, in the case of strain path change without changing the sign of double-dot product $\widehat{\boldsymbol{h}}^{\boldsymbol{s}}$: $\boldsymbol{S}$, it was assumed that the microstructure deviator evolves by rotating towards the new direction for stress deviator. Hence, a possible evolution equation for $\widehat{\boldsymbol{h}}^{\boldsymbol{s}}$ was suggested:

$$\frac{d\widehat{\boldsymbol{h}}^{\boldsymbol{s}}}{dp} = k\left[\widehat{\boldsymbol{S}} - \frac{8}{3}\widehat{\boldsymbol{h}}^{\boldsymbol{s}}\left(\widehat{\boldsymbol{S}} : \widehat{\boldsymbol{h}}^{\boldsymbol{s}}\right)\right] \tag{2.42}$$

where k is a constant and $\widehat{\boldsymbol{S}}$ is normalized in a similar way as Equation (2.38). The aforementioned situation is illustrated in Figure 2.27 for a generic material, where the microstructure deviator rotates as a result of a strain path change from uniaxial tension to balanced biaxial tension.

Lee et al. [84] extended HAH model to describe the hardening behaviour of AZ31B sheet under load path changes. In their model, called HAH-HCP, they made use of CPB06 criterion as the stable component (φ) of the yield function in Equation (2.37), to capture the initial yield asymmetry (strength differential) of AZ31B sheet. Isotropic evolution of yield

surface was specified using two different isotropic hardening laws for tension and compression, respectively:

$$\sigma_T = C_0 \cdot (\bar{\varepsilon} + \varepsilon_0)^n \tag{2.43}$$

$$\sigma_C = A_1 + \frac{(B_1 - C_1)}{1 + exp(|D_1 \cdot (\bar{\varepsilon} - \varepsilon_1)|)} \tag{2.44}$$

where C_0, ε_0, n, A_1, B_1, C_1, D_1, and ε_1 are material parameters. The assignment of Equation (2.43) or (2.44) was decided according to thickening and thinning criteria.

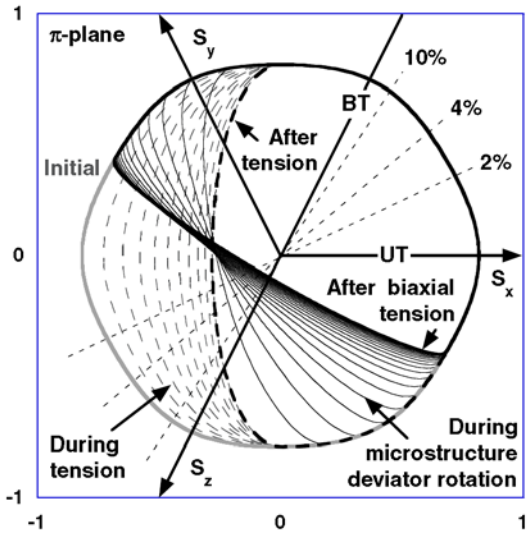

Figure 2.27 The evolution of yield surface in HAH model after strain path change from uniaxial tension to balanced biaxial tension [83]**.**

To reproduce the sigmoidal shape of the flow response of Mg alloy sheets, they proposed the following evolution laws to replace the law in Equation (2.40) when loading direction reversed. Equation (2.45) reproduces transient hardening in the de-twinning-dominated region, and Equation (2.46) captures the s-shape.

$$\frac{dg_u}{dp} = k_1 \frac{(g_{u_1} - g_u)}{g_u} \quad , \quad g_u < g_{u_1} \tag{2.45}$$

$$\frac{dg_u}{dp} = L_u \cdot g_u \left((1 - g_{u_1}) - g_u \right) \quad , \quad g_u \geq g_{u_1} \tag{2.46}$$

$$L_u = L_{ua} \cdot L_{ub} \cdot exp\left({}^{-\bar{\varepsilon}_{twin}}/_{L_{uc}} \right) \tag{2.47}$$

where g_{u_1}, L_{ua}, L_{ub}, and L_{uc} are material constants and $\bar{\varepsilon}_{twin}$ is equivalent strain produced due to twinning.

Figure 2.28 shows the correlations between experimental and simulated results by HAH-HCP for AZ31B sheet subjected to TCT and CTC with pre-strains of 4%. It was stated that HAH-HCP successfully captured the main characteristics of Mg alloy sheet plastic response.

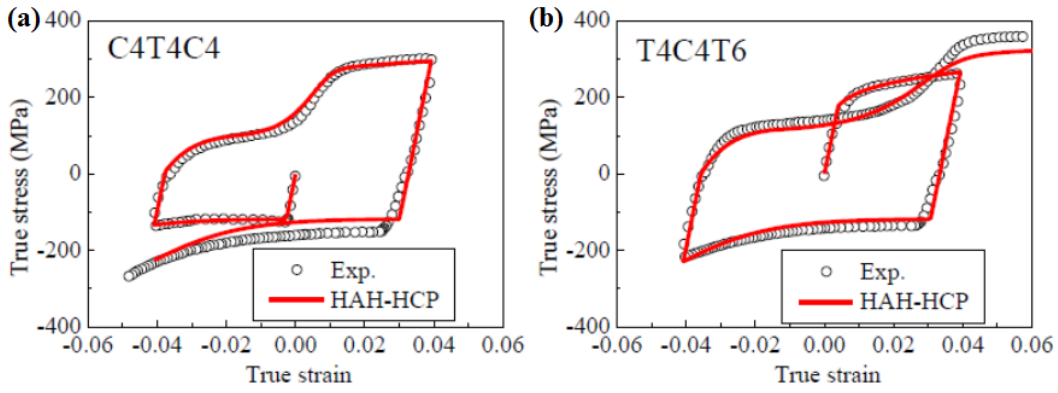

Figure 2.28 HAH-HCP-simulated curves compared with experimental results of AZ31B sheet during (a) CTC, and (b) TCT tests [84]**.**

2.3 **Concluding remarks**

With regard to the review of available phenomenological plasticity models capable of describing unique cyclic plastic behaviour of wrought Mg alloys, the need for developing a new plasticity model may be justified by emphasizing the areas not covered by those models, as follows.

- Multiaxial stress analysis of components requires constitutive formulations in a general state of stress, rather than plane stress state, which would only be applicable to sheets.
- Considering the anisotropic response of wrought Mg alloys, a cyclic plasticity model should take directional behaviour into account and have the capability of being calibrated using experimental results along different directions.
- To be able to use the cyclic plasticity model for applications involving cyclic loading, for instance, the fatigue life estimation of a magnesium control arm in automotive suspension system, axial tension-compression and torsional stabilized hysteresis loops must be utilized to determine the model parameters.
- Response prediction under non-proportional multiaxial cyclic paths associated with complex loading, which is frequently found in automotive suspension and transmission parts has never been verified by plasticity models developed to date.

Chapter 3

Role of loading direction on cyclic behaviour characteristics of AM30 extrusion and its fatigue damage modelling

3.1 Introduction

In recent years, the automotive industries' commitment to reduce vehicle weight, and thereby fuel consumption, has brought more attention to light metals. Other than saving energy, weight reduction reduces greenhouse gas emissions, which, in turn, contributes to the conservation of environment [1]. Magnesium (and its alloys), being the lightest commercially available structural metal (with the density of 1.75 g/cm^3), has undoubtedly been the focal point for this increased interest [2,26,85–87].

Currently, magnesium alloys are widely being applied to automotive components used in vehicle interior, housings and trim parts [6]. Extending current application of magnesium alloys to load-bearing components such as suspension arms requires, on one hand, comprehensive understanding of their plastic behaviour. On the other hand, fatigue modelling is necessary to estimate these components' service life under cyclic loading conditions.

Die casting has been the main manufacturing process for magnesium components [9,10]. Compared to cast products, wrought magnesium alloys have shown enhanced mechanical properties, e.g., tensile and fatigue properties [4,13,88,89]. However, the development of

preferred orientation (texture) upon conventional forming/processing applications such as rolling and extrusion, renders their cyclic plastic and fatigue behaviour dependent on the loading direction. In this context, a number of previous researches have been dedicated to the anisotropic fatigue characteristics of wrought magnesium alloys along different directions [89–96].

Sajuri et al. [89] carried out stress-controlled cyclic tests on AZ61 extrusion along extrusion (ED), transverse (TD) and 45° to the ED and reported a higher fatigue strength in the ED compared to those in other directions. Lv et al. [92,93] investigated the strain-controlled cyclic response of rolled AZ31 alloy in rolling (RD) and transverse directions. They observed that under the same total strain amplitude, the cyclic stress amplitudes of TD specimens were higher than those of RD specimens, while fatigue lives under both stress- and strain-controlled cyclic loadings were longer for TD. They, further, showed that strain-life data along both directions could be described by separate Coffin-Manson relations, but did not attempt to model consolidated fatigue damage data. In another study by Park et al. [91], rolled AZ31 Mg alloy plate was subjected to strain-controlled cyclic tests along RD and ND (normal to the plate). The ND was seen to exhibit superior fatigue resistance, which was ascribed to the beneficial compressive mean stress during cyclic deformation along ND. It was also concluded that total strain energy density (defined as the addition of positive elastic and plastic strain energy densities) as damage parameter was capable of correlating consolidated fatigue damage data considering directional anisotropy. A more recent work by Park et al. [90] on the same rolled AZ31 alloy plate under stress-controlled cyclic testing reported shorter fatigue life for ND specimens in comparison with RD specimens. They attributed this to the greater extent of plastic

strain accommodation by twinning due to lower twinning stress while loading along ND. Lin et al. [97,98] explored the influence of sampling direction on the low-cycle fatigue life of hot rolled AZ91 alloy under stress-controlled cyclic tests with various stress ratios and peak stresses. Their results indicated that the fatigue lives of TD specimens were longer than those of RD specimens under all test conditions. Furthermore, they successfully used a modified Basquin model with two separate sets of parameters extracted from RD and TD data to estimate the experimental life. Finally, it was reported by Jordon et al. [94] that even though AZ61 extrusion, under the influence of texture, exhibited a slightly greater high-cycle fatigue resistance along ED compared to ND, inclusion size was the decisive parameter in obtained experimental fatigue life. They stated that fatigue behaviour differences along ED and ND could be captured by incorporating the differences in grain orientation and size, particle size and cyclic hardening parameters into a multistage fatigue (MSF) model.

Wrought AM30 magnesium alloy is a Mg-Al-Mn alloy system developed by Luo and Sachdev in 2007 [3]. Henceforth, very limited number of studies [4,5,99–101] have been conducted on its cyclic and fatigue behaviour. Begum et al. [4] and Luo et al. [5] performed strain-controlled cyclic tests on an extrusion piece along ED at strain amplitudes between 0.1% and 0.6% and observed cyclic hardening and asymmetric hysteresis loops at high strain amplitudes. It was stated by the former study that Coffin-Manson and Basquin rules could be used to describe fatigue life. The effect of crystallographic orientation on fatigue of AM30 alloy crash rail extrusion was explored by Jordon et al. [99] through strain-controlled cyclic tests with amplitudes between 0.2% and 0.5%. Based on their results, the stress amplitude as well as mean

stress for ED specimens (with most of basal planes parallel to loading direction) were higher than those in ND (with most of basal planes perpendicular to loading direction), and the ND specimens exhibited slightly better fatigue properties compared to ED ones. Moreover, in a parallel paper on AM30 extrusion under the same conditions, Lugo et al. [102] employed MSF model, with parameters calibrated separately for ED and ND, to fit experimental strain-life curves.

In spite of abovementioned literature on cyclic and fatigue characteristics of AM30 alloy, there is still lack of knowledge on its low-cycle fatigue response at high strain amplitudes up to 2.3%. More importantly, to the best of authors' knowledge, the in-plane (processing plane parallel to the basal planes of majority of crystals) fatigue and cyclic anisotropy, corresponding to different behaviour in ED and TD, has never been researched before. Fatigue damage modelling that incorporates material orientation is also lacking. The intent of present chapter is, therefore, to look comprehensively into the orientation-dependent cyclic flow and fatigue behaviour of AM30 alloy extrusion along ED and TD, as well as cyclic damage analysis and fatigue life modelling.

3.2 Materials and methods

3.2.1 Material and specimen

The material selected for current investigation is AM30 magnesium alloy processed by hot extrusion as detailed in [3]. The chemical composition of the experimental AM30 alloy is listed in Table 3.1.The flat specimens for monotonic and cyclic tests with the geometry sketched

in Figure 3.1, were machined from the extrusion section along two orthogonal directions i.e., extrusion (ED) and transverse (TD), corresponding to regions ‘A’ and ‘B’ in Figure 3.2, respectively.

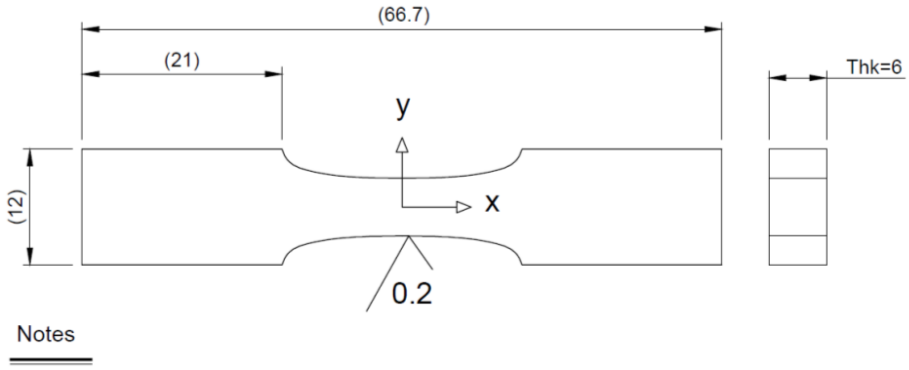

x (mm)	y (mm)	x (mm)	y (mm)
0.00	3.00	8.38	3.49
0.68	3.00	9.14	3.63
1.37	3.01	9.93	3.82
2.05	3.01	10.69	4.05
2.74	3.03	11.36	4.37
3.42	3.04	11.77	4.71
4.11	3.07	12.01	4.98
4.80	3.11	12.25	5.34
5.50	3.15	12.52	6.00
6.20	3.20	33.35	6.00
6.91	3.28	33.35	0.00
7.64	3.37		

Notes

1. All dimensions are in (mm) except the surface roughness which is in micro-meter.
2. Curvature of the reduced section is determined by the coordinates shown in the table.
3. Axes x and y are axes of symmetry.

Figure 3.1 Specimen geometry for tensile and fatigue tests.

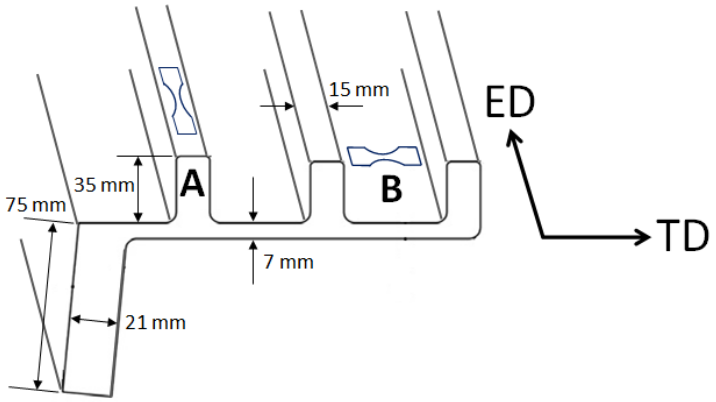

Figure 3.2 Schematic view of AM30 extrusion profile with locations of ED and TD specimens specified with letters ‘A’ and ‘B’, respectively.

Prior to microstructure observation via optical microscope, metallographic samples were manually ground using SiC papers and then sequentially polished with 6, 3, 1 and 0.1 μm

diamond pastes. For the purpose of revealing grain (twin) boundaries in the microstructure, acetic-picral etchant solution (4.2 *g* picric acid, 10 *mL* acetic acid, 10 *mL* distilled water, 70 *mL* ethanol) was used. A typical initial microstructure of the experimental AM30 alloy (away from the surface) is shown in Figure 3.3. According to this figure, twin-free grains with bimodal size distribution are observed. A similar microstructure for AM30 extrusion was reported along ED and TD [5]. It was also reported that the top and bottom surfaces of the extrusion section consisted of larger grains than that of center region [4]. This has been heeded, for comparative purposes, while machining the specimens.

Table 3.1 AM30 chemical composition (wt. %).

Al	Mn	Zn	Fe	Cu	Ni
3.4	0.33	0.16	0.0026	0.0008	0.0006

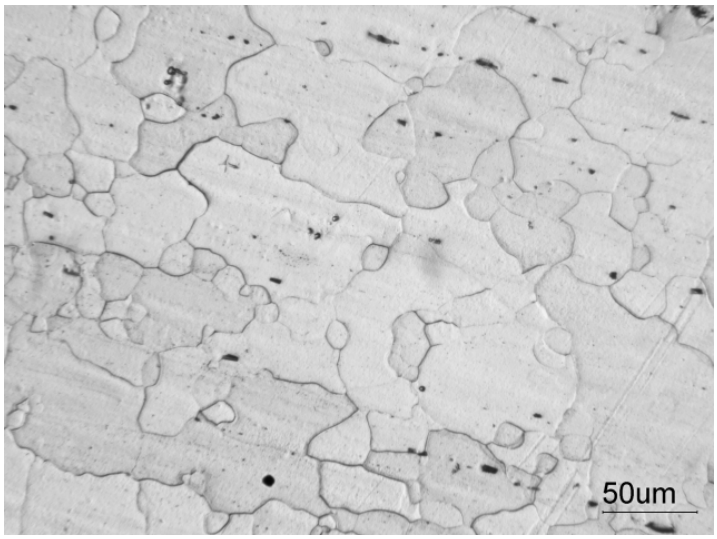

Figure 3.3 Initial twin-free microstructure of experimental AM30 alloy (away from the surface of extrusion section).

Texture measurements were carried out on a Bruker D8 Discover X-ray diffractometer equipped with a VÅNTEC-500 2D detector using Cu-K_α beam radiation at 40 *kV* and 40 *mA*. The use of area detector enabled automated defocusing and background corrections of peak profile. The initial textures of regions 'A' and 'B' of the extrusion section represented by pole figures of basal (0002) and prismatic $(10\bar{1}0)$ poles are displayed in Figure 3.4(a) and (b), respectively. Both regions evince strong basal textures, with the majority of crystals having their c-axes tilted about 20° from ND toward ED in Figure 3.4(a) and nearly perpendicular to ED in Figure 3.4(b).

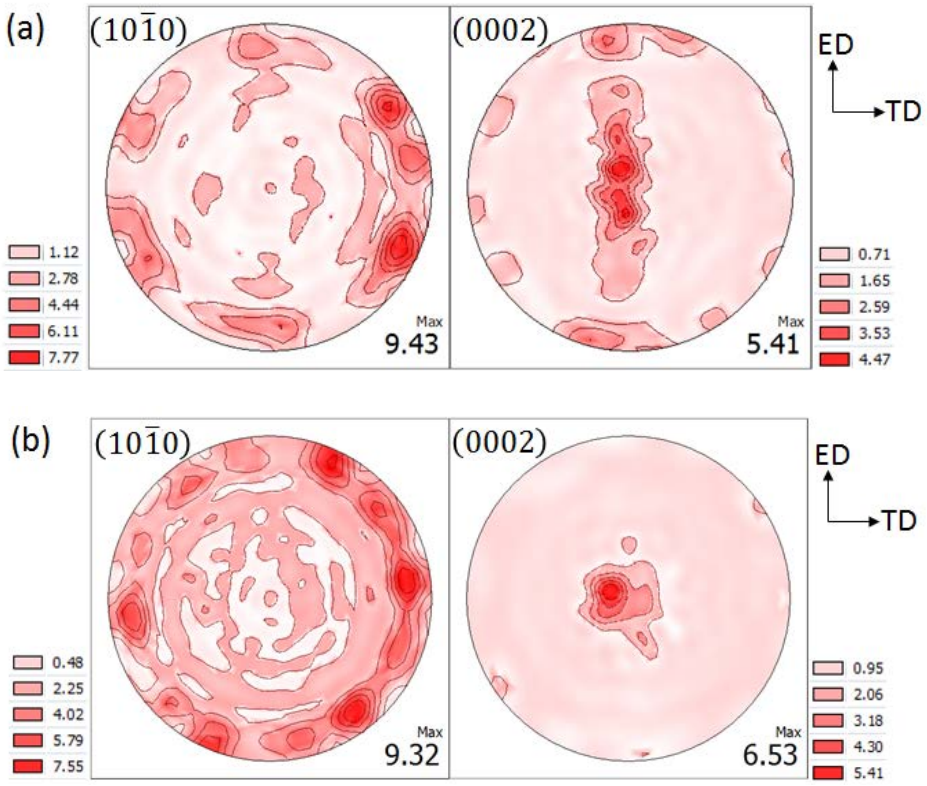

Figure 3.4 (0002) and $(10\bar{1}0)$ pole figures of AM30 extrusion at locations (a) 'A', and (b) 'B'.

3.2.2 Fatigue testing setup

Fatigue testing was performed on an Instron 8874 servo-hydraulic load frame with 25 *kN* axial force capacity. Fully reversed ($R_\varepsilon = -1$) strain-controlled tension-compression (pull-push) cyclic tests, as per ASTM standard E606, were conducted at ambient temperature. The tests were run at varying frequencies between 0.02 and 0.2 *Hz* depending on the applied strain amplitude. Engineering strain values were recorded and controlled through a uniaxial extensometer with gauge length of 10 *mm* and travel of ±0.8 *mm*. At very low strain amplitudes, after material stabilized, i.e., when the maximum and minimum loads of each cycle stayed unchanged from one cycle to the next, tests were switched to load-controlled cycling at higher frequencies up to 15 *Hz*. Test stopping criteria were considered either final rupture of the specimen or 50% load drop. Afterwards, the final fracture surfaces were inspected for crack initiation and propagation mechanisms employing scanning electron microscope (SEM) in secondary electron (SE) mode.

3.3 Results

3.3.1 Monotonic tensile behaviour

The monotonic uniaxial stress-strain response of the AM30 extrusion along ED and TD are given in Figure 3.5(a). The initial portions of the curves (up to the axial strain of 0.05), which is of more importance to the argument being made by this study, are redrawn in Figure 3.5(b). A noticeable yielding anisotropy is present between ED and TD. Yield stress (0.2% offset) along ED is measured to be roughly twice that along TD (200 *MPa* as against 117

MPa). Since loading orientation is not preferable for twinning activation, the yielding anisotropy hints at the activation of different slip systems during tension along ED and TD. Employing crystal plasticity simulations to calculate Schmid factor for various slip systems during tensile deformation of magnesium alloys with similar texture as the one under investigation, it was concluded by other researchers [16,99] that basal slip $\{0001\}\langle 11\bar{2}0\rangle$ and prismatic slip $\{10\bar{1}0\}\langle 11\bar{2}0\rangle$ are predominant slip mechanisms for accommodating tensile strain along TD and ED, respectively. This seems to contradict the very high critical resolved shear stress (CRSS) for prismatic slip at room temperature. It was, however, reported that aluminum as alloying element in Mg-Al alloys facilitated room-temperature slip on prismatic planes at the same time with strengthening of basal planes against slip [17,103–105]. Higher CRSS for slip on prismatic planes at room temperature is then expected to reflect the observed yielding behaviour.

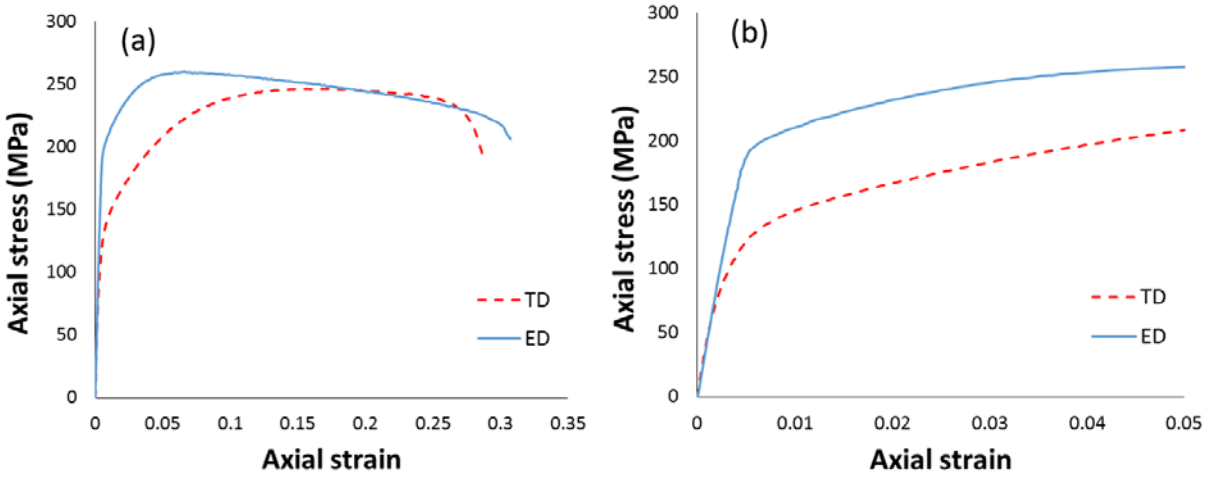

Figure 3.5 (a) Tensile stress-strain curves of AM30 extrusion with loading direction along ED and TD, (b) Zoomed-in details up to 5% strain.

3.3.2 Fully reversed strain-controlled cyclic test results

3.3.2.1 Extrusion Direction (ED)

Figure 3.6 shows the half-life stress-strain hysteresis loops of AM30 Mg alloy extrusion specimens cut along ED under fully reversed strain-controlled pull-push tests at different strain amplitudes ranging from 0.3% to 2.3%. The shapes of half-life hysteresis loops at various strain amplitudes are mainly dictated by the occurrence and exhaustion of twinning and de-twinning as governing plastic deformation mechanisms. At low strain amplitudes of 0.3% and 0.4%, very little plastic deformation can be detected. Judging by the absence of macroscopic flow manifestation of twins, the plastic deformation should principally be accommodated by basal and non-basal slip systems [106,107] with predominance of prismatic slip as was stated before. This means that the compressive stress of -118 *MPa* under the strain amplitude of 0.4% is obviously not enough to get the twins dominantly activated at the half-life. However, the strain amplitude of 0.5% provides sufficient stress (-124 *MPa*) to trigger extension twinning $\{10\bar{1}2\}\langle 10\bar{1}1\rangle$ and de-twinning in the compressive and tensile reversals, respectively. Henceforth, marked flow asymmetry under tension and compression is observed. De-twinning during tensile reversals (for $\varepsilon_a \geq 0.5\%$) happens readily inside the twinned portion of grain and results in a decreased hardening rate [108–110]. Upon de-twinning exhaustion, slip takes over and the hardening rate is subsequently increased, causing an inflection point in the tensile reversal. The increased hardening rate is known to be due to the rotation of crystals to hard orientations for higher order slip and the activation of compression twinning $\{10\bar{1}1\}\langle 10\bar{1}2\rangle$ [19,105,111–113]. The same inflection point in the compressive reversal, attributed to the

saturation of twinning, is observed for strain amplitudes greater or equal to 1.5%. Similarly to the tensile reversal, slip plays the major role upon saturation of twinning as deformation mechanism. Impeding dislocation movements by twin boundaries, then, contributes to the higher hardening rate of the flow curve. This results in attenuated flow asymmetry between tension and compression at high strain amplitudes, as is seen from Figure 3.8(c).

The variations of stress amplitude and mean stress for specimens along ED during strain-controlled pull-push tests are plotted in Figure 3.7. Generally, AM30 alloy extrusion hardens under cyclic straining along ED [4,99]. This may be related to the formation of residual twins during successive processes of twinning and de-twinning in each cycle [108]. To be more specific, the hardening response changes with strain amplitude. Accordingly, three distinct types of hardening behaviour can be inferred from Figure 3.7(a). Firstly, at strain amplitudes of 0.3% and 0.4%, stress amplitude is constant during the initial 10 cycles, then the material slightly hardens before reaching to stability again. As is shown in Figure 3.8(a), at 0.3%, deformation starts with twinning during compression and de-twinning in tensile reversal. This leads to the formation and build-up of residual twins after each cycle, which brings about the cyclic hardening. When twinning gets deactivated, the residual twin build-up and hardening cease. Secondly, at strain amplitudes between 0.5% and 1%, an increasing trend for stress amplitude is observed with progression of straining. Finally, strain amplitudes greater or equal to 1.5% (Figure 3.8(c)) will cause the material to harden at first, and then become stable until failure. This points out that the capacity of microstructure for residual twins is saturated [108].

Mean stress variations with cyclic deformation corresponding to the mentioned three ranges are: no change or gradual increase for low strain range, rapid increase or no change for medium strain range, and rapid decrease for high strain range (Figure 3.7(b)). The increasing trend for mean stress with cycling can be corresponded to the increase in peak stress in tensile reversal. This phenomenon has been argued to be due to the transformation of mobile dislocations in parent matrix to immobile ones in the substructure of $\{10\bar{1}2\}\langle 10\bar{1}1\rangle$ tension twins upon 86.3° lattice rotation [114,115]. The rationale behind the observed decaying of mean stress with cyclic test progression at high strain amplitudes will be discussed later.

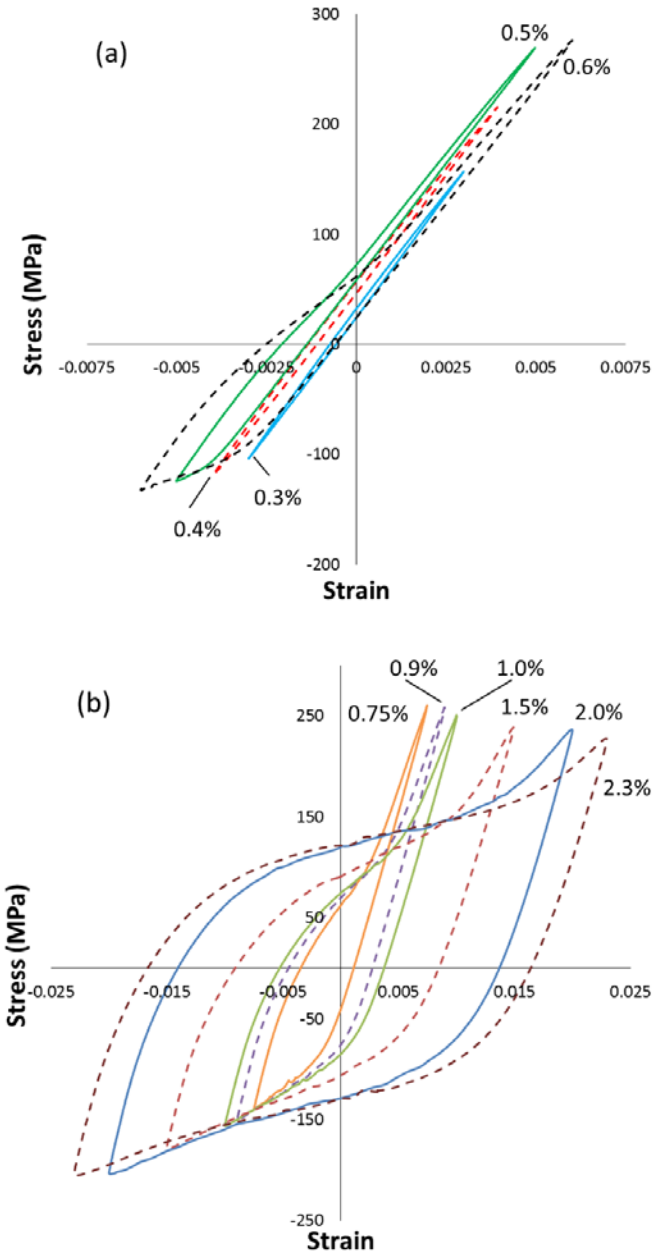

Figure 3.6 Half-life hysteresis loops of AM30 extrusion tested at various strain amplitudes along ED.

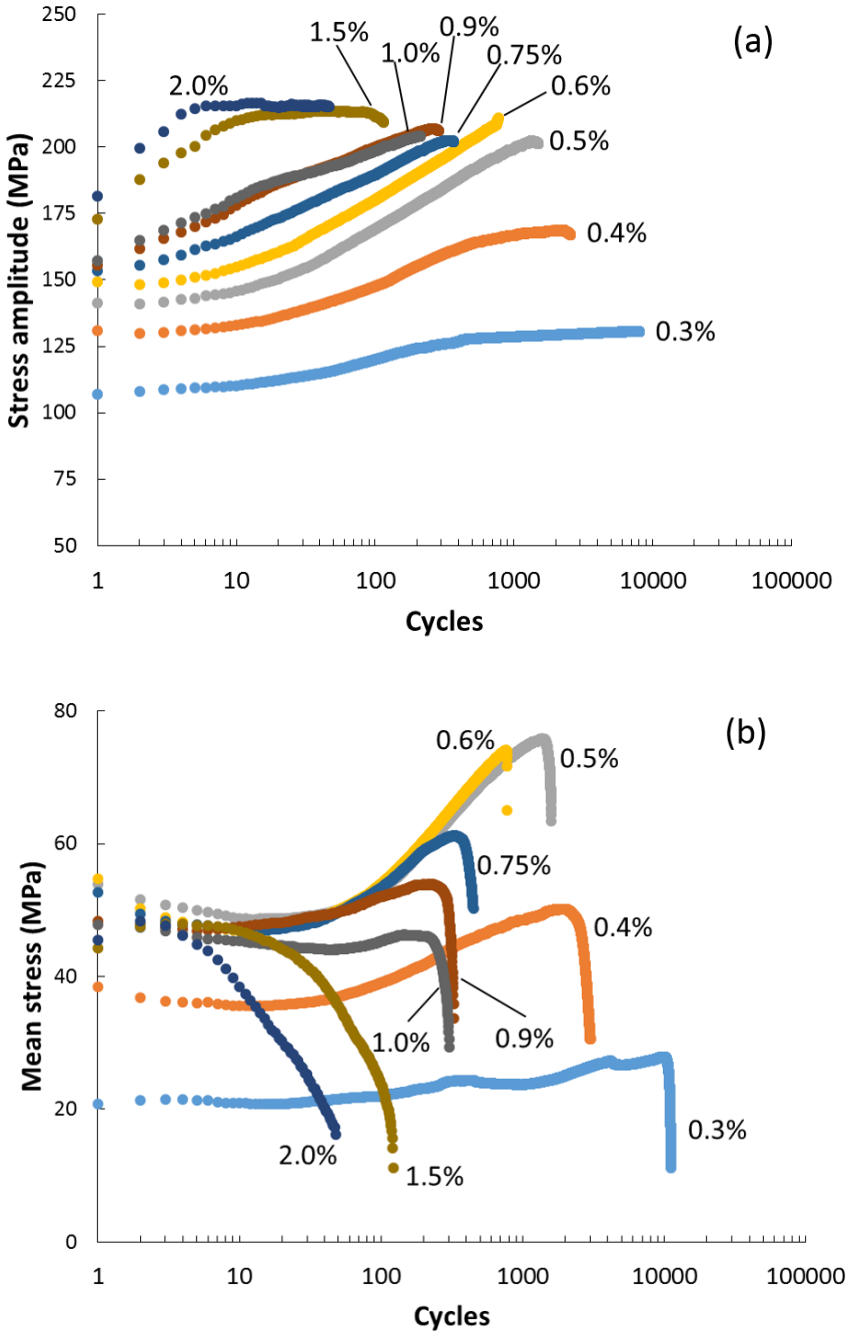

Figure 3.7 Variations of (a) stress amplitude and (b) mean stress with number of tension-compression cycles at various strain amplitudes along ED.

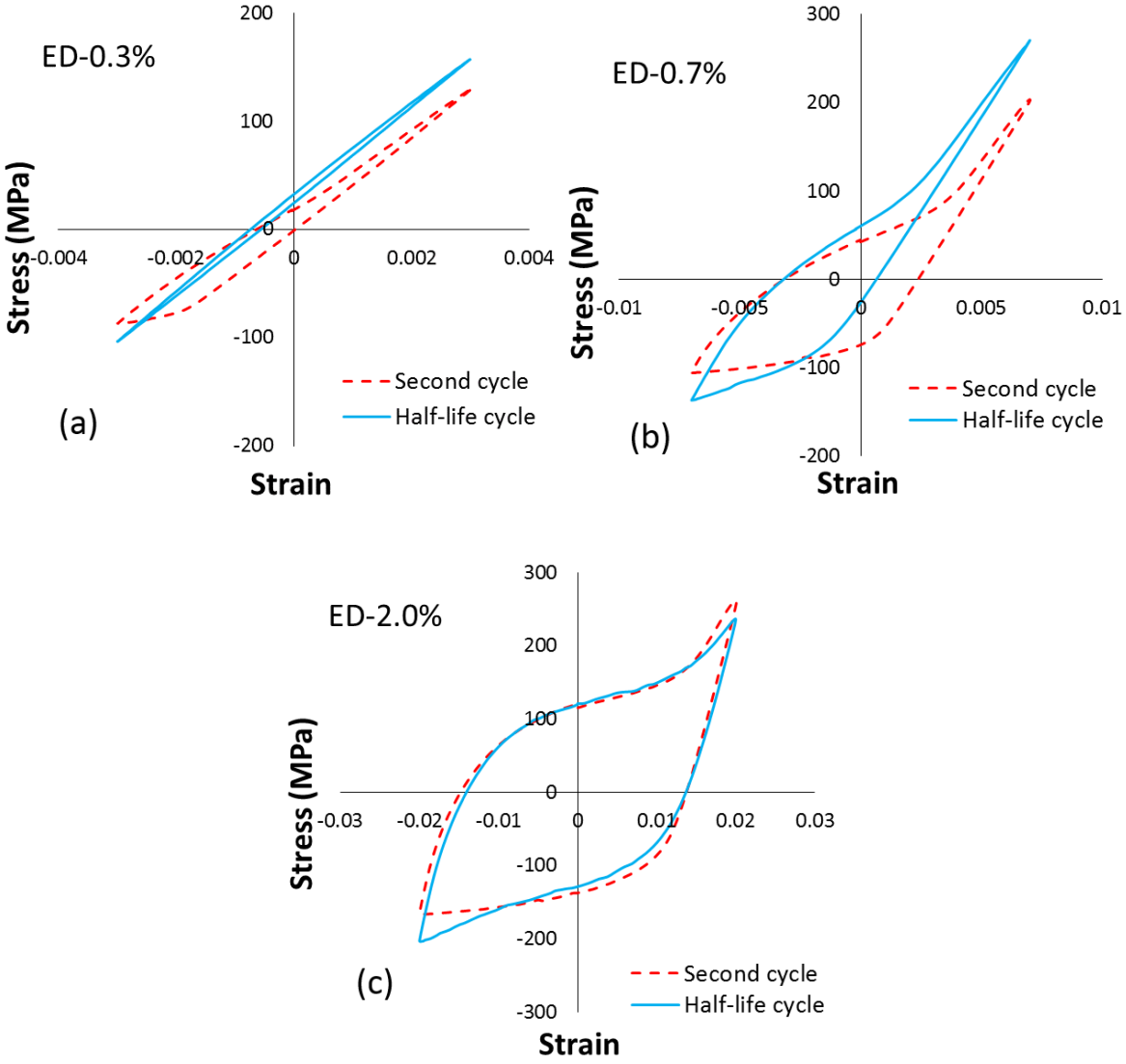

Figure 3.8 Typical hysteresis loops of ED specimens at second and half-life cycles during cyclic tests at (a) low, (b) intermediate, and (c) high strain amplitudes.

3.3.2.2 Transverse Direction (TD)

The half-life stress-strain hysteresis loops of AM30 Mg alloy extrusion specimens tested under the same conditions as Figure 3.6 but along TD, are illustrated in Figure 3.9. According to Figure 3.9(a), twinning becomes the predominant plastic deformation mode at strain

amplitudes equal to or greater than 0.5% corresponding to the compressive stress of -118 *MPa*. This stress level was seen to be insufficient for twinning activation in ED. Since CRSS for twinning is much higher than that for basal slip, TD specimens, which are more favourably oriented for basal slip, exhibit lower stress levels during compression [16]. From another point of view, the lower compressive stress in TD can be, indirectly, connected with the lower extent of twin formation.

Below 0.5%, hysteresis loops exhibit considerable plastic strain being primarily accommodated by basal slip. Moreover, twinning exhaustion, which is depicted by the inflection point in the compressive reversal, is observed for strain amplitudes higher than 1.2%.

Plots of stress amplitude and mean stress variations against number of cycles illustrated in Figure 3.10, confirm the overall hardening of AM30 extrusion along TD. As in ED, three types of hardening behaviour can be identified. The strain amplitudes of 0.3% (Figure 3.11(a)) and 0.4% are characterised with no hardening associated with mean stress decay during initial 10-20 cycles followed by gradual increase in both hardening rate and mean stress. Similar to behaviour in ED, residual twins' formation are believed to be the reason. Between 0.5% and 1.5%, cyclic hardening occurs throughout the whole life with increasing or steady mean stress. Typical second and half-life cycles related to this type of behaviour is shown in Figure 3.11(b). At high strain amplitudes of 2% (Figure 3.11(c)) and 2.3%, the hardening essentially ceases after 10 cycles as a result of residual twin saturation. It is noteworthy that hardening saturation happens at a larger strain amplitude along TD than ED. This delayed saturation is consistent with the less favourability of twinning in compression along TD. For these high strain

amplitudes, mean stress evolution shows a sustained decrease up until failure, which will be discussed hereunder.

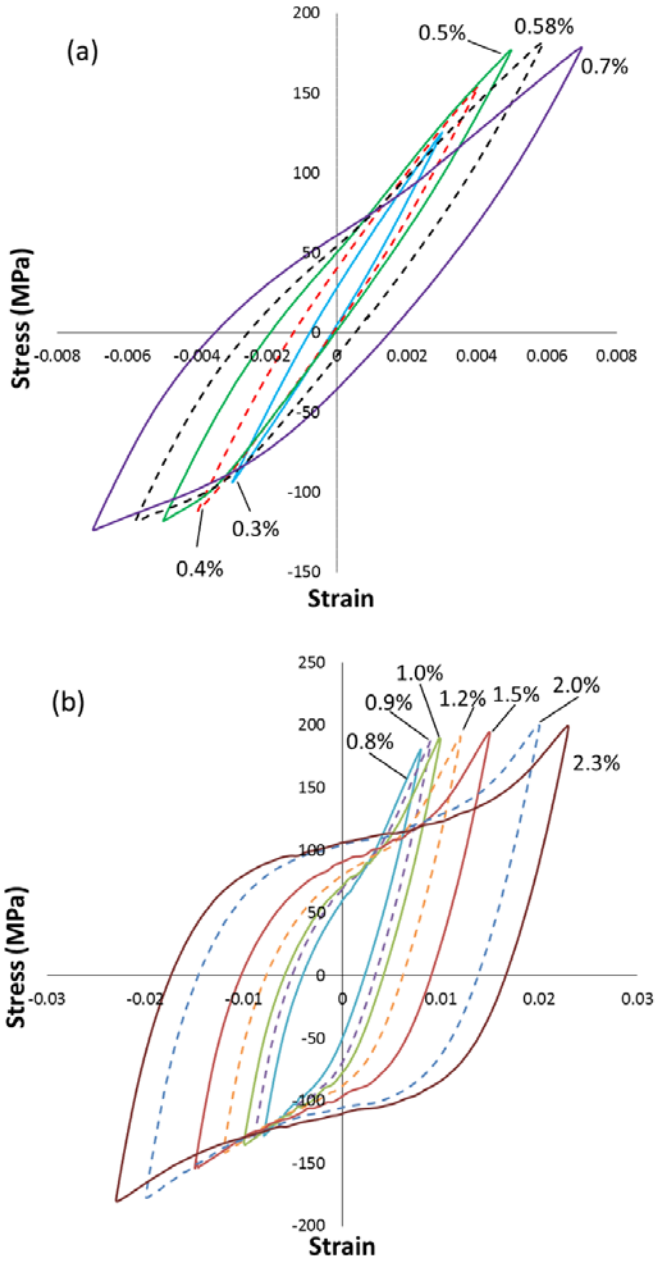

Figure 3.9 Half-life hysteresis loops of AM30 extrusion tested at various strain amplitudes along TD.

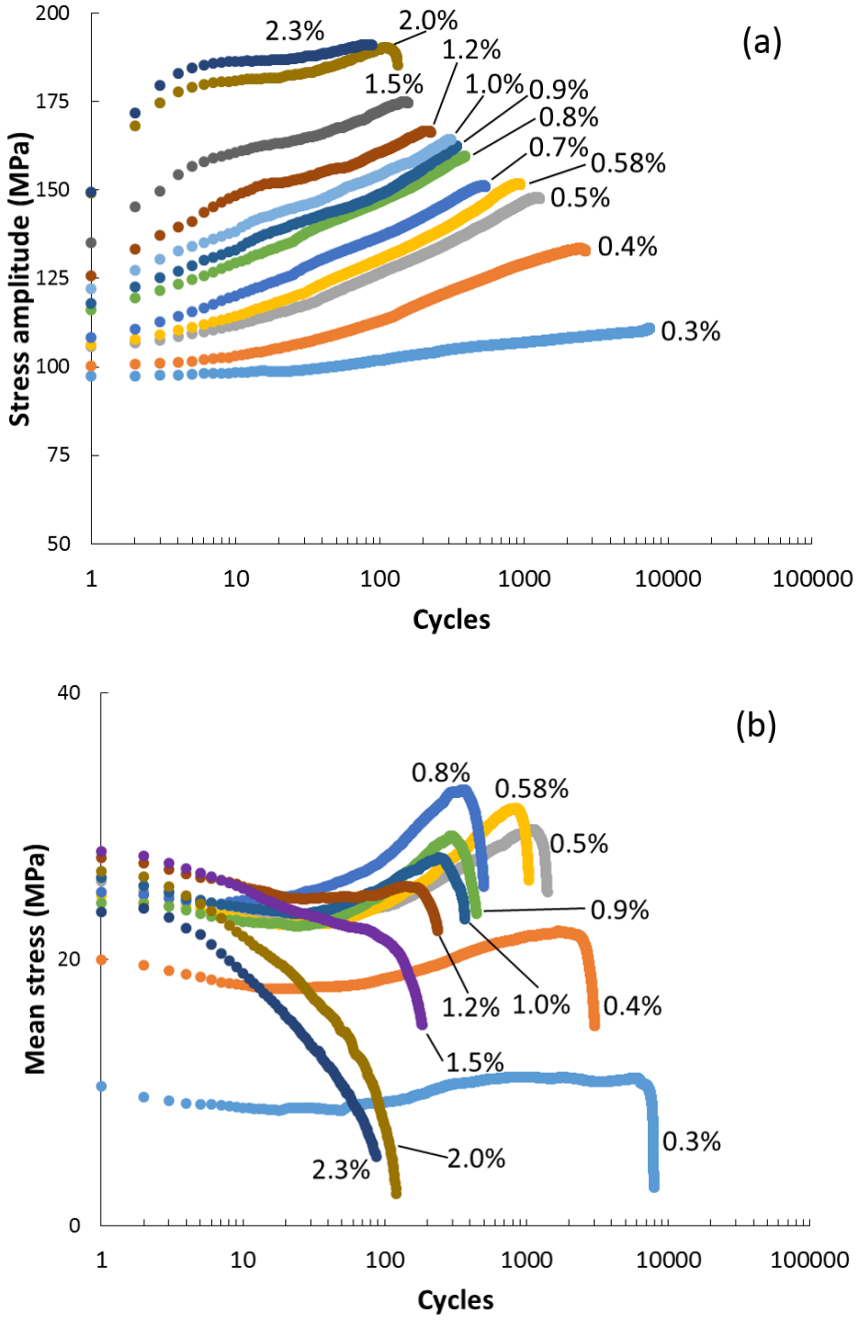

Figure 3.10 Variations of (a) stress amplitude and (b) mean stress with the number of tension-compression cycles at various strain amplitudes along TD.

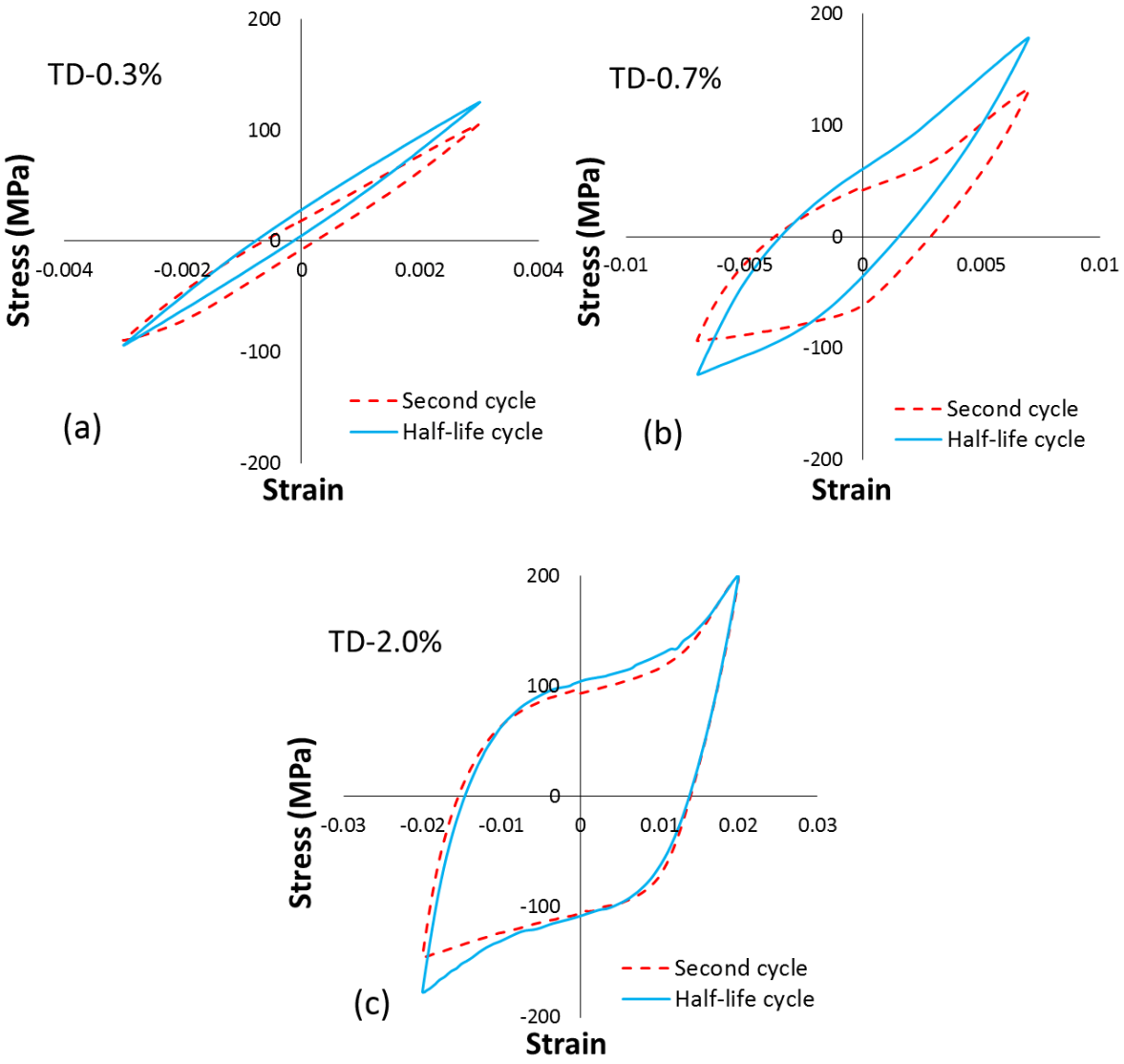

Figure 3.11 Typical hysteresis loops of TD specimens at second and half-life cycles during cyclic tests at (a) low, (b) intermediate, and (c) high strain amplitudes.

3.3.3 Microstructure and texture analyses

Typical optical micrographs of AM30 Mg alloy extrusion tested under low and high strain amplitudes are presented in Figure 3.12. Figure 3.12(a) and (b) show the microstructures of ED specimens tested at strain amplitudes of 0.3%.and 2%, respectively. Twin-free grains in

the microstructure of specimen subjected to low strain amplitude of 0.3% (Figure 3.12(a)) confirms the predominance of slip mechanism mentioned before in the context of hysteresis shapes. However, some traces of residual twins can be evidenced inside the microstructure (shown by arrows), which is in line with the stress amplitude evolution with cycling at low strain amplitudes described earlier. The irregular stepped appearance of these twins is most likely due to the interaction of twinning dislocations on twin boundary and defects such as dislocation pile-ups in matrix during slip-driven deformation [115,116]. Contrary to low strain amplitude, microstructure at high strain amplitude (Figure 3.12(b)) displays extensive twinning (mainly c-axis tension twins $\{10\bar{1}2\}\langle 10\bar{1}1\rangle$ judging by their lenticular morphology [5,117]) inside almost all grains. As is seen, the twins consume their parent grains and in some grains twins in different orientations intersect each other. Besides, twins without visible boundaries, shown by arrows in Figure 3.12(b), indicate the occurrence of twin growth and coalescence, as discussed in [118,119].

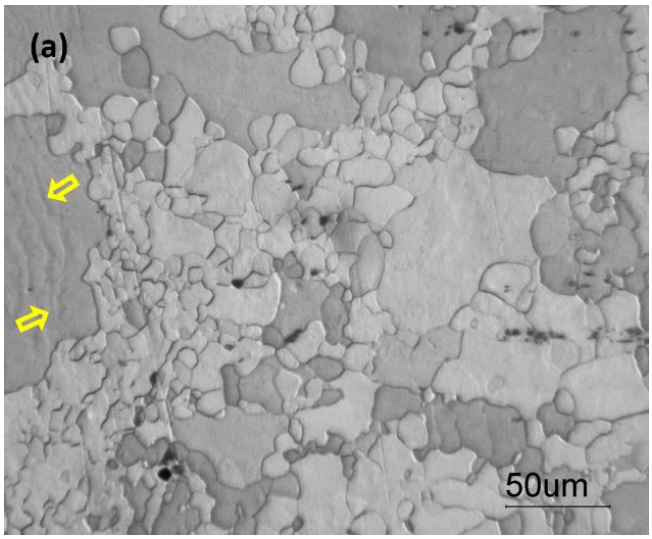

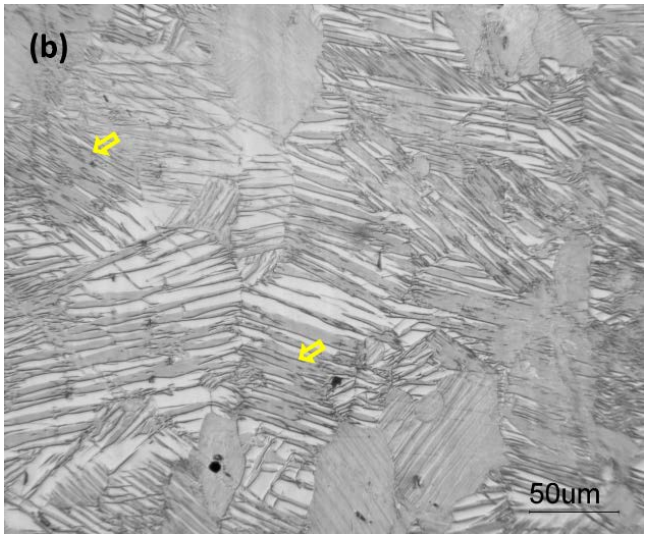

Figure 3.12 Optical microstructures after cyclic pull-push tests along ED at (a) 0.3%, and (b) 2%.

Figure 3.13 shows texture measurements represented by pole figures of basal (0002) and $(10\bar{1}0)$ prismatic poles for specimens tested at various strain amplitudes and along different directions: (a) 0.3% in ED, (b) 2% in ED, (c) 0.3% in TD and (d) 2% in TD. The XRD measurements were done on sections far away from the final fracture surface. It should also be mentioned that all the specimens used for texture analysis had been fractured under tension. Comparing pole figures in Figure 3.13(a) and (c) with as-extruded ones (Figure 3.4) reveals that, in general, the main texture components are preserved after cyclic straining at 0.3%, which is in accordance with slip being the predominant deformation mode as was previously assumed. Furthermore, it is seen that some of the basal poles are oriented from nearly normal/normal direction (ND) towards ED. This change in orientation cannot be related to slip. It can, however, be justified by twinning, which causes the basal planes to rotate 86.3°. The observation of

residual twins in the microstructure shown in Figure 3.12(a) corroborates the mentioned justification.

On the other hand, texture of the specimens subjected to the strain amplitude of 2% represented by pole figures in Figure 3.13(b) and (d), indicates a drastic change in the texture, which can be ascribed to the occurrence of profuse extension twinning. This change is realized by vanishing of most of the basal poles in the center (ND) of (0002) pole figures and formation of new components along TD and ED, for specimens tested in ED and TD, respectively. In other words, the c-axes of the majority of grains are rotated away from the straining direction and oriented against compression [120]. This is the favourable orientation for the activation of bulk extension twinning during the next compressive reversal. Additionally, higher maximum intensity of basal poles in Figure 3.13(b) (10.62 multiples of uniform distribution, MUD) compared to Figure 3.13(d) (8.05 MUD) is indicative of higher extent of twinning/de-twinning during deformation along ED.

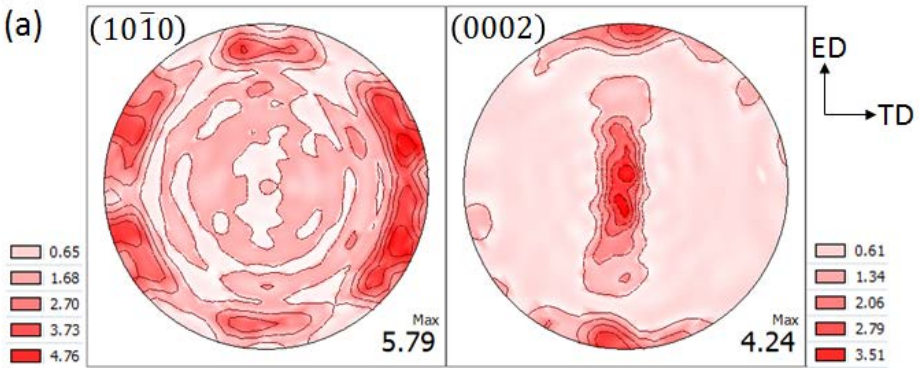

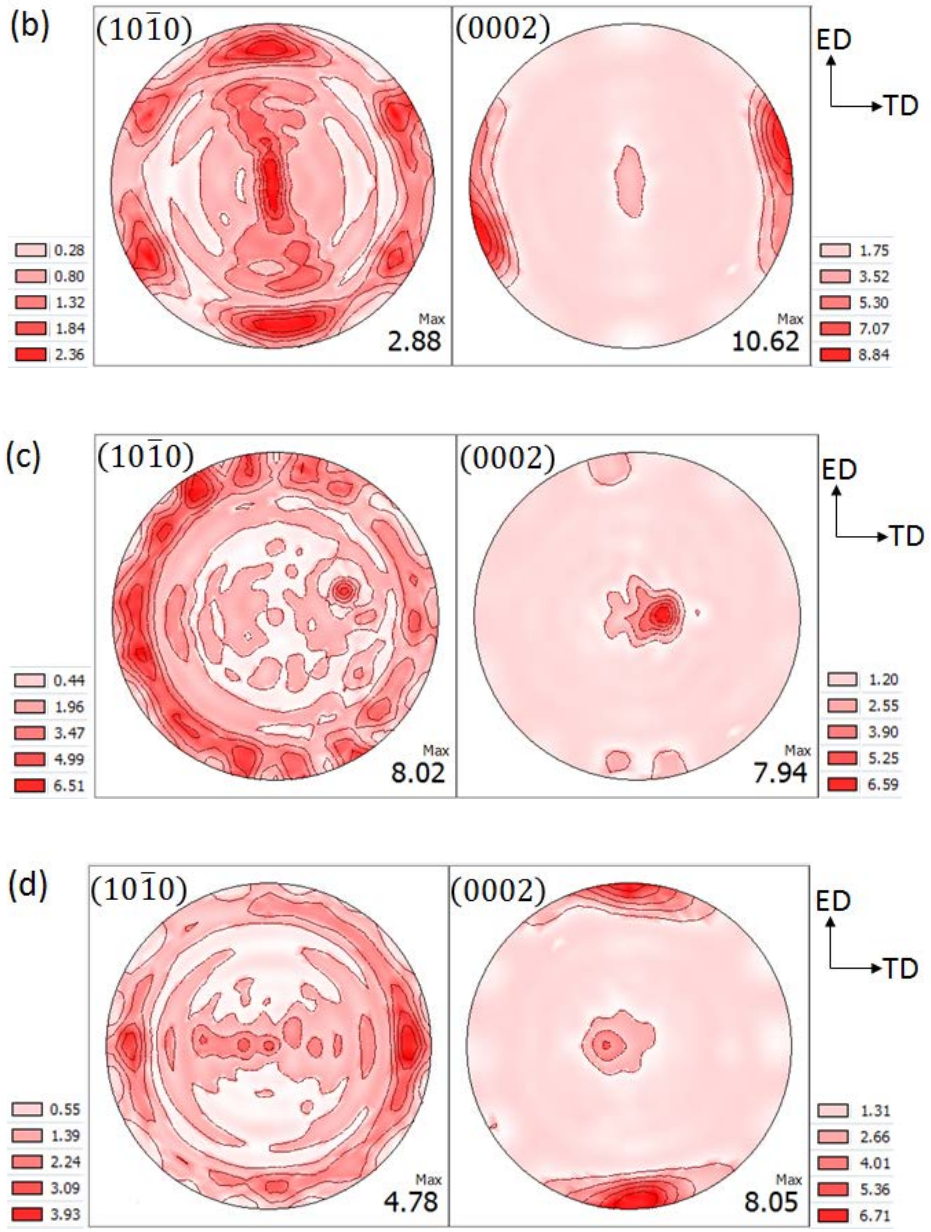

Figure 3.13 (0002) and (10$\bar{1}$0) pole figures of AM30 extrusion specimens subjected to cyclic tests at: (a) 0.3% in ED, (b) 2% in ED, (c) 0.3% in TD, and (d) 2% in TD.

3.3.4 Fracture surface characterisation

The typical SEM images of the fracture surface for ED specimen tested at low strain amplitude of 0.3% is shown in Figure 3.14. Two distinct regions of crack initiation/stable propagation (region I) and unstable crack propagation (region II) are demarcated by a line. These regions are identified with distinguishing features such as fatigue striations (Figure 3.14(c)) and river pattern for regions I and II, respectively [121]. Although a number of researchers [22,108,122] attributed the fatigue striations in magnesium alloys to sequential twinning/de-twinning processes, the observed striations in Figure 3.14(c) are probably due to slipping, bearing in mind the predominance of slip at low strain amplitudes. On closer observation of region I, multiple cracks are spotted emanating from the free surface. A magnified view of one of these crack initiation sites is depicted in Figure 3.14(b). It is clearly seen that the crack is originated at an extrusion-intrusion location at the surface (crack is designated with an arrow). These extrusion-intrusion features are results of persistent slip band (PSB) formation during slip-controlled cyclic process. The PSBs, are, in turn, formed due to irreversible dislocation glide, i.e., when individual glide process is not perfectly reversed upon strain reversal [123,124]. Furthermore, the wavy appearance of slip lines is characteristic of the cross-slip of <a>-type dislocations into non-basal slip planes [125]. These findings are in agreement with macroscopic flow curves presented earlier, as well as crack initiation mechanisms reported for various magnesium alloys in the literature [126–130].

In addition to slip-band cracking, other crack initiation mechanisms are also observed for magnesium alloys, namely, twin-boundary cracking and inclusion cracking. For the

magnesium alloy under investigation, cracks are evidenced to initiate at the twin lamellae interfaces at higher strain amplitudes. For instance, typical twin-boundary cracks (pointed by arrows in Figure 3.15) are captured by SEM near the surface of the specimen tested at 1.5% along ED. At such high strain amplitudes no notable crack initiation site was observed, or rather simultaneous cracking sites at different locations were pinpointed [4,94,130,131]. Inclusions (intermetallic particles) are found to be the common crack initiators for AM30 magnesium alloy under various loading conditions along different directions. These inclusions were analyzed to be Al-Mn binary phases [99,132,133]. A crack can be induced by a fractured inclusion, or by debonding at inclusion-matrix interface. Only the cracked intermetallic particles in AM30 alloy were witnessed in previous works [99,132]. Nonetheless, an indication of a crack generated at debonded inclusion-matrix interface for TD specimen tested at 0.3% is shown in Figure 3.16. An arrow points to the crack in the zoomed view of the inclusion-matrix interface.

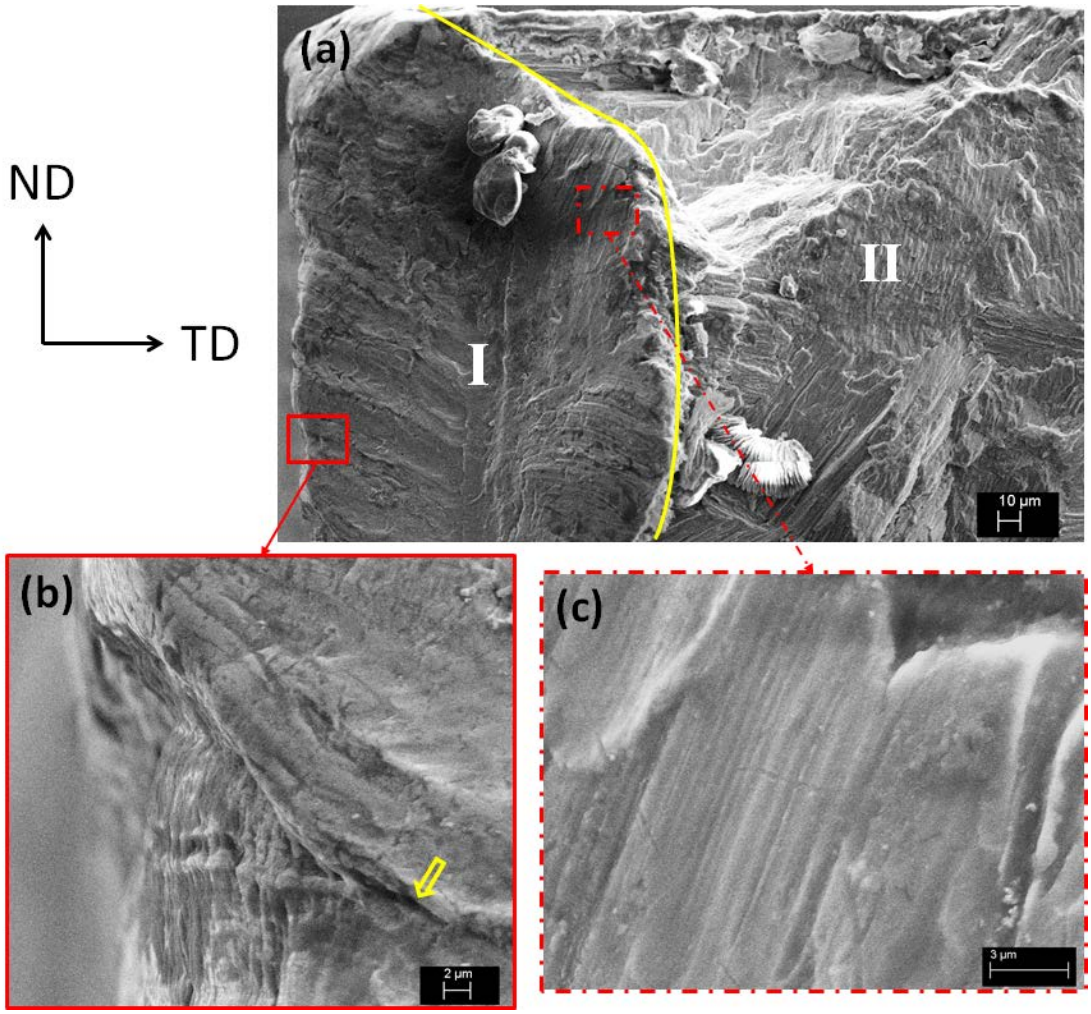

Figure 3.14 (a) SEM micrograph of AM30 typical fatigue fracture surface at low strain amplitude (0.3% in ED) showing regions I and II of crack propagation, as well as higher magnifications of (b) crack initiation site at surface with arrow pointing at the crack, and (c) fatigue striations corresponding to region I.

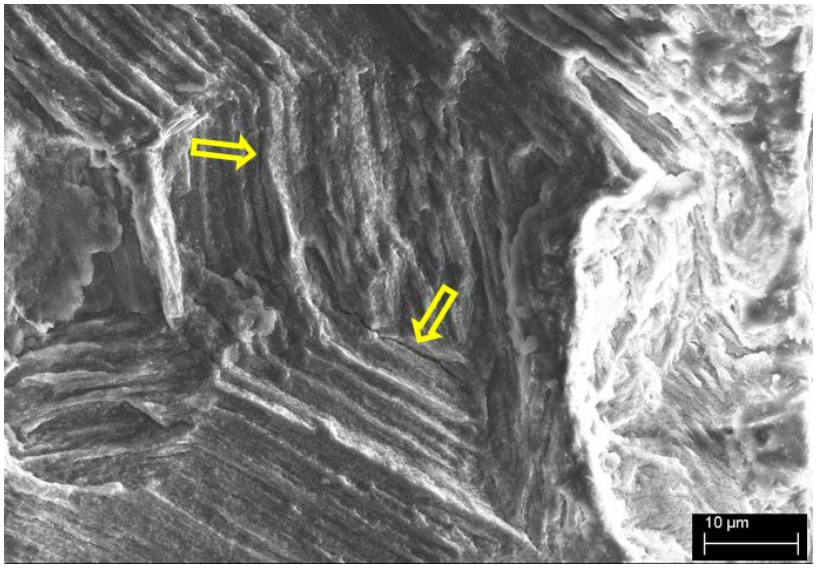

Figure 3.15 Twin lamellae as sources of fatigue cracks in AM30 at high strain amplitudes.

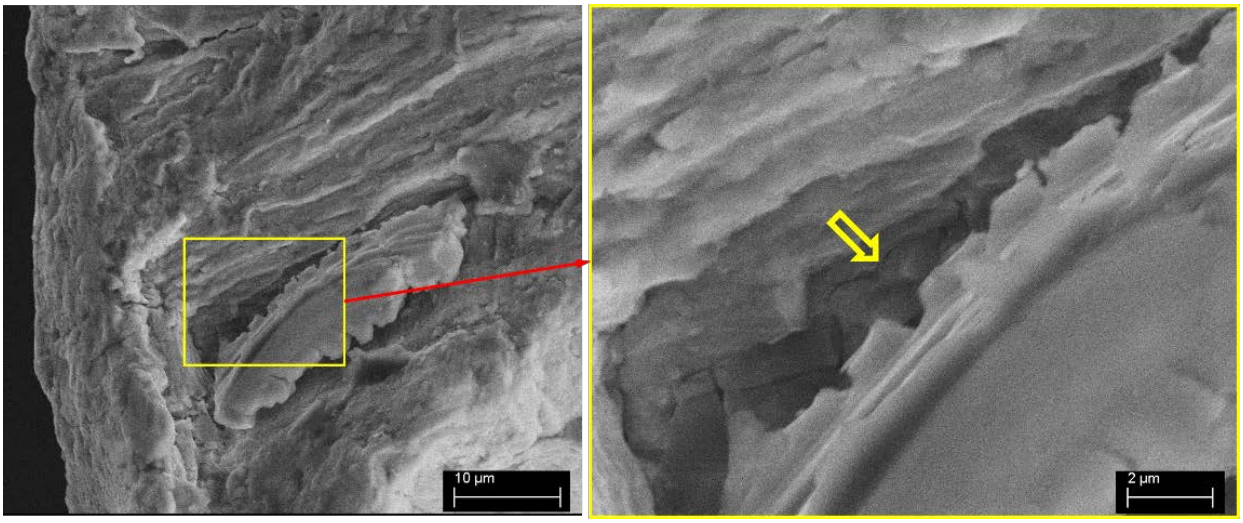

Figure 3.16 Typical SEM image of a fatigue crack originated from delaminated inclusion-matrix interface in TD specimen tested at 0.3%.

3.3.5 Strain-life curve

Total strain amplitude as a function of number of cycles to failure for specimens tested along ED and TD are presented in Figure 3.17(a). The tests in ED and TD are also summarized in Table 3.2 and Table 3.3, respectively (where ε_a: Axial strain amplitude; $^{\Delta\sigma}/_{2}$: Axial stress amplitude; σ_m: Mean axial stress; N_f: Fatigue life.). According to the results, ED specimens exhibit inferior fatigue properties compared to TD specimens over almost entire strain range tested in this investigation. The lower fatigue resistance demonstrated upon straining along ED may be explained by higher fatigue damage induced by means of more extensive twinning, as was deduced from flow characteristics in ED and TD. Mean stress effects should be also taken into account, which will be done so further on. The strain-life results are consistent with the previous studies on the direction-dependent fatigue behaviour of rolled AZ31 magnesium alloy [92,93].

For comparison purposes, strain-life results for AM30 extrusion tested in ED and ND at strain amplitudes up to 0.6%, taken from literature, are plotted in Figure 3.17(b), together with data from present study. It should be noted here that 0.6% is the maximum strain amplitude reported for cyclic testing of AM30 extrusion, hence, data up to 0.6% from present investigation are shown in Figure 3.17(b). The ED results are seen to be scattered, especially at strain amplitude of 0.3%. It is also noticed that ND demonstrates different fatigue properties at and below 0.5%. Their relatively lower fatigue life below 0.5% may be correlated with the fact that ND specimens are most favourably oriented for triggering extension twins during first tensile reversal [91,99]. At strain amplitude of 0.5%, however, the twins are found to be nucleating

along all directions. Under this circumstance, ED specimens, with highest developed mean stress, show less number of cycles before failure.

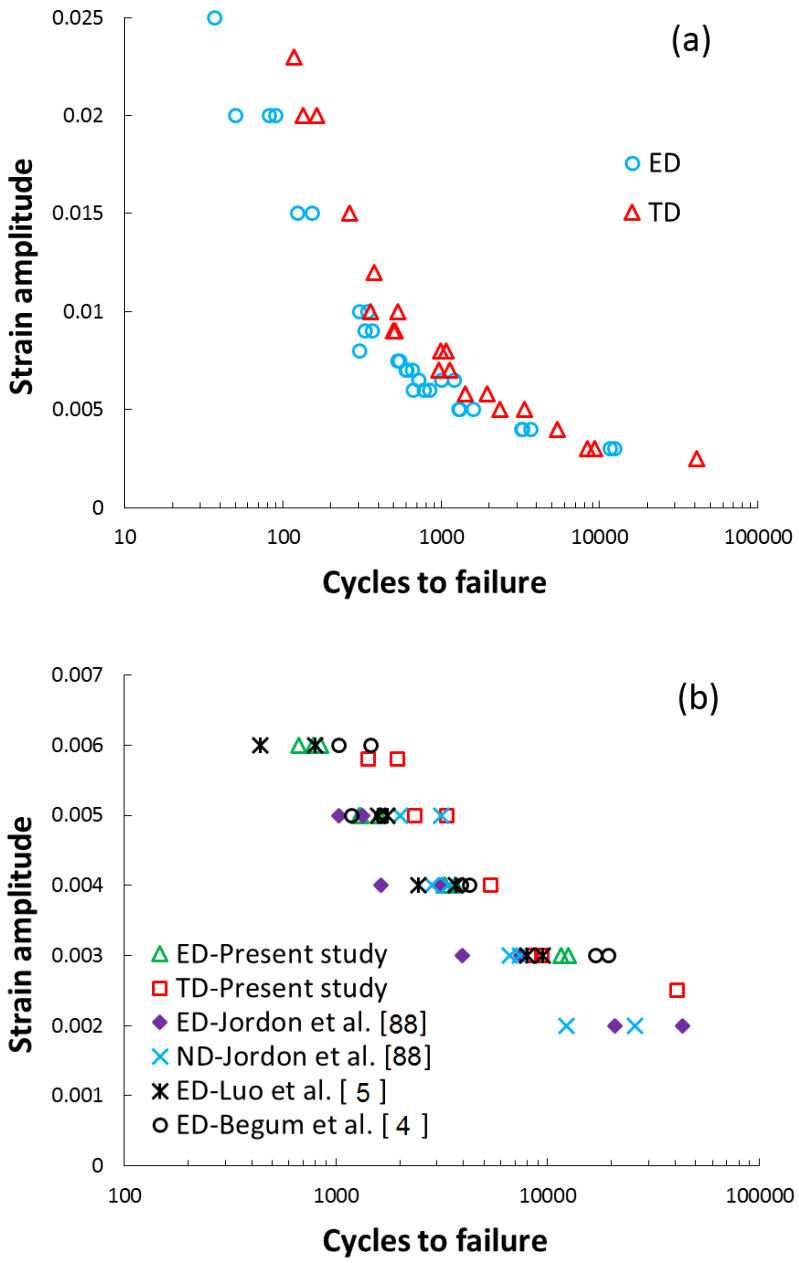

Figure 3.17 Strain-life data for AM30 extrusion along different directions: (a) obtained in the present study; (b) a comparison with results reported in literature.

Table 3.2 Cyclic axial ED test summary.

Spec. ID	ε_a (%)	$\Delta\sigma/2$ (MPa)	σ_m (MPa)	N_f (cycles)
ED06	0.3	130.3	26.6	12,532
ED22	0.3	132.8	31.1	11,589
ED07	0.4	166.6	48.6	3,231
ED58	0.4	163.1	48.5	3,658
ED26	0.5	190.6	66.9	1,312
ED56	0.5	196.9	72.4	1,592
ED30	0.6	206.9	75.6	845
ED57	0.6	204.4	71.5	780
ED14	0.7	203.9	66.8	606
ED25	0.7	201.5	65.1	659
ED49	0.75	200.5	60.0	531
ED24	0.9	201.4	50.6	366
ED54	0.9	202.9	52.2	331
ED28	1.0	200.4	48.6	341
ED55	1.0	201.1	45.3	305
ED21	1.5	208.9	29.6	152
ED48	1.5	211.7	23.6	124
ED29	2.0	220.3	16.5	90

Table 3.3 Cyclic axial TD test summary.

Spec. ID	ε_a (%)	$\Delta\sigma/2$ (MPa)	σ_m (MPa)	N_f (cycles)
TD02	0.3	112.4	10.4	8,407
TD05	0.3	109.6	15.7	9,357
TD18	0.4	128.0	20.0	5,377
TD19	0.5	147.5	24.3	2,349
TD28	0.58	150.2	32.1	1,414
TD33	0.58	145.4	25.9	1,958
TD07	0.7	158.0	34.4	1,125
TD32	0.7	153.3	32.1	966
TD09	0.8	160.4	32.3	992
TD36	0.9	160.1	29.7	509
TD11	1.0	160.5	28.6	358
TD37	1.0	162.6	27.4	528
TD29	1.2	166.1	25.0	377
TD15	1.5	174.2	20.3	264
TD16	2.0	187.5	15.6	134
TD24	2.0	188.9	11.4	163
TD27	2.3	190	9.5	117

3.4 Discussion

3.4.1 Cyclic stress-strain amplitude curves

In order to better understand the role of material anisotropy on the cyclic deformation behaviour of AM30 extrusion along two orthogonal directions, three undermentioned curves are extracted from half-life hysteresis loops and plotted against corresponding strain amplitude. Firstly, the plot of stress amplitude versus plastic strain amplitude for two directions is depicted in Figure 3.18(a). It is obvious that, to reach to the same amount of plastic deformation, higher levels of stress are needed when deforming along ED rather than TD. This is in tune with the more asymmetric hysteresis loops observed in ED (Figure 3.9), which can be related to higher volume fraction of twins activated during compressive reversal [16].

It is also to be noted that stress amplitude variation in TD exhibits an ascending trend, whereas in ED it shows minimal change after the strain corresponding to the activation of twinning. The reason lies probably in the way peak stress at the tip of tensile reversal in ED evolves, as is illustrated in Figure 3.18(b). This descending trend (softening) for the stress at tensile tip has been also reported for pure polycrystalline magnesium and ZK60 alloy extrusion strained along ED, and was attributed to the ceaseless occurrence of grain boundary and twin tip cracking with the start of deformation [109,134]. From this perspective, the lesser extent of twinning while deforming along TD can explain the observed trend for the stress at the tensile tip of TD hysteresis loops with increasing strain amplitude.

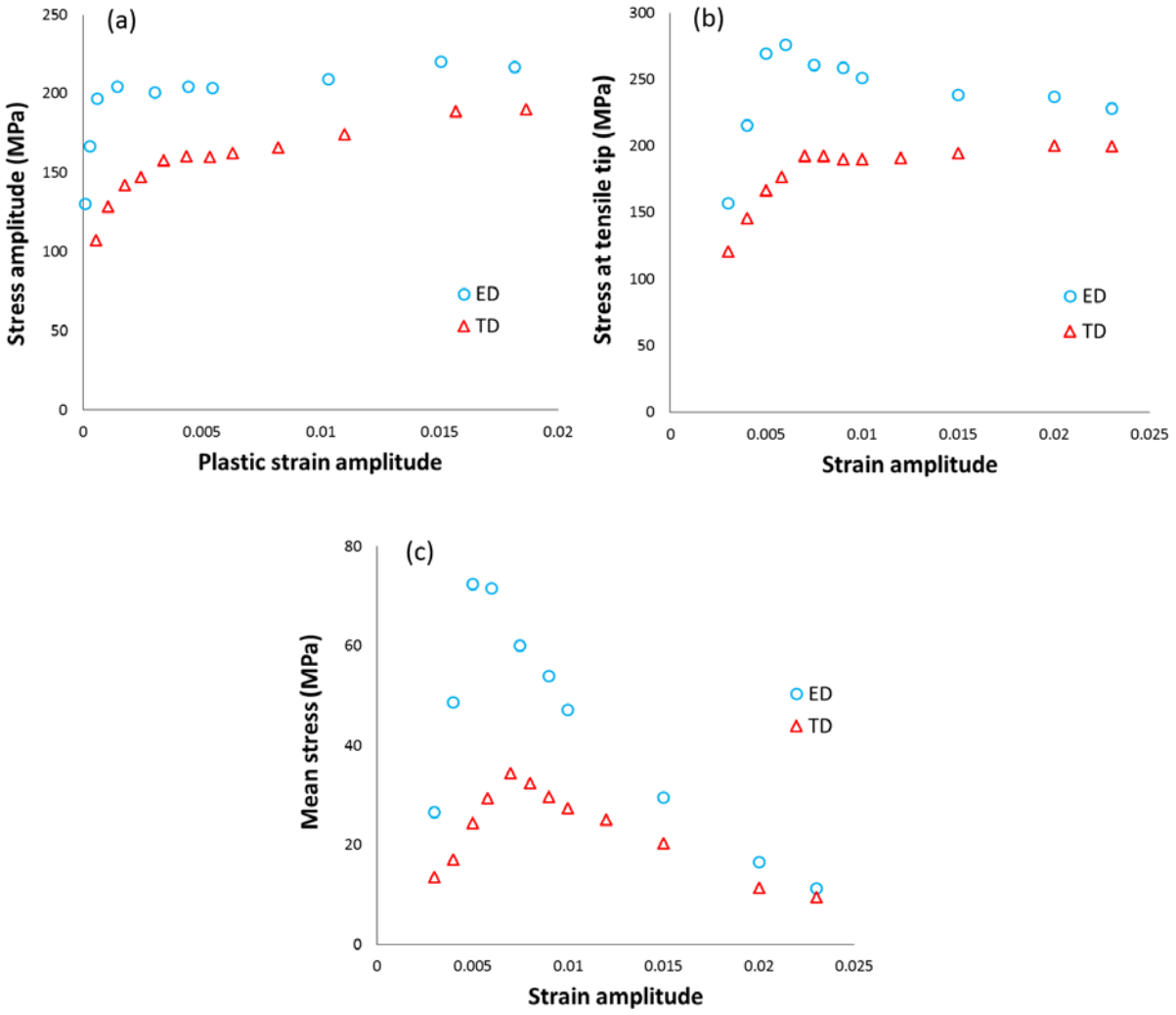

Figure 3.18 (a) Cyclic stress-plastic strain amplitude; variations of (b) stress at tensile tip and (c) mean stress with strain amplitude. Data extracted from half-life hysteresis loops in ED and TD.

3.4.2 Fatigue life modelling

In order to quantify the damage occurred in the microstructure of a material during cyclic loading, a number of fatigue damage parameters have been proposed and formulated in such a way that incorporates experimental fatigue life [29,135,58]. Available fatigue damage

parameters can be categorized into stress-, strain- and energy-based methods. As was seen in Figure 3.18, for AM30 extrusion, a larger applied strain amplitude does not necessarily produce higher peak stress or mean stress, while, it definitely ends in less number of cycles before failure. Hence, a stress-based fatigue damage parameter cannot properly describe the inflicted fatigue damage in the Mg alloy under this investigation. However, stress-based fatigue life prediction models have been employed by Lin et al. [136] for AZ31B Mg alloy under stress-controlled loading. In what follows, a strain-based and an energy-based fatigue damage criteria are being evaluated based on their capabilities to predict the anisotropic fatigue data of AM30 extrusion.

3.4.2.1 Smith-Watson-Topper (SWT)

The SWT parameter, initially formulated for mean stress effect consideration, has been employed by many researchers for multiaxial fatigue analyses as a strain-based critical plane approach [137,138]. This parameter is written in terms of fatigue life:

$$\sigma_{n,max}\frac{\Delta\varepsilon_1}{2} = \frac{\sigma_f'^2}{E}\left(2N_f\right)^{2b} + \sigma_f'\varepsilon_f'\left(2N_f\right)^{b+c} \qquad \textbf{(3.1)}$$

where ${\Delta\varepsilon_1}/{2}$ is the principal normal strain range, $\sigma_{n,max}$ is the maximum normal stress on maximum normal strain plane (as the critical plane) and E is the modulus of elasticity which was calculated, from the tensile tests, to be 43.8 GPa. The Coffin-Manson coefficients and exponents on the right-hand side of Equation (3.1) are extracted from Figure 3.19(a) and listed in Table 3.4. The symbols in Figure 3.19(a) corresponds to the experimental data obtained from half-life hysteresis loops along TD and the dashed lines represent the best power-law fits.

Table 3.4 Coffin-Manson parameters for SWT model.

Fatigue strength coefficient, σ_f' (MPa)	410.416
Fatigue toughness coefficient, ε_f'	1.480
Fatigue strength exponent, b	-0.130
Fatigue toughness exponent, c	-0.791

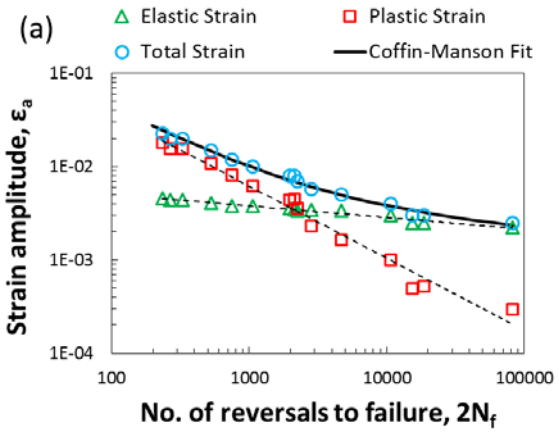

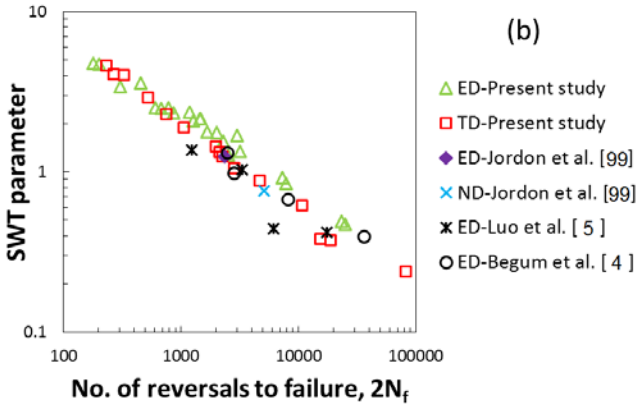

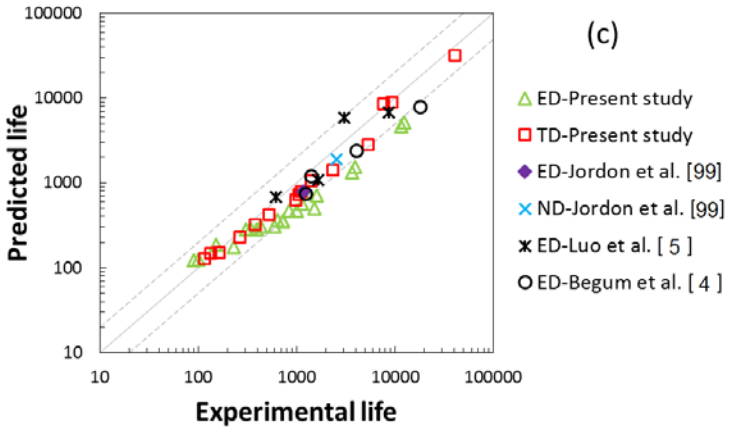

Figure 3.19 (a) Strain-life data used for extracting Coffin-Manson constants; (b) SWT damage parameter evolution with number of reversals to failure; (c) The correlation of SWT-estimated fatigue life with experimental life.

Figure 3.19(b) shows the SWT parameter calculated for each cyclic test condition as a function of number of reversals to failure. The data from literature are also included. From this plot, the relationship between SWT parameter and fatigue life in terms of reversal count can be fairly expressed using a single power-law relation. This implies that the SWT parameter can be utilized to quantify the fatigue damage imposed upon straining in different directions.

The predicted fatigue life, calculated from Equation (3.1) in conjunction with values from Table 3.4, is plotted against the experimental life in Figure 3.19(c). The diagonal solid line denotes the perfect match and the other two dashed lines stand for factor of 2 bounds between predicted and experimental life. The life estimations are mostly found to be within a life factor range of 2, though for a few tests (mostly in ED) the lives are under-predicted. There is also some scatter seen in, especially, the ED predictions. These observations can be ascribed to the

maximum normal stress parameter in SWT equation, Equation (3.1), as its evolution with increasing strain amplitude was seen to be unusually complex (Figure 3.18(b)).

3.4.2.2 Jahed-Varvani (JV)

Energy-based fatigue damage model is another commonly used approach, especially for anisotropic materials. This is because of the invariant nature of strain energy density, being a scalar quantity. In this study, Jahed-Varvani energy model, which was introduced in 2006 [139], will be employed for fatigue life estimation. In the JV model, total energy density as damage parameter is assumed to consist of positive elastic and plastic parts. The latter is defined as the area inside the hysteresis loop at each strain amplitude (cyclic energy) and the former can be calculated from following equation:

$$\Delta E_e^+ = \frac{{\sigma_{max}}^2}{2E} \tag{3.2}$$

where σ_{max} is the stress at the tensile tip of the hysteresis loop. Through the addition of positive elastic strain energy density, mean stress effect is also taken into account in this model [140]. The energy damage parameter is, then, correlated with fatigue life via an equation analogous to the Coffin-Manson relation [139]:

$$\Delta E = E_e'\left(2N_f\right)^B + E_f'\left(2N_f\right)^C \tag{3.3}$$

where ΔE is the total strain energy density. Coefficients and exponents in Equation (3.3) are extracted from energy-life curves (Figure 3.20(a)) and are tabulated in Table 3.5. The same set of tests as the one used in Figure 3.19(a) is utilized for parameter extraction in Figure 3.20(a).

Table 3.5 Energy-based parameters for JV model.

Fatigue strength coefficient, E'_e (MJ/m^3)	2.995
Fatigue toughness coefficient, E'_f (MJ/m^3)	1710.690
Fatigue strength exponent, B	-0.281
Fatigue toughness exponent, C	-0.975

The plot of total strain energy density versus number of reversals to failure is depicted in Figure 3.20(b), including the data from literature. As is seen, all the data points can be consolidated into one single curve. This validates the use of strain energy density for evaluating fatigue damage occurred in AM30 extrusion along different directions, i.e., ED, TD and ND.

The correlation between predicted life and experimental life in both directions is illustrated in Figure 3.20(c). All data points fall within the bounds signifying life factor of ±2 (dashed lines). Most of the fatigue life predictions are closely consistent with the observed fatigue life (the data points located on the solid diagonal line). In contrast with the SWT results, the life predictions of the JV model in ED are not scattered, though the maximum stress is included in this model too. The accuracy of the JV energy model has been also reported to be good in multiaxial fatigue life prediction of AZ31B extrusion [86,135].

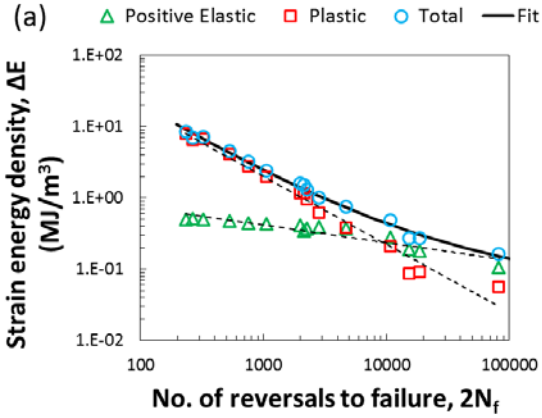

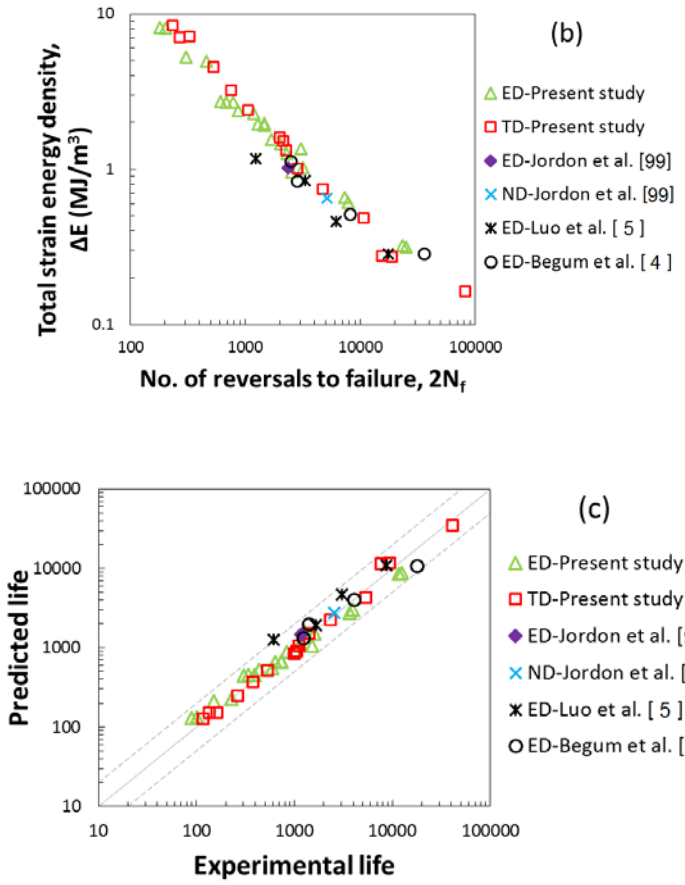

Figure 3.20 (a) Strain energy-life data used for extracting constants in Equation (3.3); (b) JV damage parameter evolution with number of reversals to failure; (c) The correlation of JV-estimated fatigue life with experimental life.

3.5 Conclusions

The uniaxial tension-compression fatigue experiments controlled under fully-reversed condition at various strain amplitudes ranging from 0.3% to 2.3% have been conducted on AM30 Mg alloy extrusion along extrusion (ED) and transverse (TD) directions. Based on the presented results in this chapter, the following main conclusions can be drawn:

1) The shapes of hysteresis loops in ED and TD are governed by different mechanisms controlling deformation. In both directions, deformation at half-life is dominated by slip when strain amplitude is below 0.5%. Afterwards, twinning/de-twinning becomes predominant deformation mechanism, which is accompanied by asymmetric cyclic response.
2) Extension twinning is believed to happen to a larger extent during compressive reversal along ED compared to TD. This results in higher asymmetry of hysteresis loops in ED.
3) While cyclic hardening is observed along both directions, the stress amplitude and mean stress developed through cyclic loading in ED are higher than those in TD.
4) AM30 extrusion exhibits better fatigue properties when deformed under cyclic loading along TD compared to that in ED, over almost entire strain range tested here. This has been related to the higher fatigue damage induced by means of more extensive twinning as well as higher detrimental mean stress in ED.
5) Fatigue cracks are evidenced to initiate at the specimens' surfaces. Persistent slip bands (PSBs) and twin lamellae interfaces are observed sites of cracking in specimens tested at low and high strain amplitudes, respectively. Cracking/debonding of intermetallic particles is realized as the common crack initiator in AM30 extrusion under various loading conditions.
6) Jahed-Varvani (JV) energy model gives superior life estimations for AM30 Mg alloy extrusion subjected to cyclic loading, irrespective of loading direction.

Chapter 4

Multiaxial cyclic behaviour and fatigue modelling of AM30 Mg alloy extrusion

4.1 Introduction

Saving energy and conservation of environment are two major reasons for drawing automotive industries' attention to wrought magnesium alloys as a light structural metal [2,9]. It was stated that diminishing the vehicle's weight by 10% would bring about a saving of approximately 5% in fuel consumption, assuming the appropriate adjustment of engine and gearbox performance [1].

Magnesium alloys are, currently, being utilized for making non-load bearing components, e.g., housing and trim parts [1,6]. To exploit their full weight-saving potential, their application needs to be broadened to load bearing components, such as body and suspension parts. Under vehicle's normal service conditions, these parts, are subjected to cyclic loading in multiaxial stress state, and thereby, prone to fatigue failure. Although the load bearing parts are generally designed to operate under low cyclic stresses in high cycle fatigue regime, they may locally experience high cyclic stresses at notches and other geometrical complexities. In light of what has been said above, understanding the multiaxial fatigue response of magnesium alloys is imperative to ensure the reliability and safety of vehicles throughout their service life.

Twenty years ago, Bentachfine et al. [141] performed strain-controlled axial-torsional tests on a magnesium-lithium alloy extrusion at various phase angle shifts in the range of 0 to 180°. They concluded that increasing phase angle shift from 0 to 90° decreases fatigue life, which was related to the generation of more complex defect structure and higher dislocation density as results of constant rotation of principal strain axes with respect to grain orientation. Since that time, there were only a few studies dealing with the multiaxial deformation and fatigue of wrought magnesium alloys. Yu et al. [142] conducted fully-reversed strain-controlled pure axial, pure torsional and combined axial-torsional cyclic tests on AZ61A extrusion. Employing an equivalent strain amplitude parameter defined as the radius of a circle circumscribing loading path, they reported the highest resistance to fatigue failure under proportional loading and the shortest fatigue life under 90° out-of-phase loading. It was, further, shown that Fatemi-Socie (FS) and modified Smith-Watson-Topper (SWT) models were able to acceptably predict experimental fatigue life. In another study by the same authors (Zhang et al. [107]), cyclic deformation characteristics of AZ61A extrusion were explored. Slight cyclic hardening and insignificant non-proportional hardening were observed under various loading conditions. The asymmetry of shear hysteresis loop in combined axial-torsional tests was attributed to the successive occurrence of twinning/de-twinning under axial deformation mode. Similar to the work by Yu et al. [142], Xiong et al. [106] investigated AZ31B extrusion and reached to the same conclusion regarding fatigue resistance under different loading conditions. Moreover, they evaluated the modified SWT and Jiang critical plane models capable of predicting fatigue life under multiaxial loading conditions. Albinmousa et al. [26,29,86,135]

carried out fully-reversed strain-controlled cyclic tests, including pure axial, pure torsional, and combined axial-torsional proportional and non-proportional at 45 and 90° phase angle shifts, on AZ31B extrusion. Their results demonstrated that AZ31B extrusion exhibited additional hardening because of non-proportionality, but not due to multiaxiality. Notwithstanding this non-proportional hardening, it was reported that phase angle shift had no significant influence on obtained fatigue life. In regard to fatigue modelling done by Albinmousa et al., Fatemi-Socie and Jahed-Varvani models resulted in better fatigue life estimations. Recently, Castro and Jiang [143] examined three critical plane approaches, i.e., SWT, FS and Jiang, using various uniaxial and multiaxial cyclic tests on AZ31B extrusion. It was deduced that FS and Jiang models gave reasonable fatigue life predictions and only Jiang model made a good correlation of cracking direction, which was ascribed to the mixed cracking mode of AZ31B extrusion. More recently, Li et al. [144] studied the multiaxial cyclic response of AZ31 extrusion during strain and stress-controlled experiments. From strain-controlled tests, they observed cyclic hardening in both axial and torsional directions, as well as additional hardening due to multiaxiality in torsional mode. They also concluded that axial ratcheting during multiaxial stress-controlled tests depended on the shape of loading path in addition to the non-proportionality of loading. Circular 90° out-of-phase loading path generated the largest axial ratcheting strain.

The literature reviewed above were all on the multiaxial study of AZ family of wrought magnesium alloys, especially AZ31B extrusion. To the best of authors' knowledge, no comprehensive study has thus far been done on the multiaxial behaviour of AM family of wrought Mg alloys, specifically AM30 extrusion. This chapter is, therefore, aimed at providing

such study. Besides, in order to complement the uniaxial experimental cyclic data on AM30 extrusion presented in previous chapter, extensive pure torsional experiments have been conducted. The capabilities of two strain-based models, i.e., Fatemi-Socie and modified Smith-Watson-Topper, and an energy-based model, i.e., Jahed-Varvani, to predict fatigue life under general loading conditions are also investigated.

4.2 Material and methods

Experimental material for the present study was hot-extruded AM30 magnesium alloy developed by Luo and Sachdev [3]. The details of the experimental alloy including its chemical composition and hot extrusion process parameters can be found in [101]. Thin-walled tubular specimens were machined from extrusion section along extrusion direction with the geometry and dimensions shown in Figure 4.1. It is worth noting that in order to make sure of microstructural uniformity, center region of the extrusion section (away from surface) were used for machining the specimens [4]. Figure 4.2 schematically shows the extrusion section and the location where the tubular specimens were cut from. The orientation of HCP crystals in connection with defined section directions, i.e., extrusion (ED), transverse (TD) and normal (ND), is also depicted in Figure 4.2.

Fatigue experiments were conducted using an Instron 8874 servo-hydraulic biaxial machine with axial and torsional load capacities of ±25 *kN* and 100 *N.m*, respectively. All of the experiments were done under fully-reversed ($R_{\varepsilon\, or\, \gamma} = -1$) strain-controlled condition at ambient temperature. Axial tension-compression cyclic data along ED were taken from previous publication [7]. Epsilon biaxial extensometer (model 3550) with the axial and shear strain

ranges of ±5% and ±3°, mounted on specimen's gauge length, was employed to record engineering axial and shear strains. Sinusoidal waveforms with different phase angle shifts of 0, 45 and 90° were applied for proportional and non-proportional axial-torsional tests. Pure torsional tests were run at frequencies ranging from 0.03 to 0.4 *Hz*, depending on applied shear strain amplitude. At very low shear strain amplitudes, after material stabilized, tests were stopped to remove the extensometer. The tests were, then, resumed running at higher frequencies up to 8 *Hz* under torque-controlled condition. Axial-torsional tests were done at lower frequencies between 0.1 and 0.3 *Hz*. Failure criteria were assumed to be either final rupture of the specimen or 50% drop in maximum load, whichever came first, unless stated otherwise. The stress-strain curve at half-life was identified as stabilized stress-strain response.

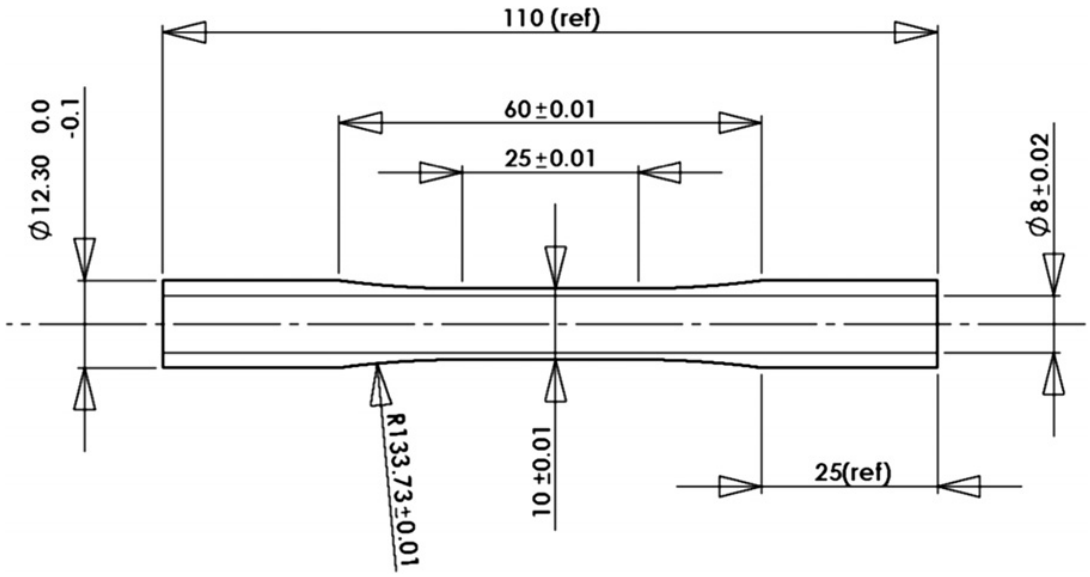

Figure 4.1 Tubular specimen geometry for pure torsional and biaxial tests.

Texture measurements were performed via a Bruker D8 Discover X-ray diffractometer equipped with a VÅNTEC-500 2D detector using Cu-K_α beam radiation at 40 *kV* and 40 *mA*.

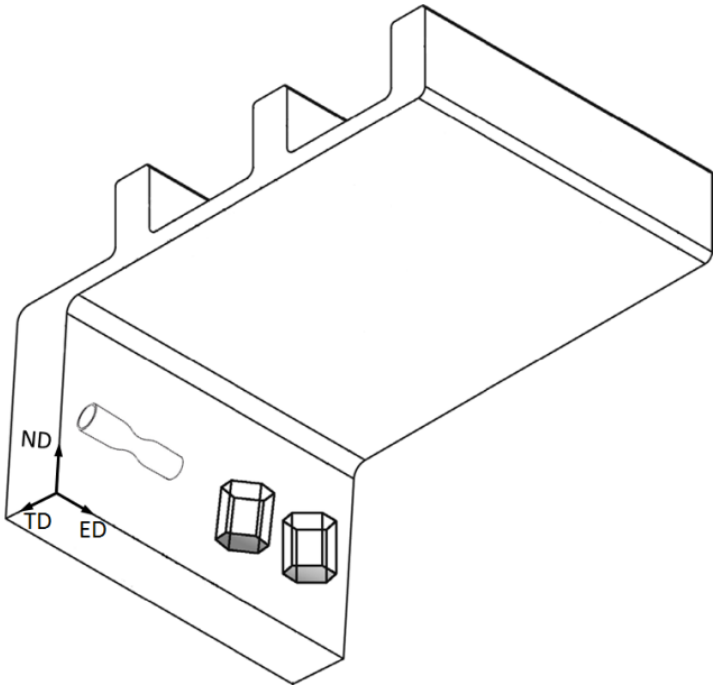

Figure 4.2 Schematic illustration of extrusion section showing crystal orientation in portion used for machining tubular specimens.

4.3 Results and discussion

4.3.1 Pure torsional cyclic loading

4.3.1.1 Hysteresis loops

Stabilized shear stress-shear strain hysteresis loops of AM30 extrusion subjected to pure torsional loading are illustrated in Figure 4.3. Eleven shear strain amplitudes in the range of 0.4% to 2.5% are employed to fully characterise the torsional behaviour of the experimental alloy. Unlike its axial cyclic behaviour, explored elsewhere [7], AM30 extrusion possesses normal symmetric hysteresis loops under torsion. This can more clearly be seen from Figure 4.4, where the maximum and minimum tips of hysteresis loops at various shear strain amplitudes

are plotted in one graph. From this figure, it can also be concluded that no significant mean stress is developed upon cyclic torsion testing. The observed symmetry alludes to the dominance of slip deformation mechanisms, although the occurrence of twinning was also reported at high shear strain amplitudes [22,106,107]. The slightly sigmoidal shape of hysteresis loop at shear strain amplitude of 2.5% (can also be seen from Figure 4.7(c)) is probably due to twinning, which is in consistence with twin observation by other researchers.

To contrast monotonic with cyclic shear flow, monotonic shear stress-shear strain curve of AM30 extrusion up to 3% shear strain is also included in Figure 4.4. It is seen that stresses from cyclic curve are higher than the ones from monotonic curve. Cyclic shear hardening coefficient, K_s', and exponent, n_s', are calculated to be 335.6 *MPa* and 0.3023, respectively, while monotonic shear hardening coefficient, K_s, and exponent, n_s, are 154.78 *MPa* and 0.2019. The results suggest that AM30 extrusion shows greater hardening capacity when subjected to cyclic shear deformation. Hardening disparity between cyclic and monotonic data grows with the shear strain to reach to roughly 25% increase in shear stress at the shear strain of 2.5%.

Texture measurements represented by basal (0002) and prismatic $(10\bar{1}0)$ pole figures can be used to verify twin occurrence at high shear strain amplitudes. Figure 4.5(a) shows pole figures of as-extruded material and Figure 4.5(b) shows pole figures of a specimen subjected to 2.5% cyclic shear strain amplitude. XRD measurements in Figure 4.5(b) were done on a section far away from final fatigue crack. According to Figure 4.5(a), the as-extruded material displays a rather strong basal texture with the majority of (0002) poles lying almost parallel to normal direction (ND), noting the peak intensity of 18.74 MUD (multiples of uniform distribution).

The reduction of peak intensity of basal poles to 9.96 MUD and emergence of new texture components in Figure 4.5(b) can only be justified by the formation of mechanical twins during pure torsional straining. However, mechanical twinning does not seem to have a noticeable effect on the symmetry of shear hysteresis loops (Figure 4.3 and Figure 4.7). This probably hints at the equal amount of twinning/de-twinning under positive and negative shear stresses, because of the rotational symmetry of basal poles about extrusion direction [107].

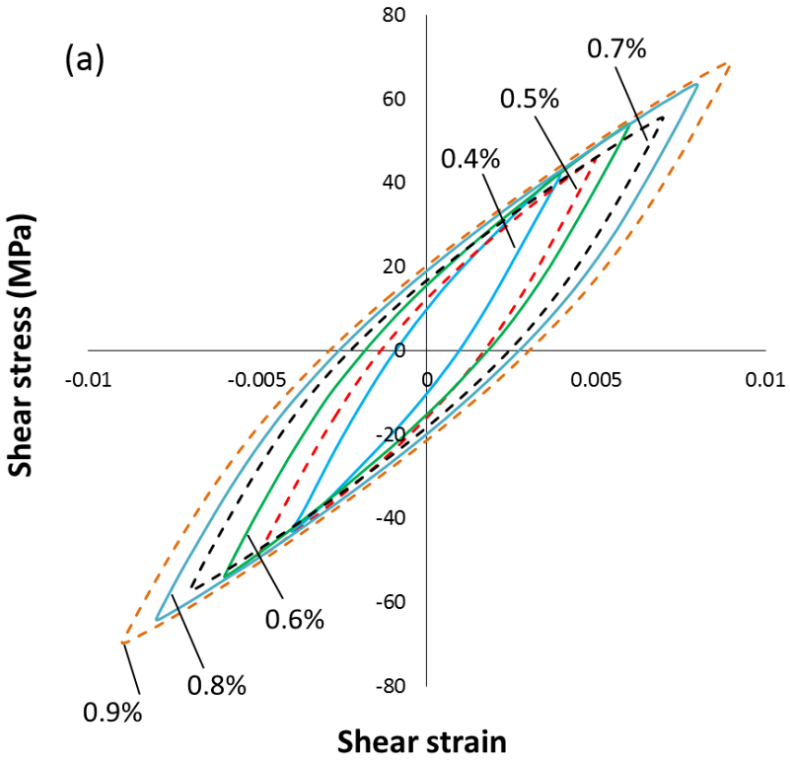

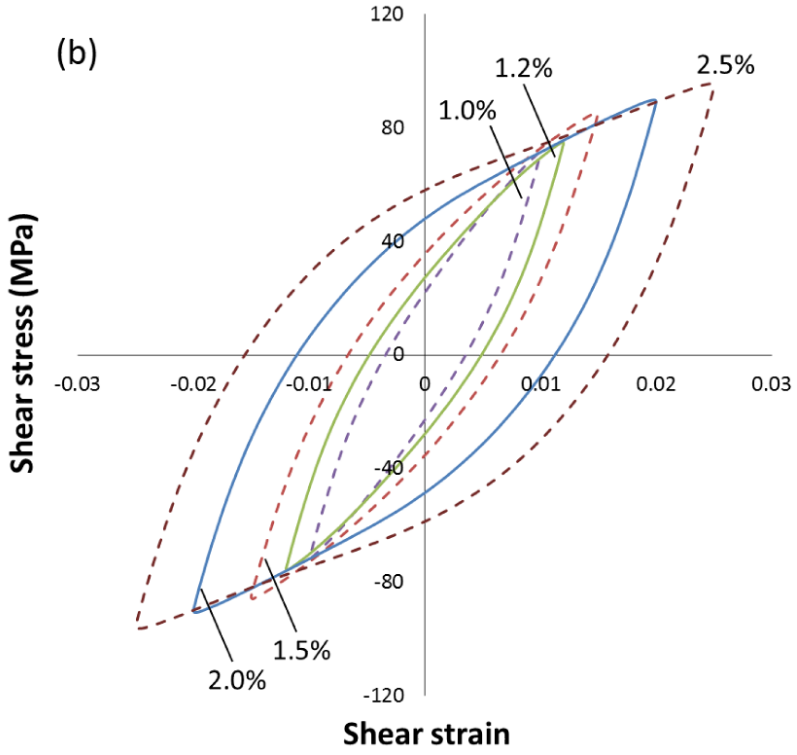

Figure 4.3 Half-life hysteresis loops of AM30 extrusion at different strain amplitudes under pure torsion.

The variations of shear stress amplitude with cycling at different shear strain amplitudes are depicted in Figure 4.6. As is seen, AM30 extrusion hardens during cyclic shear straining. However, the rate of hardening depends on the strain amplitude. Generally, the hardening rate increases with increasing shear strain amplitude. This increase in hardening rate is more pronounced for the shear strain amplitudes above 1%. This may be due to the occurrence of twinning at high shear strain amplitudes, which hinders free dislocation movements [107]. These results are in accordance with the cyclic shear behaviour reported for AZ61A extrusion [107]. Moreover, compared to AZ31B extrusion [26], the experimental alloy exhibits stronger cyclic shear hardening. The overall cyclic shear hardening response can also be inferred from

Figure 4.7, where second-cycle along with the half-life hysteresis loops at low, intermediate and high shear strain amplitudes are plotted.

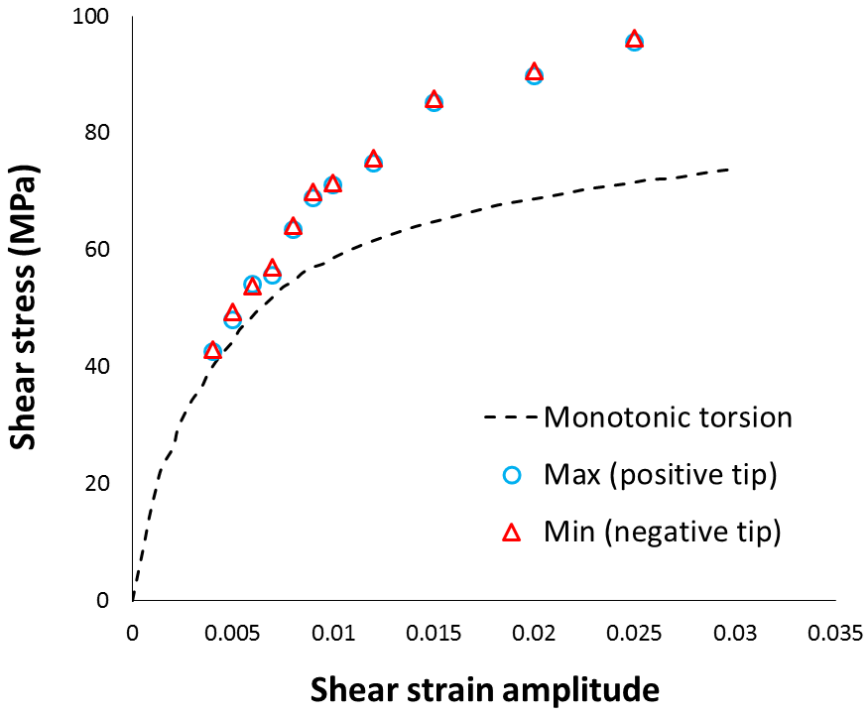

Figure 4.4 Cyclic and monotonic shear stress-shear strain curves of AM30 extrusion.

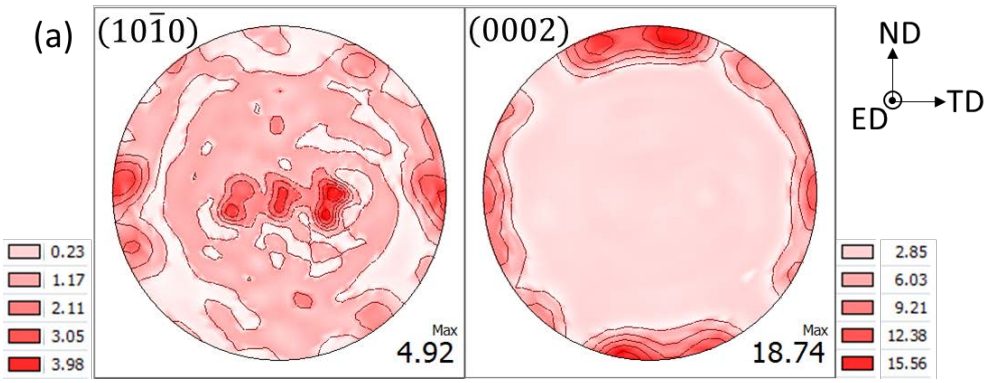

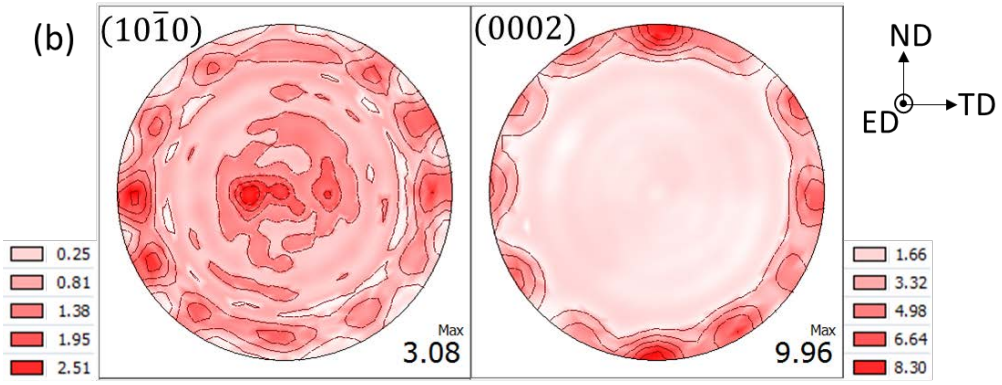

Figure 4.5 Basal and prismatic pole figures of (a) as-extruded material and (b) specimen tested under pure torsion at 2.5% shear strain amplitude.

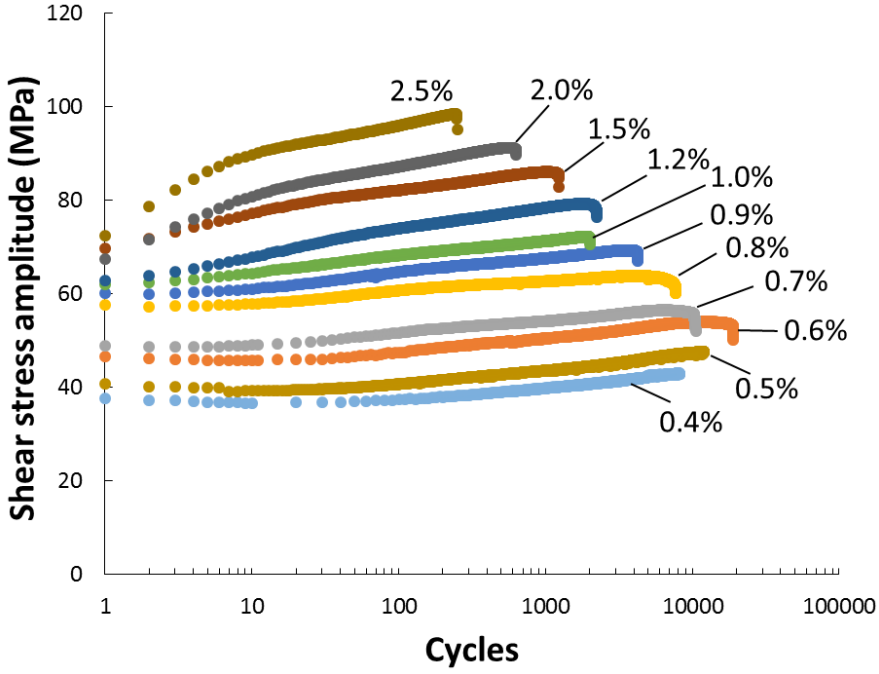

Figure 4.6 Shear stress amplitude evolution with cycling at various shear strain amplitudes.

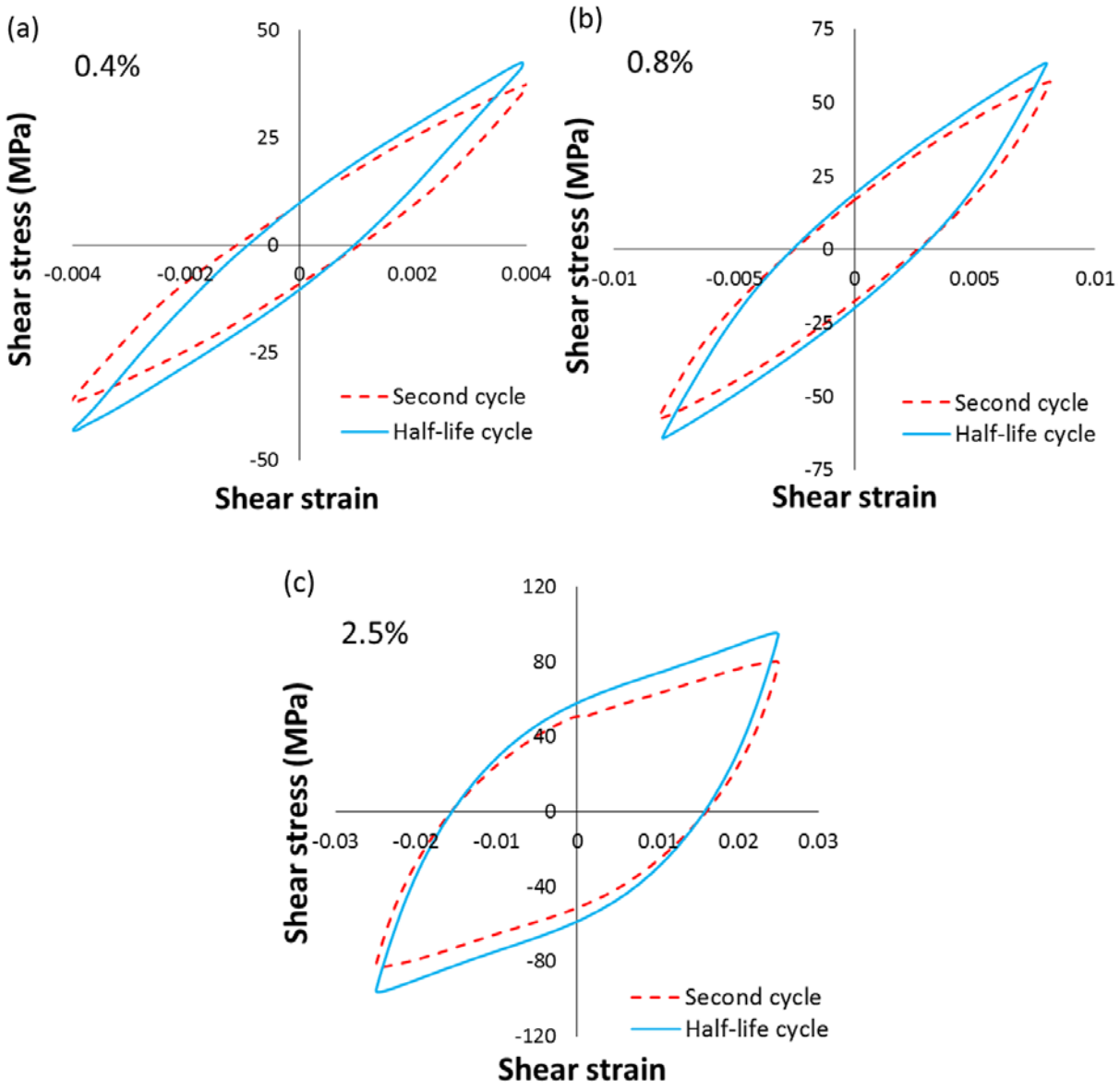

Figure 4.7 Typical shear hysteresis loops of AM30 extrusion at second and half-life cycles during cyclic tests at (a) low, (b) intermediate, and (c) high shear strain amplitudes.

4.3.1.2 Shear strain-life curve

Total shear strain amplitude as a function of number of cycles before fatigue failure for the experimental alloy under pure torsional loading is shown in Figure 4.8. For comparison purposes, shear strain-life data for AZ31B and AZ61A Mg alloy extrusions from literature [106,142] are also included. An arrow associated with a data point denotes a run-out test for which fatigue failure has not occurred at one million cycles. It should be mentioned here that the shear fatigue life data in Figure 4.8 are reported at 5% drop of maximum shear stress in a loading cycle, to be consistent with the fatigue life data from literature. It is, however, observed that, in most cases, final failure happens either quickly or after a few cycles upon initial load drop. The summary of cyclic pure torsional tests are also given in Table 4.1, reporting lives at 50% torque drop (where γ_a: Shear strain amplitude; $^{\Delta\tau}/_{2}$: Shear stress amplitude; τ_m: Mean shear stress; N_f: Fatigue life.).

According to results from strain-controlled cyclic experiments displayed in Figure 4.8, AM30 extrusion shows better low-cycle shear fatigue properties than AZ31B and AZ61A extrusions. Considering the fact that at large strains, enhanced fatigue life depends more on ductility [145], the observed behaviour can be connected with the better formability of AM30 extrusion [3,4]. High-cycle shear fatigue properties of these alloys may be better contrasted by conducting stress-controlled cyclic tests.

Table 4.1 Cyclic pure torsional test summary.

Spec. ID	γ_a (%)	$\Delta\tau/2$ (MPa)	τ_m (MPa)	N_f (cycles)
PT14	0.4	42.8	-0.2	58,258
PT27	0.4	45.9	-0.3	62,769
PT22	0.5	47.6	-1.8	40,586
PT01	0.6	53.3	0.5	18,356
PT05	0.6	54.0	0.1	19,653
PT03	0.7	56.4	-0.7	11,093
PT02	0.8	59.7	-1.0	5,813
PT32	0.8	63.9	-0.4	7,875
PT20	0.9	68.7	-0.1	4,343
PT29	1.0	65.6	-0.4	3,714
PT31	1.2	75.3	-0.4	2,409
PT09	1.5	85.5	-0.3	1,267
PT10	1.5	86.5	-0.6	1,468
PT15	2.0	93.0	-0.5	542
PT18	2.0	90.2	-0.5	644
PT19	2.5	95.9	-0.4	256

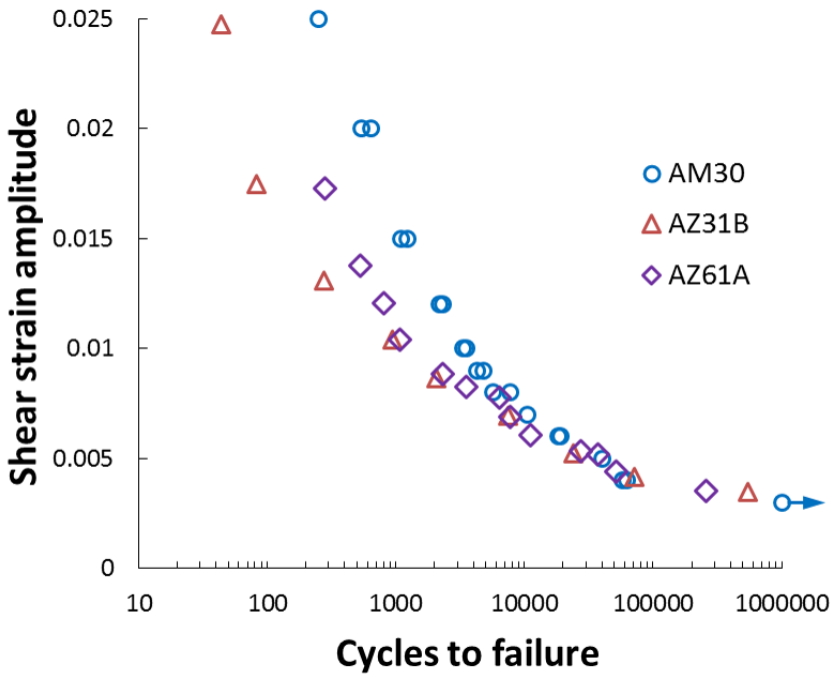

Figure 4.8 Shear strain-life data for AM30 extrusion compared with data for other wrought Mg alloys (AZ31B [106] **and AZ61A** [142]**).**

4.3.2 Combined axial-torsional cyclic loading

The details of the axial-torsional experiments including applied strain amplitudes, axial and shear stress ranges and mean values and experimental fatigue lives are tabulated in Table 4.2 (where ε_a: Axial strain amplitude; γ_a: Shear strain amplitude; $\Delta\sigma$: Axial stress range; σ_m: Mean axial stress; $\Delta\tau$: Shear stress range; τ_m: Mean shear stress; N_f: Fatigue life.). The stress ranges and mean values are extracted from half-life (stabilized) hysteresis loops under axial and torsional deformation modes. It is also to be noted that the middle number of specimen ID denotes phase angle difference between axial and torsional deformation modes. In following

sections, the axial-torsional cyclic behaviour of AM30 extrusion will be explored from two perspectives: the interrelation of deformations in two different axes, and the influence of phase angle shift between axial and torsional loading cycles on cyclic hardening, hysteresis loops as well as obtained fatigue lives.

4.3.2.1 Multiaxial deformation effects

The effect of simultaneous shear deformation on the shape of axial hysteresis loop and the evolution of axial stress amplitude during proportional (in-phase) axial-torsional tests are depicted in Figure 4.9. The proportional tests comprise axial strain amplitude of 0.5% and various shear strain amplitudes of 0, 0.4 and 0.6%.

A closer look at Figure 4.9(a) reveals that the accompanied shear strain does not affect twinning/de-twinning-dominated portions of the axial hysteresis loops, at the end of compressive reversal and the initial stage of tensile reversal. However, the hardening rate of slip-dominated portion that follows de-twinning saturation is decreased with increasing accompanied shear strain. In other words, slip happens with less resistance in the co-presence of larger shear strain. This may be explained by the fact that accompanied shear stress will contribute to resolved shear stress on a specific slip plane to reach to its critical value (CRSS), and thereby, accommodate axial strain under lower axial stress.

Table 4.2 Proportional and non-proportional axial-torsional fatigue tests' results.

Spec. ID	ε_a (%)	γ_a (%)	$\Delta\sigma$ (MPa)	σ_m (MPa)	$\Delta\tau$ (MPa)	τ_m (MPa)	N_f (cycles)
BA-0-3	0.3	0.4	235.7	11.8	79.3	1.4	8,911
BA-0-10	0.3	0.4	225.2	11.5	78.5	2.1	9,197
BA-0-2	0.4	0.4	310.9	46.1	72.9	6.2	1,520
BA-0-7	0.4	0.4	300.1	41.7	72.6	4.9	1,554
BA-0-4	0.5	0.4	355.2	55.6	68.3	6.7	1,157
BA-0-8	0.5	0.6	330.2	42.9	87.4	6.2	917
BA-0-11	0.4	0.6	276.7	37.2	97.7	6.7	1,629
BA-0-12	0.3	0.6	223.6	20.3	99.5	5.1	3,210
BA-0-5	0.4	0.3	294.8	31.4	58.0	4.6	4,027
BA-0-9	0.4	0.5	302.0	48.0	84.5	5.8	1,495
BA-45-1	0.3	0.4	229.4	12.8	83.5	0.5	6,085
BA-45-2	0.5	0.6	345.6	50.1	107.0	-2.7	650
BA-45-3	0.5	0.6	349.2	55.0	115.3	-3.4	669
BA-45-4	0.3	0.6	230.0	10.3	104.8	1.3	3,141
BA-90-1	0.3	0.4	231.2	5.4	83.6	-2.3	6,737
BA-90-2	0.5	0.6	347.4	39.5	123.1	-6.1	829
BA-90-3	0.3	0.4	237.7	0.9	87.0	-1.7	7,508
BA-90-4	0.3	0.6	244.1	9.2	110.6	-2.9	3,179

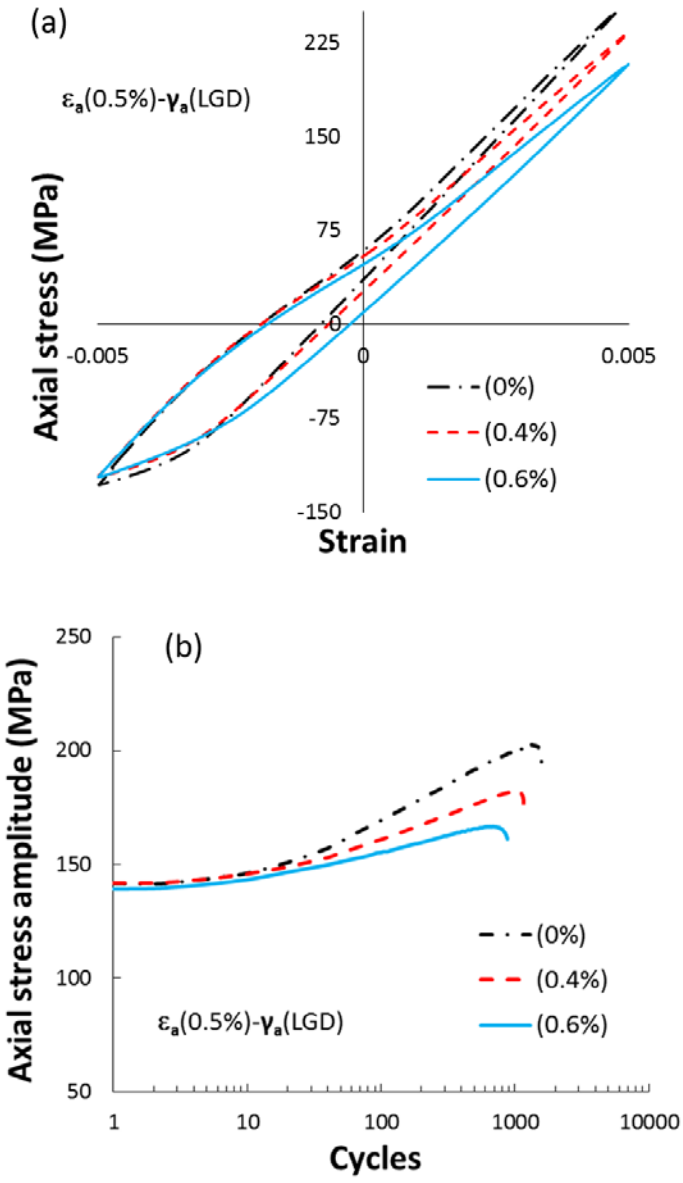

Figure 4.9 (a) Axial stress-strain hysteresis loops and (b) axial stress amplitude variations of experimental alloy during in-phase tests at 0.5% axial strain amplitude and various shear strain amplitudes.

It is known that axial cyclic hardening of AM30 extrusion can be related to the formation of residual twins due to successive twinning/de-twinning processes in each cycle [4,108]. On

one hand, twinned area is rotated towards plastically hard orientations [146]. On the other hand, the residual twins' boundaries hinder dislocation motions on active slip planes [147]. However, as is seen from Figure 4.9(b), the hardening effect of residual twins is found to be attenuated, presumably through larger driving force provided by concomitant shear deformation, which can help dislocation advancement.

The effect of simultaneous axial deformation on the shape of shear hysteresis loop and the evolution of shear stress amplitude during proportional axial-torsional tests are shown in Figure 4.10. The proportional tests include pure torsional at 0.6%, and axial-torsional combining shear strain amplitude of 0.6% with different axial strain amplitudes of 0.3, 0.4 and 0.5%. According to Figure 4.10(a), while pure torsional hysteresis loop is symmetric, axial-torsional cyclic tests show asymmetric shear behaviour. With increasing axial strain amplitude, the asymmetry of shear hysteresis becomes more pronounced. We can even observe a sigmoidal-shape shear unloading reversal with axial strain amplitude of 0.5%. As was reported elsewhere [7], 0.5% corresponded to minimum axial strain amplitude to see de-twinning saturation during the tensile reversal of AM30 extrusion stabilized hysteresis loop. It is stated that the asymmetry of shear hysteresis loop is associated with the occurrence of twinning/de-twinning and the induced change in texture [106,107]. Upon reorienting matrix by twinning, basal slip is more favoured in the twinned portion of microstructure than the matrix. Hence, a higher volume fraction of twins under axial mode will result in easier shear strain accommodation under torsional mode. This is confirmed by the results presented in Figure 4.10(b).

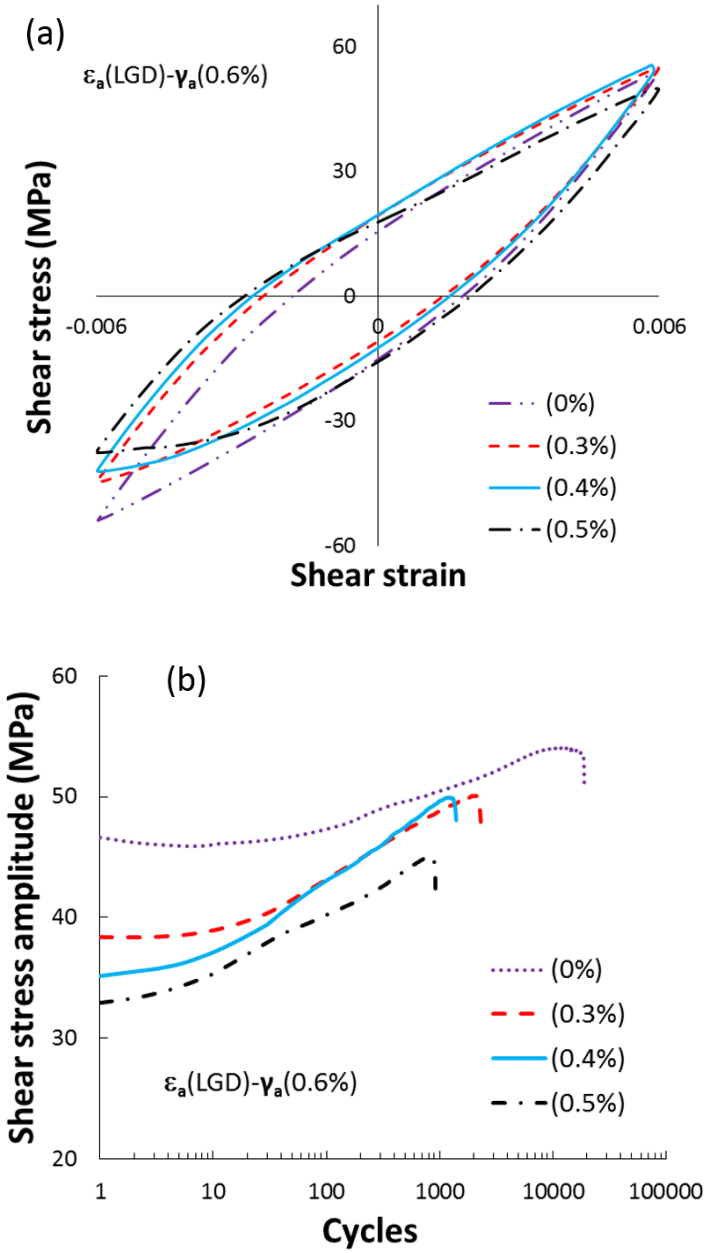

Figure 4.10 (a) Torsional stress-strain hysteresis loops and (b) shear stress amplitude variations of experimental alloy during in-phase tests at 0.6% shear strain amplitude and various axial strain amplitudes.

4.3.2.2 Phase angle effects

Figure 4.11 illustrates the effect of phase angle shift between axial and torsional sinusoidal waveforms on stabilized hysteresis loops at constant axial and shear strain amplitudes of 0.3% and 0.6%, respectively. No significant change in the overall shapes of hysteresis loops can be spotted. There is only a minor reduction of mean stress with increasing phase angle shift, which was also observed in AZ31B extrusion and attributed to the weaker resistance of microstructure to shear deformation in the presence of twins [106]. The volume fraction of twins at the negative tip of shear hysteresis loop is highest for in-phase and lowest for 90° out-of-phase strain path. (See Figure 4.14).

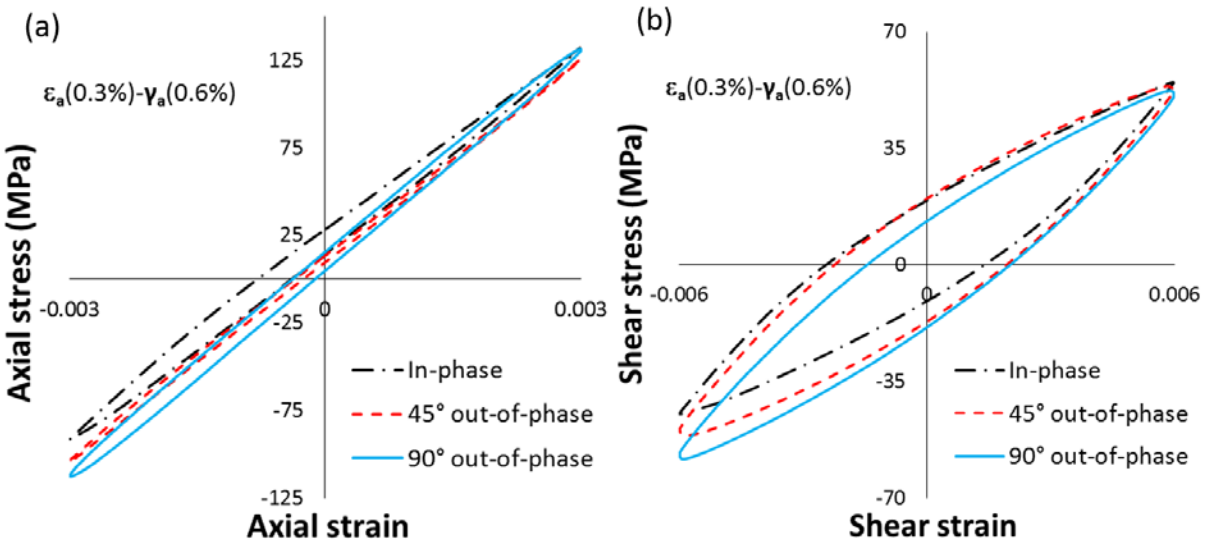

Figure 4.11 Axial and torsional hysteresis loops of AM30 extrusion during cyclic tests at $\varepsilon_a = 0.3\%$, $\gamma_a = 0.6\%$ and different phase angle shifts.

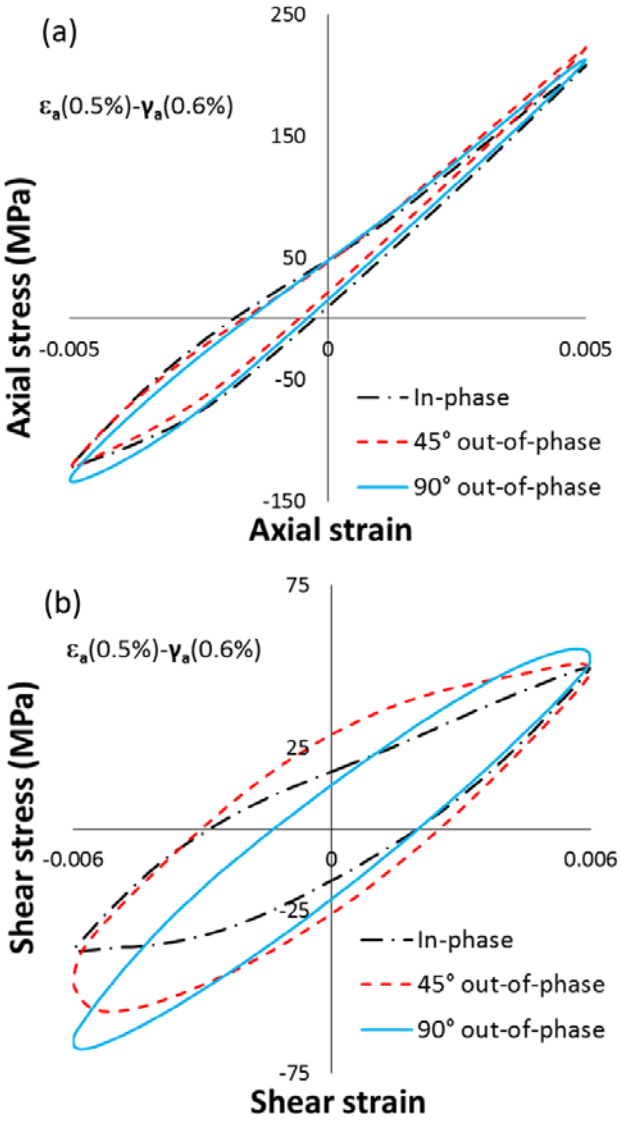

Figure 4.12 Axial and torsional hysteresis loops of AM30 extrusion during cyclic tests at $\varepsilon_a = 0.5\%$, $\gamma_a = 0.6\%$ and different phase angle shifts.

The stabilized stress-strain hysteresis curves of AM30 extrusion subjected to axial and shear strain amplitudes of 0.5% and 0.6%, respectively, applied with different phase angle shifts of 0, 45 and 90° are shown in Figure 4.12. Contrary to the results presented in Figure 4.11, there

is a noticeable change in the shapes of shear hysteresis loops with varying the phase angle shift, while axial hysteresis loops are remained unchanged. Similar observations in Mg alloy extrusions were reported by other researchers [86,106,142]. The changes in shear hysteresis loops are ascribed to the twinning/de-twinning phenomena under axial deformation (see Figure 4.14). It was mentioned earlier that axial strain amplitude of 0.5% during cyclic tension-compression test was found to be the threshold value for the predominance of twinning/de-twinning deformation mechanism at half-life. Therefore, it is concluded that axial hysteresis characteristics are not affected by the non-proportionality of multiaxial loading, whereas, depending on the magnitude of axial strain amplitude, phase angle shift can influence shear hysteresis loops.

Referring to the data in Table 4.2, fatigue lives obtained at $\varepsilon_a(0.3\%)$ and $\gamma_a(0.6\%)$ for the phase angle shifts of 0, 45 and 90° are 3210, 3141 and 3179 cycles, respectively. Furthermore, the fatigue lives at $\varepsilon_a(0.5\%)$ and $\gamma_a(0.6\%)$ for similar phase angle shifts are recorded to be 917, 650 and 829 cycles, respectively. It appears that phase angle shift has no significant effect on the fatigue lives obtained at $\varepsilon_a(0.3\%)$ and $\gamma_a(0.6\%)$, but affects the fatigue lives at $\varepsilon_a(0.5\%)$ and $\gamma_a(0.6\%)$. This may be elucidated by data in Figure 4.13, which shows that total strain energy densities measured at $\varepsilon_a(0.3\%)$ and $\gamma_a(0.6\%)$ with different phase angle shifts are comparable to each other (Figure 4.13(a)), while they are different for various phase angle shifts at $\varepsilon_a(0.5\%)$ and $\gamma_a(0.6\%)$ (Figure 4.13(b)).

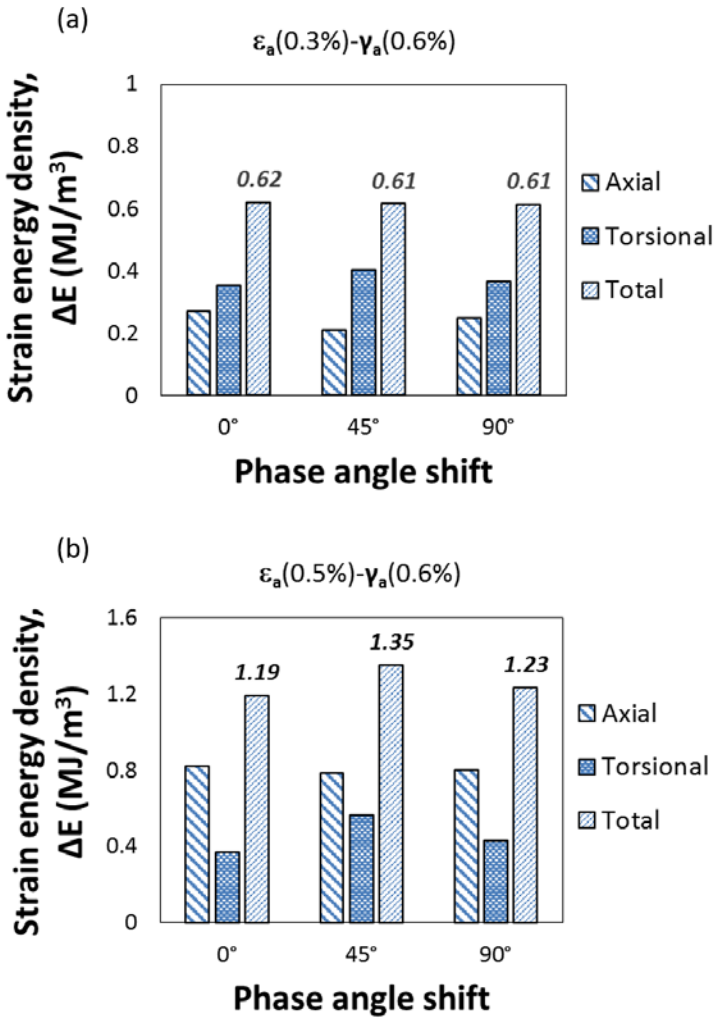

Figure 4.13 Measured axial and torsional strain energy densities for half-life hysteresis loops during cyclic tests at different phase angle shifts: (a) $\varepsilon_a = 0.3\%$, $\gamma_a = 0.6\%$ and (b) $\varepsilon_a = 0.5\%$, $\gamma_a = 0.6\%$.

In order to explore the hardening behaviour of AM30 extrusion under combined axial-torsional loading, the variations of axial and shear stress amplitudes at $\varepsilon_a(0.5\%)$ and $\gamma_a(0.6\%)$ and different phase angle shifts are given in Figure 4.14. For comparison purposes, stress responses from pure axial (at $\varepsilon_a = 0.5\%$) and pure torsional (at $\gamma_a = 0.6\%$) cyclic tests are also

included. It can be seen that with the increase of phase angle shift from 0 to 90°, higher stress amplitudes are exhibited in both axial and torsional modes. This additional non-proportional hardening is much more pronounced in the torsional mode (Figure 4.14(b)). Similar results were reported for AZ31B extrusion [86]. It is worth mentioning that the additional cyclic hardening is a general phenomenon, which happens due to the rotation of principal axes during out-of-phase loading [148,149]. For a grain with arbitrary orientation, the rotation of principal axes will result in the activation of various slip systems and twins along different orientations. Interaction between these activated mechanisms brings about the additional hardening.

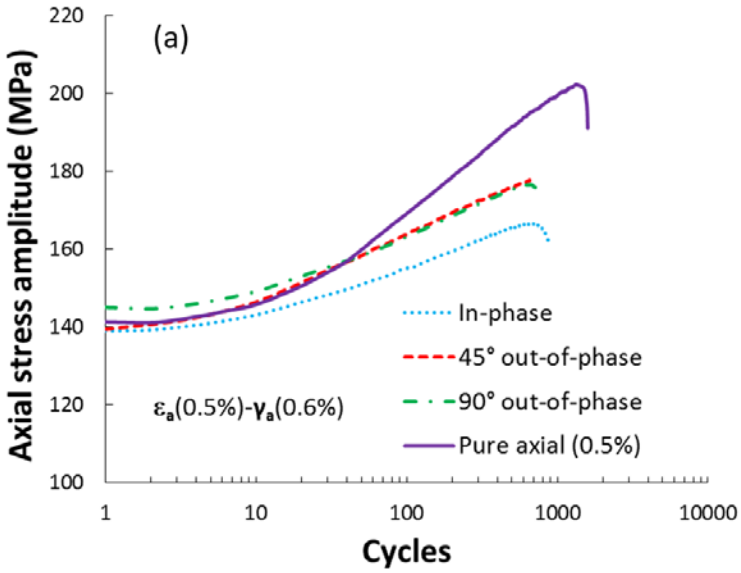

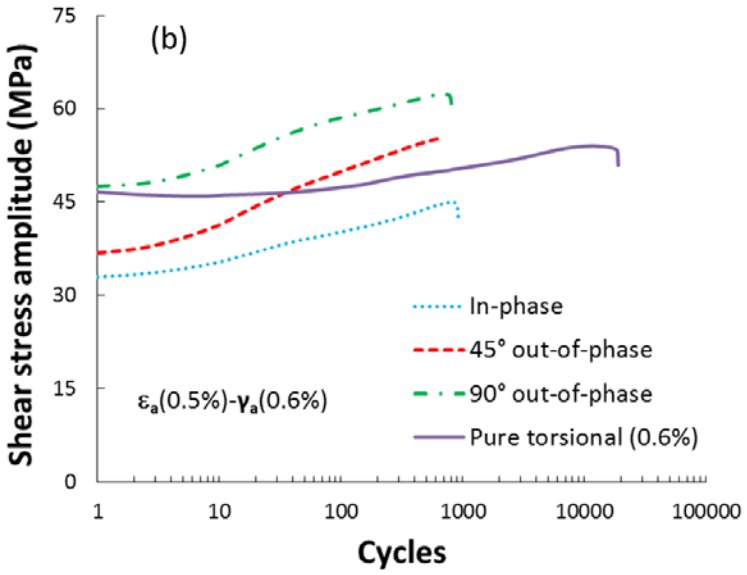

Figure 4.14 The variations of (a) axial and (b) shear stress amplitudes with cyclic straining at $\varepsilon_a = 0.5\%$, $\gamma_a = 0.6\%$ with different phase angle shifts.

4.3.3 Fatigue modelling

Various fatigue damage parameters have been formulated to quantify damage caused to a material under cyclic loading. Critical plane approaches and energy-based models are being commonly applied to a variety of metals [29,143,149–154]. In critical plane approaches a critical plane of material is sought in a way that gives the maximum value of a predefined parameter. To this end, the parameters of interest from stabilized hysteresis loops are first transformed using stress-strain transformation rules (via Mohr's circle method). After pinpointing the critical plane, corresponding model parameters on that plane are extracted and used in a damage equation to find damage parameter. The damage parameter is, ultimately, coupled with a life equation to give life prediction. It is noteworthy that critical plane models

are, theoretically, defined to predict early fatigue cracking orientation, in addition to final fatigue life. Nonetheless, this aspect of critical plane models is not being investigated here.

This section evaluates the fatigue life prediction capabilities of two common critical plane approaches, i.e., Fatemi-Socie and modified Smith-Watson-Topper, as well as Jahed-Varvani as an energy-based approach.

4.3.3.1 Fatemi-Socie (FS)

Fatemi-Socie model [148] was built on Brown and Miller's work [155] by replacing normal strain term with normal stress. The critical plane in this model is defined as the material plane with maximum shear strain value. Its fatigue damage parameter takes the following mathematical form:

$$FS\ Parameter = \gamma_{a,max}\left(1 + k\frac{\sigma_{n,max}}{\sigma_y}\right) \quad \textbf{(4.1)}$$

where $\gamma_{a,max}$ is the maximum shear strain amplitude, $\sigma_{n,max}$ is the maximum normal stress on the maximum shear strain plane (critical plane), and k and σ_y are material constants. The constant k is found in a way that the curves of FS damage parameter versus number of reversals for pure axial (tension-compression) and pure torsional tests are brought together ($k = 1.3$ in this study). The constant σ_y is assumed equal to the monotonic yield strength of the material (200 *MPa* for AM30 extrusion). In Equation (4.1), k/σ_y represents the sensitivity of a material to normal stress [156]. In Figure 4.15(a), the FS parameter is plotted as a function of number of reversals to failure under various loading conditions. Pure axial data were obtained from a

previous article by the authors [7]. As is observed, calculated fatigue damage data using FS criterion are closely converged regardless of different testing circumstances. This confirms the capability of FS model for quantifying fatigue damage under combined axial-torsional cyclic deformation.

Based on FS model, the fatigue damage parameter may be correlated with fatigue life using shear strain-life properties of material. Hence, the following relationship is employed to estimate the fatigue life under different loading conditions:

$$FS\ Parameter = \frac{\tau_f'}{G}\left(2N_f\right)^{b_s} + \gamma_f'\left(2N_f\right)^{c_s} \quad \textbf{(4.2)}$$

where G is the shear modulus (considered 15.1 GPa in this study), and N_f is the number of cycles to fatigue failure. The definitions of the shear strain-life parameters and their corresponding values for AM30 extrusion, calculated from Figure 4.15(b), are listed in Table 4.3. The symbols in Figure 4.15(b) correspond to experimental data obtained from half-life hysteresis loops of pure torsional tests and dashed lines are best power-law fits.

The predicted fatigue lives by FS model are plotted against experimental lives under various loading conditions and is shown in Figure 4.15(c). Diagonal solid line represents perfect match and two parallel long-dashed and dash-dotted lines indicate factor of 2 and 1.5 bounds, respectively, between predicted and experimental lives. Based on the results, all predictions fall within factor of 2 boundaries, though the fatigue lives are mostly under-predicted, especially for pure axial tests in the low-cycle fatigue regime. In general, the results imply the capability of FS model to estimate the axial-torsional fatigue life of AM30 extrusion.

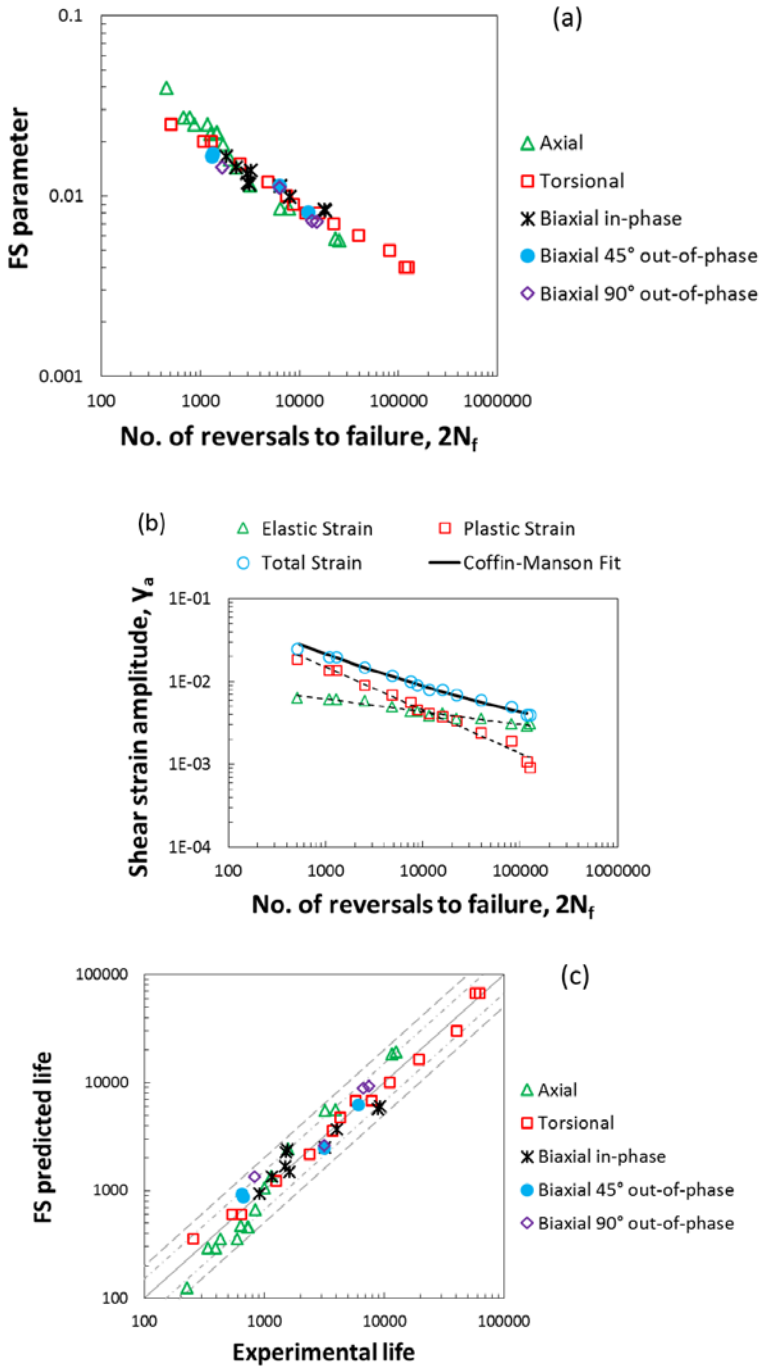

Figure 4.15 (a) Calculated FS parameters under various loading conditions; (b) Shear strain-life data used for extracting shear fatigue properties; (c) The correlation of FS-estimated life with experimental life.

Table 4.3 Shear strain-life parameters used in FS model.

Shear fatigue strength coefficient, τ_f' (*MPa*)	283.818
Shear fatigue ductility coefficient, γ_f'	0.602
Shear fatigue strength exponent, b_s	-0.159
Shear fatigue ductility exponent, c_s	-0.531

4.3.3.2 Modified Smith-Watson-Topper (MSWT)

The SWT parameter has been used by Socie in the multiaxial loading analysis of materials that fail primarily under tensile cracking mode [156]. This critical plane model was shown to be incapable of correlating fatigue data under pure torsional loading of AZ31B extrusion [86,106]. Jiang and Sehitoglu [157] modified SWT parameter to take general cracking mode into account:

$$MSWT\ Parameter = 2b\ \Delta\varepsilon\ \sigma_{max} + \frac{1-b}{2}\Delta\tau\ \Delta\gamma \qquad \textbf{(4.3)}$$

where $\Delta\varepsilon$, $\Delta\tau$ and $\Delta\gamma$ stand for the ranges of normal strain, shear stress and shear strain, respectively, and b is a material constant. The critical material plane in this model is defined as the plane with the maximum value of MSWT parameter. The variable b varies from 0 to 1. For $b = 1$, Equation (4.3) gives the original SWT parameter. It is stated that for the values of b between 0.37 and 0.5, mixed cracking behaviour can be evaluated, while $b \leq 0.37$ and $b \geq 0.5$ enables the model to be used in shear and tensile cracking modes, respectively [106,142]. Figure 4.16(a) depicts the MSWT parameter calculated for different uniaxial and axial-torsional cyclic tests by assuming $b = 0.3$. The value of b implies that shear cracking mode is dominant in the experimental alloy.

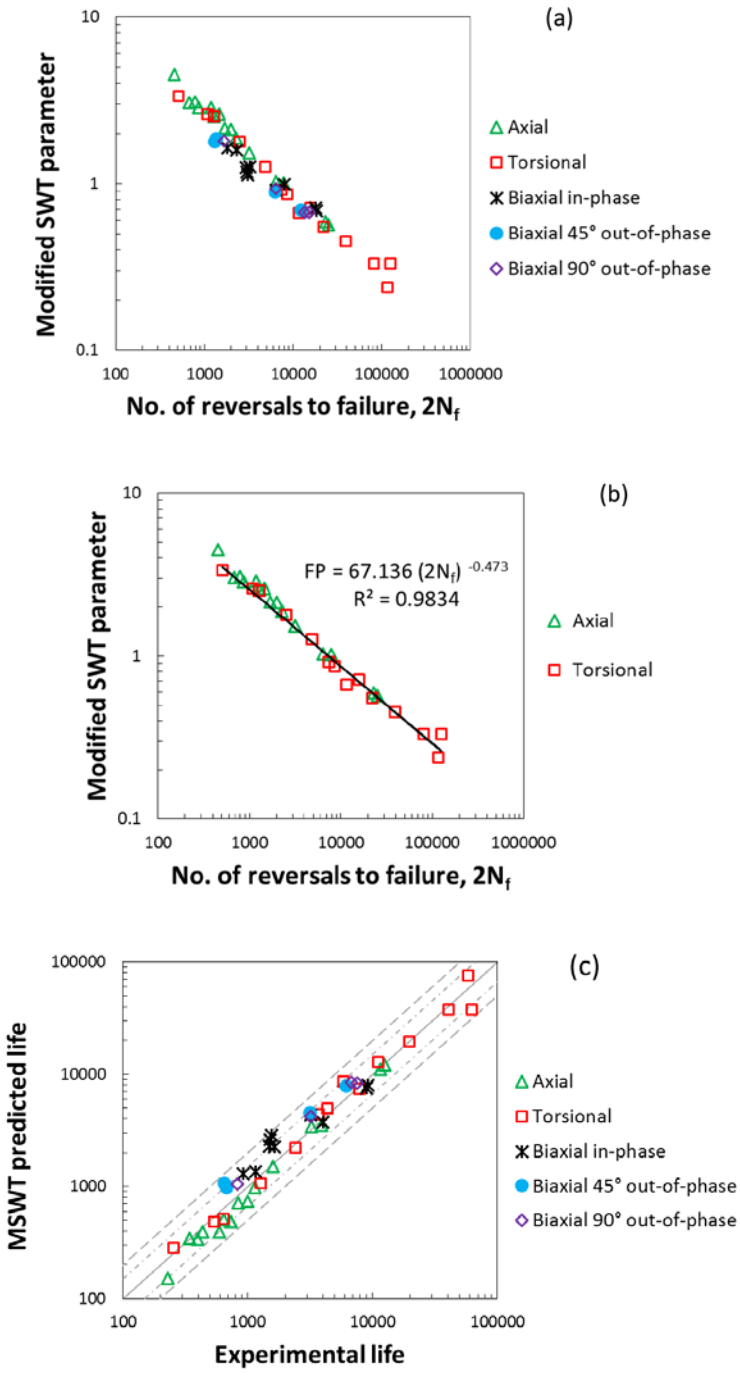

Figure 4.16 (a) Calculated modified SWT parameters under various loading conditions; (b) Power-law relationship between MSWT parameter and number of reversals to failure; (c) The correlation of MSWT-estimated life with experimental life.

According to Figure 4.16(b), the linear relationship between MSWT parameter and number of reversals to failure in a log-log scale can fairly be fitted employing a power-law equation:

$$MSWT\ Parameter = 67.136\left(2N_f\right)^{-0.473} \quad \textbf{(4.4)}$$

Equation (4.4) can be used, in conjunction with Equation (4.3), to estimate fatigue life under various loading conditions. In Figure 4.16(c), the estimated fatigue lives are compared with the experimental ones. It can be deduced that the modified SWT model provides reasonably good fatigue life predictions for AM30 extrusion under pure uniaxial and combined axial-torsional loading. This model had been successfully applied to predict the multiaxial fatigue of AZ31B and AZ61A Mg alloys extrusions [106,142].

4.3.3.3 Jahed-Varvani (JV)

Given the invariant nature of energy as a scalar quantity, energy-based approaches have the potential to be used for multiaxial fatigue life prediction of anisotropic materials such as AM30 Mg alloy extrusion. In current study, Jahed-Varvani's energy-based model [139] will be evaluated on the basis of its life prediction capabilities.

In the JV model, fatigue damage is expressed by total strain energy density, which consists of two different terms, i.e., plastic and positive elastic strain energy densities. The former term is calculated from area inside stabilized hysteresis loop at any strain amplitude:

$$\Delta E_A^p = \oint \sigma_{xx} d\varepsilon_{xx}^p \quad \textbf{(4.5)}$$

$$\Delta E_S^p = \oint \tau_{xy} d\gamma_{xy}^p \quad \textbf{(4.6)}$$

where ΔE_A^p and ΔE_S^p are plastic axial and torsional strain energy densities, respectively. Positive elastic energy can be determined by the following equations:

$$\Delta E_{e,A}^+ = \frac{{\sigma_{max}}^2}{2E} \quad \textbf{(4.7)}$$

$$\Delta E_{e,S}^+ = \frac{{\tau_{max}}^2}{2G} \quad \textbf{(4.8)}$$

where σ_{max} and τ_{max} are, respectively, axial and shear stresses at the positive tip of the hysteresis loops, and E and G are, respectively, the average tensile and average shear moduli of unloading reversals. By introducing positive elastic strain energy density, mean stress effects are also taken into account in this model [140,158]. The axial and shear strain energy densities are, then, related to fatigue life in terms of number of reversals to failure through an equation similar to Coffin-Manson relationship [139,159]:

$$\Delta E_A = E_e'(2N_A)^B + E_f'(2N_A)^C \quad \textbf{(4.9)}$$

$$\Delta E_S = W_e'(2N_S)^{B_s} + W_f'(2N_S)^{C_s} \quad \textbf{(4.10)}$$

where ΔE_A and $2N_A$ are total axial strain energy density and axial fatigue life in reversals, respectively, and ΔE_S and $2N_S$ are their shear counterparts. Remaining symbols in Equations (4.9) and (4.10) denote energy-based fatigue parameters, which are defined in Table 4.4.

Table 4.4 Energy-based fatigue parameters used in JV model.

Axial fatigue strength coefficient, E_e' (MJ/m^3)	9.107
Axial fatigue toughness coefficient, E_f' (MJ/m^3)	20350.770
Axial fatigue strength exponent, B	-0.340
Axial fatigue toughness exponent, C	-1.378
Shear fatigue strength coefficient, W_e' (MJ/m^3)	2.762
Shear fatigue toughness coefficient, W_f' (MJ/m^3)	318.753
Shear fatigue strength exponent, B_s	-0.325
Shear fatigue toughness exponent, C_s	-0.683

In order to find the energy-based fatigue parameters, pure axial (along ED) and pure torsional cyclic tests of AM30 extrusion are utilized to construct the plots of positive elastic/plastic axial/shear energy densities versus fatigue life in log-log scale, as shown in Figure 4.17(a) and (b). From these plots, the energy-based fatigue parameters are determined and tabulated in Table 4.4.

To assess the fatigue life of the experimental alloy under various proportional and non-proportional axial-torsional loading conditions, first axial and shear strain energy densities from stabilized hysteresis loops should be computed. Next, these values together with energy-based fatigue parameters are used in Equations (4.9) and (4.10) to give two fatigue lives; N_A and N_S. These lives correspond to upper and lower bounds for each loading scenario. The actual fatigue life falls at some value between N_A and N_S [139]. In this study, the following equation is observed to result in best life estimations by combining two fatigue life limits:

$$N_f = \frac{\Delta E_A}{\Delta E_T} N_A + \frac{1}{2} \frac{\Delta E_S}{\Delta E_T} N_S \qquad \textbf{(4.11)}$$

where N_f is the final estimated life, and ΔE_T is total strain energy density (sum of axial and shear components). The comparison between JV predicted life and the experimental life is illustrated in Figure 4.17(c). The long-dashed lines represent the factor of 2 limits and dash-dotted lines show the factor of 1.5 boundaries. It is clear that the JV model provides very good predictions within the life factor range of ±1.5.

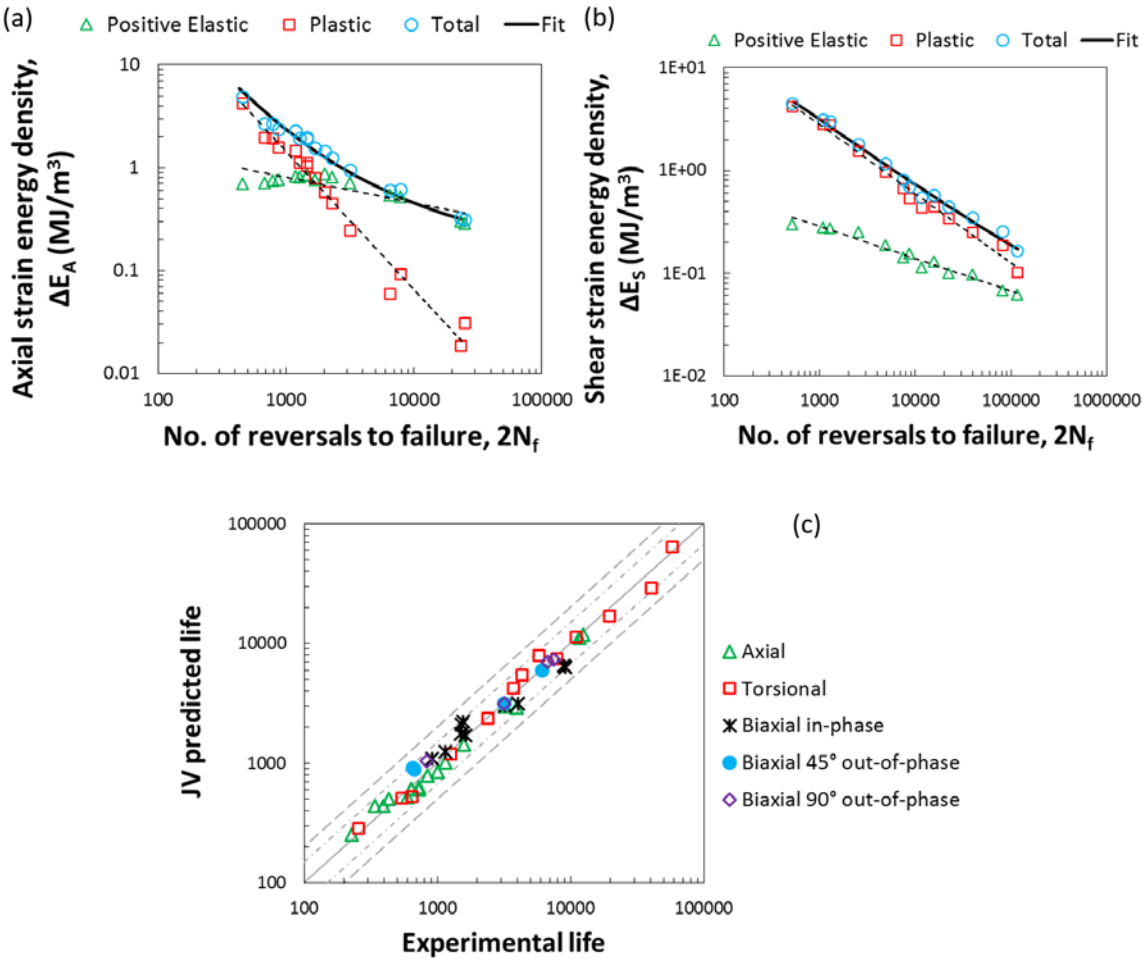

Figure 4.17 (a) Axial and (b) shear strain energy density-life data used for extracting JV model parameters; (c) The correlation of JV-estimated life with experimental life.

4.4 Conclusions

Pure torsional and combined axial-torsional cyclic tests under fully-reversed strain-controlled conditions have been performed on AM30 Mg alloy extrusion. The following main points can be restated from the discussed results:

1) AM30 extrusion exhibits symmetric hysteresis loops upon pure torsional cyclic loading. Slip is, accordingly, considered predominant deformation mechanism, although twinning is proved to happen at very large shear strain amplitudes.
2) AM30 extrusion displays better low-cycle shear fatigue properties than AZ31B and AZ61A extrusions, during strain-controlled cyclic tests.
3) During proportional biaxial cyclic tests, twinning/de-twinning occurrence in axial mode renders the shear response asymmetric. On the other hand, shear deformation is found to only affect the slip-dominated portion of axial hysteresis loop.
4) Axial hysteresis characteristics are not affected by the non-proportionality of multiaxial loading, whereas, depending on the magnitude of axial strain amplitude, phase angle shift can alter shear hysteresis loops.
5) Additional non-proportional hardening is seen for both axial and torsional modes, during combined biaxial deformation of AM30 extrusion.
6) Both critical plane approaches, namely, Fatemi-Socie and Modified Smith-Watson-Topper, as well as Jahed-Varvani energy-based model can suitably predict fatigue life of AM30 Mg alloy extrusion under multiaxial loading conditions.

Chapter 5

Constitutive plastic modelling of wrought magnesium alloys under general loading conditions considering asymmetry/anisotropy

5.1 Introduction

Vehicle lightweighting, as a viable solution for reducing fuel consumption, has made magnesium alloys attractive to automotive industry [1]. Mg parts manufactured via forming processes have the added benefit of enhanced mechanical properties, such as fatigue resistance, over die-cast parts [6,9,10].

In order to design and optimize forming processes for new Mg components, and thereby, reduce their production cost and time, numerical modelling is an effective tool. Finite element (FE) simulation is also essential to evaluate Mg components under service loading conditions. To this end, the development of accurate and efficient material constitutive models to be implemented into commercial FE codes is required. Because of the unusual plastic behaviour of wrought magnesium alloys, however, constitutive modelling is rather a challenging task. This is even more challenging when complex deformation paths including reverse loading is involved. In this context, there have been two major approaches employed by different researchers, namely crystal plasticity approach and continuum phenomenological plasticity approach.

Due to the complex behaviour of magnesium alloys, crystal plasticity approach has been of great interest in constitutive modelling. In recent years, several constitutive models for magnesium alloys in the framework of crystal plasticity have been developed. These models are implemented either in finite element codes for use with commercial FE packages [33,160] or as numerical models including self-consistent [13,31,161] or Taylor models [162–164]. Even though macroscopic stress-strain response and texture predictions of crystal plasticity models are fairly accurate, at least in cases of monotonic loading and uniaxial tension-compression cyclic loading [165], these models are not yet applicable to large-scale industrial forming processes, mainly because of computation power and time concerns.

In continuum plasticity, contrary to crystal plasticity, the underlying deformation mechanisms, dislocation substructures and other crystallographic features along with their associated complexities are neglected and the material (which is viewed as an aggregate of grains in crystal plasticity) is treated as a plastically deforming homogeneous continuum. From this point of view, the equations governing plasticity are being developed using an approach similar to the one used in classical elasticity theory [166].

The ability of this approach to model the plastic behaviour of cubic metals under various loading conditions is known [167,168]. On the other hand, there have been a number of recent endeavors to extend the application of continuum plasticity approach for modelling the unusual behaviour of anisotropic and asymmetric of metals with hexagonal structure (HCP) such as wrought magnesium alloys. Lee et al. [75] modified Dafalias-Popov's two-surface model [73] to include three different deformation modes of twinning, untwinning and slip. They utilized

different hardening curves via different equations for gap distances between bounding and loading curves. A modified Drucker-Prager yield criterion (based on von Mises criterion) was introduced for capturing yield asymmetry and anisotropy. In “TWINLAW” developed by Li et al. [70], yield asymmetry was incorporated using a von Mises yield surface with off-origin center (initial non-zero back stress). To allow for the unusual hardening behaviour of magnesium alloys, they made use of several modified Armstrong-Frederick nonlinear kinematic hardening rules combined with isotropic hardening rule. Kim et al. [27] used two separate yield functions of CPB06 [44,49] and Hill48 [38] for twinning/de-twinning and slip dominated regions, respectively. Moreover, to describe the uniaxial behaviour of AZ31B Mg alloy sheet, empirical reference flow stress equations were suggested based on the dominant deformation mode. Nguyen et al. [80] proposed separate von Mises yield surfaces, each coupled with its own isotropic hardening rule corresponding to different dominant deformation modes (i.e., slip, twinning and de-twinning), to account for the asymmetric hardening behaviour of AZ31B sheet. Muhammad et al. [81] used a similar approach as Nguyen et al. [80] but with three distinct CPB06ex2 [50] yield surfaces and argued that von Mises yield surfaces cannot correctly capture planar anisotropy of AZ31B sheets. More recently, Lee et al. [84] extended distortional anisotropic hardening concept, introduced by Barlat et al. [83] as an alternative for kinematic hardening, to reproduce anisotropic hardening behaviour of AZ31B sheets.

Up to now, all plasticity models for wrought Mg alloys were being formulated in plane stress space, which is acceptable for rolled sheets. However, the stress state of a bulk magnesium component under multiaxial loading cannot be approximated as plane stress and thus,

constitutive formulations in a general state of stress are inevitably necessary. Furthermore, since available asymmetric plasticity models were geared to metal forming applications, their parameters were calibrated based on uniaxial tension/compression loading/unloading/reloading results. However, to be able to use the model for applications involving repetitive cyclic loading, e.g., fatigue life estimation of a load-bearing component, cyclic stabilized hysteresis loops must be utilized to determine model parameters. Moreover, none of the plasticity models so far developed for magnesium alloys have been verified under non-proportional multiaxial cyclic straining paths associated with complex loading which is frequently found in components such as automotive suspension and transmission parts. In view of this, there is a lack of accurate cyclic plasticity model capable of predicting the behaviour under non-proportional as well as proportional cyclic combined loading.

Present chapter puts forward a new phenomenological cyclic plasticity model for wrought Mg alloys based on von Mises isotropic yield surface and a generalized asymmetric/anisotropic Ziegler's kinematic hardening rule. Cyclic biaxial axial-torsional and uniaxial tension-compression tests on various wrought Mg alloys are used to calibrate model parameters. An implicit numerical algorithm is then developed to implement the proposed model into user material subroutine (UMAT) within Abaqus®/Standard FE package. Finally, model is verified by comparing predicted results with newly generated experimental data as well as available data in the literature.

5.2 Materials and experimental procedures

Experimental data for three different wrought magnesium alloys are herein used. Stabilized cyclic hysteresis loops of AZ31B [28,86] and AZ61A [107] Mg alloy extrusions during strain-controlled tests were taken from other researchers' works. Similar data for hot-extruded AM30 Mg alloy (material developed by Luo and Sachdev [3]) were generated by the authors (specimen geometry and test procedure were described in Chapter 4). Additionally, tension-compression (T-C) test results on AM30 flat specimens, machined from extrusion section along extrusion (ED) and transverse (TD) directions, were carried out (more details can be found in Chapter 3).

Notched plate loading-unloading test was performed on an AM30 plate with center hole, with geometry sketched in Figure 5.1(a). The longitudinal (90-*mm* dimension) and transverse (30-*mm* dimension) directions of the notched plate were aligned with ED and TD of the extrusion section, respectively. During the test, load was controlled via a MTS 810 servo-hydraulic uniaxial frame with $50\ kN$ force capacity. Engineering strain field around the notch were computed using a Digital Image Correlation (DIC) system from GOM® GmbH. Prior to the test, a fine speckle pattern was painted on the notched specimen to make it ready for DIC measurements (Figure 5.1(b)).

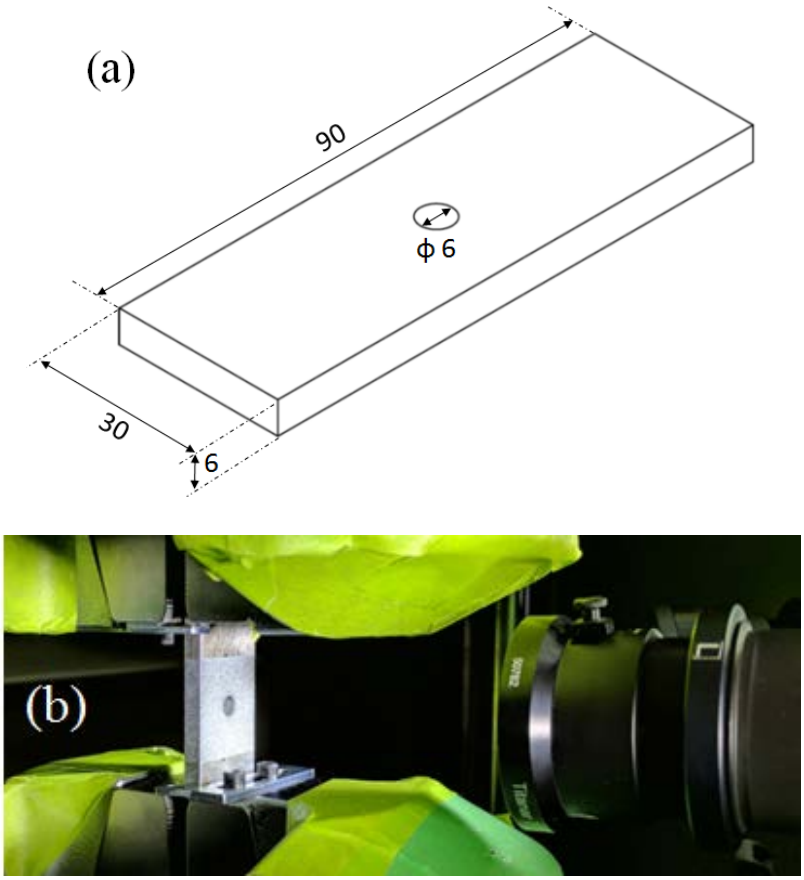

Figure 5.1 (a) Notched plate geometry and dimensions (in *mm*); (b) Notched plate loading-unloading test setup.

5.3 Proposed constitutive model

5.3.1 Plastic characteristics of wrought Mg alloys

Owing to the strong propensity of basal-textured wrought magnesium alloys to mechanical twinning at room temperature, they exhibit exceptional macroscopic characteristics during plastic deformation. In this regard, following experimental observations are taken into consideration while constructing new plasticity model:

- Yield asymmetry: the initial yield stress in tension is much higher than the initial yield stress in compression [169,170]. This difference in yield strength is attributed to the occurrence of extension twinning when compressing perpendicular to c-axes (along ED in AM30 extrusion), and is different from strength differential effect associated with mean normal stress [171].
- Plastic flow asymmetry: during compression along ED (in-plane compression in rolled sheets) or tension following compression, stress-strain curves show a sigmoidal shape, as opposed to its normal shape during tensile deformation [75,172]. This abnormal concavity of the curve is due to the occurrence and then saturation of twinning/de-twinning deformation mechanisms [22,173].
- Directional anisotropy: under both compressive and tensile loading, yielding and hardening behaviour differ from one material orientation to another [52].
- Shear symmetry: unlike axial response, the cyclic shear response of wrought Mg alloys is symmetric [8,107]. Therefore, it is reasonable to assume Masing behaviour under shear loading.

5.3.2 Background

Within the context of purely mechanical rate-independent small-strain plasticity, the increment of strain, $\Delta\boldsymbol{\varepsilon}$, in a continuum under deformation is assumed to be additively decomposed to an elastic, $\Delta\boldsymbol{\varepsilon}^{\boldsymbol{e}}$, and plastic, $\Delta\boldsymbol{\varepsilon}^{\boldsymbol{p}}$, parts:

$$\Delta\boldsymbol{\varepsilon} = \Delta\boldsymbol{\varepsilon}^{\boldsymbol{e}} + \Delta\boldsymbol{\varepsilon}^{\boldsymbol{p}} \quad \textbf{(5.1)}$$

where, bold characters represent second order tensor quantities. The elastic part is assumed to follow the Hooke's law:

$$\Delta\boldsymbol{\varepsilon}^{\boldsymbol{e}} = \boldsymbol{C}^{-1}{:}\,\Delta\boldsymbol{\sigma} \tag{5.2}$$

where, $\Delta\boldsymbol{\sigma}$ is the increment of stress tensor, $\boldsymbol{C}$ is the fourth order elasticity tensor, and ":" denotes double-dot product. It is further assumed that there exists a scalar-valued function, $\emptyset$, defining a smooth hyper-surface, yield surface, in stress space enclosing an elastic region. The plastic component of the strain increment is given by the following normality rule:

$$\Delta\boldsymbol{\varepsilon}^{\boldsymbol{p}} = \zeta\frac{\partial\emptyset}{\partial\boldsymbol{\sigma}} \tag{5.3}$$

where, the plastic multiplier, ζ, is a scalar defining the magnitude of the plastic flow, being calculated from consistency condition.

5.3.3 Yield surface and flow rule

One of the essential elements of continuum-based plasticity models is the definition of yield surface. Yield criterion is required to represent material behaviour under general loading conditions. To better capture yield asymmetry in magnesium alloys, the use of complex yield functions is necessitated, however, representing the general evolution of such yield functions under complex combinations of multiaxial loading is an onerous task [70]. Developing a plasticity model for asymmetric magnesium alloys, insensitive to the choice of initial yield stress, would enable us to employ isotropic yield functions, the evolution of which can be formulated in a much simpler way.

In present study, the plasticity model pivots on proposed hardening rule rather than yield surface definition. Hence, for the sake of simplicity and efficiency, well-established isotropic von Mises yield criterion has been incorporated in the proposed model:

$$\emptyset(\boldsymbol{\sigma}, \boldsymbol{\alpha}) = \varphi(\boldsymbol{\sigma} - \boldsymbol{\alpha}) - \bar{\sigma} = 0 \tag{5.4}$$

$$\varphi(\boldsymbol{\sigma} - \boldsymbol{\alpha}) = \left[{}^{3}/_{2} \, (\boldsymbol{S} - \boldsymbol{A}) : (\boldsymbol{S} - \boldsymbol{A}) \right]^{1/2} \tag{5.5}$$

$$\boldsymbol{S} = \boldsymbol{\sigma} - tr(\boldsymbol{\sigma}) \, \boldsymbol{I} \tag{5.6}$$

$$\boldsymbol{A} = \boldsymbol{\alpha} - tr(\boldsymbol{\alpha}) \, \boldsymbol{I} \tag{5.7}$$

where, $\boldsymbol{\sigma}$, $\boldsymbol{\alpha}$, $\boldsymbol{S}$, and $\boldsymbol{A}$ are stress tensor, back-stress tensor, and their deviators, respectively, $tr(\blacksquare)$ denotes the first invariant (trace) of tensor ■, and $\boldsymbol{I}$ is the identity tensor. The yield surface in Equation (5.4), initially centered at the origin, evolves only by kinematic hardening (represented by back stress tensor, $\boldsymbol{\alpha}$), i.e., it translates in the stress space without changing its shape and size. Hence, the size of the yield surface, $\bar{\sigma}$, is constant.

In plasticity theories with a yield surface, the accurate determination of the size of elastic region is very crucial in order to correctly predict the onset of deviation from linear behaviour [75,167,174]. However, this transition from linear elastic behaviour was observed to be very sudden in most of previously developed models, failing to reproduce experimental elastic-plastic transient behaviour. Since in the current model the choice of initial yield stress has minimal effect on the predicted flow curve (as long as chosen value is less than actual yield stress), by arbitrarily specifying a small value ($20 \, MPa$ in this work), a continuous plastic

modulus function embedded in the kinematic hardening rule, would smoothly reproduce the experimental flow curve from elastic into plastic region.

The plastic strain increment is determined by an associated flow rule for a von Mises yield surface:

$$\Delta \boldsymbol{\varepsilon^p} = \zeta\, \boldsymbol{N} = \Delta p\, \boldsymbol{N} \tag{5.8}$$

$$\Delta p = \left({}^{2}/_{3}\, \Delta \boldsymbol{\varepsilon^p} : \Delta \boldsymbol{\varepsilon^p}\right)^{1/2} \tag{5.9}$$

$$\boldsymbol{N} = \frac{\partial \emptyset}{\partial(\boldsymbol{\sigma} - \boldsymbol{\alpha})} = {}^{3}/_{2}\, \frac{\boldsymbol{S} - \boldsymbol{A}}{\bar{\sigma}} \tag{5.10}$$

where, Δp is equivalent plastic strain increment, and $\boldsymbol{N}$ is the outward tensor normal to the yield surface.

5.3.4 Hardening rule

While yield surface designates the onset of yielding, the hardening rule governs the evolution of yield surface with further plastic deformation. In the proposed model, von Mises yield surface evolves only through kinematic hardening, i.e., translates in stress space without any change in its shape and size. Figure 5.2 shows the evolution of von Mises yield surface according to Ziegler's rule [61,175] for the increment of back stress in the radial direction:

$$\Delta \boldsymbol{\alpha} = d\mu(\boldsymbol{\sigma} - \boldsymbol{\alpha}) \tag{5.11}$$

where, $d\mu$ is a positive scalar.

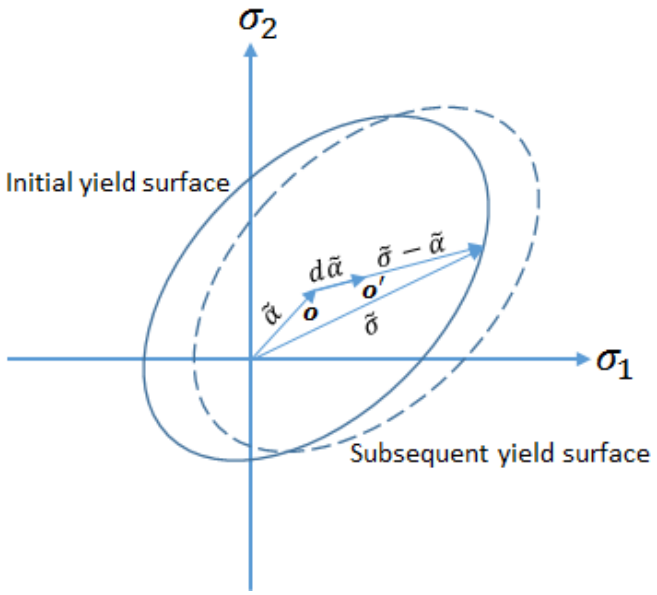

Figure 5.2 Yield surface translation in stress space according to Ziegler's kinematic rule.

With the purpose of describing the unusual cyclic plastic behaviour of wrought magnesium alloys mentioned earlier, an anisotropic generalization of Ziegler's hardening rule [176,177] is proposed for the evolution of back stress tensor:

$$\Delta\boldsymbol{\alpha} = [\boldsymbol{H}]\,\boldsymbol{m}\,\Delta p \tag{5.12}$$

in which, $\boldsymbol{m}$ gives the unit radial tensor:

$$\boldsymbol{m} = \frac{\boldsymbol{\sigma} - \boldsymbol{\alpha}}{\|\boldsymbol{\sigma} - \boldsymbol{\alpha}\|} \tag{5.13}$$

where, $\|\blacksquare\|$ denotes the norm of tensor ■. The matrix $[\boldsymbol{H}]$ in Equation (5.12) contains the hardening or plastic moduli. The matrix form of $[\boldsymbol{H}]$ can be exploited to make explicit reference to the properties of the material along different directions. This way the anisotropic and asymmetric features of cyclic curves of wrought magnesium alloys can be modeled. Besides

that, the proposed model is also able to express material's shear response independently. Under multiaxial loading, material properties along directions involved in the loading, will contribute to the overall plastic response of the material.

As was stated before, the proposed model does not include isotropic hardening, thus the size of the yield surface remains unchanged during plastic straining. Both the increase in yield stress with plastic strain and the difference in initial yield stress in tension and compression are taken care of by the translation of the yield surface in stress space, i.e., kinematic hardening. Excluding isotropic hardening, results in less complexity in the numerical implementation of the proposed model, as will be touched upon later.

5.4 Numerical implementation

The proposed plasticity formulation has been implemented into the FE software package Abaqus®/Standard 6.14-2 [178], via user-defined material subroutine (UMAT). Before looking at numerical procedure in detail, it should be mentioned here that for practical reasons, Voigt notation is used for implementing the constitutive model [166]. In Voigt notation one-dimensional and two-dimensional arrays are representing second-order tensor quantities (e.g., stress and strain) and constitutive tensors (e.g., elastic and plastic moduli), respectively. For instance, stress tensor in Voigt notation is written:

$$\boldsymbol{\sigma} = \begin{bmatrix} \sigma_{xx} & \sigma_{xy} & \sigma_{xz} \\ \sigma_{xy} & \sigma_{yy} & \sigma_{yz} \\ \sigma_{xz} & \sigma_{yz} & \sigma_{zz} \end{bmatrix} \equiv \tilde{\sigma} = \begin{bmatrix} \sigma_{xx} \\ \sigma_{yy} \\ \sigma_{zz} \\ \sigma_{xy} \\ \sigma_{xz} \\ \sigma_{yz} \end{bmatrix} \tag{5.14}$$

in which, the symmetry of stress tensor is used.

5.4.1 Stress update algorithm

In Abaqus®, strain and deformation gradient are passed into the UMAT both at the start and end of a time increment, whereas stress and state variables are provided only at the start of a time increment [166]. Inside UMAT, stress and state variables are updated and Jacobian (material tangent stiffness matrix) is defined.

Incremental Hooke's law is utilized for elastic deformation:

$$\Delta\tilde{\sigma} = [C]\,\Delta\tilde{\varepsilon}^{e} \tag{5.15}$$

where, $\Delta\tilde{\varepsilon}^{e}$ is elastic strain increment vector and $[C]$ is the elasticity modulus given as:

$$[C] = \begin{bmatrix} 2G+\lambda & \lambda & \lambda & 0 & 0 & 0 \\ \lambda & 2G+\lambda & \lambda & 0 & 0 & 0 \\ \lambda & \lambda & 2G+\lambda & 0 & 0 & 0 \\ 0 & 0 & 0 & G & 0 & 0 \\ 0 & 0 & 0 & 0 & G & 0 \\ 0 & 0 & 0 & 0 & 0 & G \end{bmatrix} \tag{5.16}$$

in which, G is the shear modulus and λ is the Lame constant. To decide whether plastic deformation is initiated, elastic predictor-plastic corrector approach is employed. According to this approach, the total strain increment at the beginning of time increment is assumed to be elastic, thereby a trial stress can be calculated:

$$\tilde{\sigma}_{n+1}^{trial} = \tilde{\sigma}_n + [C]\Delta\tilde{\varepsilon} \quad \textbf{(5.17)}$$

Then, if the trial stress does not satisfy the yield condition, Equation (5.4), plastic loading will not initiate and the increment is purely elastic. However, if the trial stress falls outside the yield surface (the size of which does not change in the absence of isotropic hardening) plastic loading occurs. Now, according to consistency condition, it is needed to bring the stress back on the yield surface. This is carried out by correcting the stress state using plastic-corrector term:

$$\tilde{\sigma}_{n+1} = \tilde{\sigma}_{n+1}^{trial} - 2G\ \Delta\tilde{\varepsilon}^{p} = \tilde{\sigma}_{n+1}^{trial} - 2G\ \Delta p\ \widetilde{N} \quad \textbf{(5.18)}$$

Three major integration algorithms have been employed by various researchers to solve for Δp in constitutive Equation (5.18) [179,180]. In forward-Euler integration algorithm, the value of plastic multiplier (equal to Δp for the case of kinematic hardening with von Mises yield criterion, as the case in present study) at the beginning of time increment is used to update the values of stress, plastic strain and state variables at the end of time increment. Thus, the yield condition at the end of time increment is not satisfied, and this may lead to erroneous results due to drifting of the solution away from the yield surface. This deficiency is overcome by the backward-Euler integration algorithm, according to which the yield condition at the end of time increment is ensured to be satisfied. The third integration algorithm is semi-implicit backward-Euler, in which contrary to the backward-Euler scheme, derivatives of the yield function with respect to stress is not needed and hence, can be used with complex yield surfaces. Since the proposed model is associated with simple von Mises yield surface and because of its accuracy and robustness, backward-Euler integration algorithm is utilized in this study. The derivation

procedure for equivalent plastic strain increment based on the backward-Euler integration scheme is elaborated in the following.

In what follows, trial quantities are denoted with superscript $\blacksquare^{trial}$, and $\blacksquare^{T}$ represents the transpose of a vector quantity. We begin by writing Hooke's law in its predictor-corrector form using Voigt notation, following from Equation (5.18):

$$\tilde{S}_{n+1} = \tilde{\sigma}_{n+1}^{trial} - 2G\,\Delta\tilde{\varepsilon}_{n+1}^{p} - {}^{1}/_{3}\,\tilde{I}(\tilde{I}^{T}\cdot\,\tilde{\sigma}_{n+1}) = \tilde{S}_{n+1}^{trial} - 2G\,\Delta p\,\widetilde{N} \tag{5.19}$$

where, $\tilde{I}$ is the identity vector. Using Equation (5.12), we may write Equation (5.10) as:

$$\tilde{S}_{n+1} = \tilde{A}_{n} + \Delta\tilde{A} + {}^{2}/_{3}\;\bar{\sigma}\,\widetilde{N} \tag{5.20}$$

Combining Equations (5.19) and (5.20), taking the inner product of both sides with $\widetilde{N}$ leads to:

$$\left(\tilde{S}_{n+1}^{trial} - \tilde{A}_{n}\right)^{T}\cdot\,\widetilde{N} = \widetilde{N}^{T}\cdot\,\widetilde{N}\left(2G\,\Delta p + {}^{2}/_{3}\;\bar{\sigma} + \Delta\tilde{A}\right) \tag{5.21}$$

where:

$$\widetilde{N}^{T}\cdot\,\widetilde{N} = {}^{3}/_{2} \tag{5.22}$$

$$\Delta\tilde{A} = \left([H]\widetilde{m} - {}^{1}/_{3}\,\tilde{I}(\tilde{I}^{T}\cdot\,[H]\widetilde{m})\right)\Delta p \tag{5.23}$$

so that:

$$\Delta p = \frac{\left(\tilde{S}_{n+1}^{trial} - \tilde{A}_{n}\right)^{T}\cdot\,\widetilde{N} - \bar{\sigma}}{\left([H]\cdot\widetilde{m} - {}^{1}/_{3}\,\tilde{I}(\tilde{I}^{T}\cdot\,[H]\cdot\widetilde{m})\right)^{T}\cdot\,\widetilde{N} + 3G} \tag{5.24}$$

In Equation (5.24), none of the terms on the right-hand side (including the initial size of yield surface, $\bar{\sigma}$) depends on equivalent plastic strain increment. This equation is, thus, a closed-form expression, which gives the solution without the need for any iteration (e.g., Newton-Raphson iterative method mostly employed in available plasticity models). In this sense, the proposed model can be considered as a computationally-efficient tool for design and optimization in large-scale practical applications under complex loading conditions. After Δp is calculated, stress increment will be obtained from following equations:

$$\widetilde{N} = \frac{\tilde{S}_{n+1}^{trial} - \tilde{A}_n - \Delta\tilde{A}}{2G\,\Delta p + {}^{2}/_{3}\;\bar{\sigma}} \tag{5.25}$$

$$\Delta\tilde{\sigma} = [C] \cdot \left(\Delta\tilde{\varepsilon} - \Delta p\,\widetilde{N}\right) \tag{5.26}$$

In wrought magnesium alloys, because of directional anisotropy and yield asymmetry, it is essential for a cyclic plasticity model to define a criterion for distinguishing load path changes. In this research, reverse yielding criterion introduced by Lee et al. [181] is incorporated into the proposed plastic constitutive model. According to this criterion, the angle between two unit radial vectors in two subsequent time increments (Λ) is calculated and contrasted with a pre-determined reference angle (Λ_r). Reverse yielding happens when following condition satisfies:

$$\Lambda = cos^{-1}\left(\widetilde{m}_n{}^{T} \cdot\; \widetilde{m}_{n+1}\right) \geq \Lambda_r \tag{5.27}$$

The reference angle is assumed to be ${}^{\pi}/_{2}$. For values of Λ less than Λ_r, forward yielding is occurring.

At first increment into the plasticity, hardening properties (plastic modulus) along each direction is determined based on the sign of the corresponding outward normal vector component, $\widetilde{N}$. Such that, for positive and negative values, respectively, tension and compression properties are considered. For subsequent plastic increments, the angle Λ is calculated and checked against Λ_r according to Equation (5.27), to decide whether current plastic modulus function needs to be maintained or updated.

5.4.2 Continuum tangent stiffness

In implicit FE formulation, in addition to constitutive equations' integration scheme, the elasto-plastic tangent stiffness matrix should also be provided. Since the accuracy of solution is not affected by the definition of tangent stiffness matrix [166], a continuum formulation for the direct derivation of tangent stiffness matrix from constitutive plasticity equations is employed in current study. Any incremental change in stress and back stress should satisfy the consistency condition:

$$\emptyset(\tilde{\sigma} + \Delta\tilde{\sigma}, \tilde{\alpha} + \Delta\tilde{\alpha}) = \emptyset(\tilde{\sigma}, \tilde{\alpha}) + \left(\frac{\partial \emptyset}{\partial \tilde{\sigma}}\right)^T \cdot \Delta\tilde{\sigma} + \left(\frac{\partial \emptyset}{\partial \tilde{\alpha}}\right)^T \cdot \Delta\tilde{\alpha} = 0 \quad \textbf{(5.28)}$$

Using Eqs. (1), (3), (7) and (21):

$$\left(\frac{\partial \emptyset}{\partial \tilde{\sigma}}\right)^T \cdot \Delta\tilde{\sigma} - \left(\frac{\partial \emptyset}{\partial \tilde{\sigma}}\right)^T \cdot \Delta\tilde{\alpha} = 0 \quad \textbf{(5.29)}$$

$$\left(\frac{\partial \emptyset}{\partial \tilde{\sigma}}\right)^T \cdot [C] \cdot \left(\Delta\tilde{\varepsilon} - \zeta \frac{\partial \emptyset}{\partial \tilde{\sigma}}\right) - \left(\frac{\partial \emptyset}{\partial \tilde{\sigma}}\right)^T \cdot (\zeta[H] \cdot \tilde{m}) = 0 \quad \textbf{(5.30)}$$

Finding ζ from Equation (5.30) and combining with Equation (5.26) gives the continuum tangent stiffness matrix:

$$\frac{\Delta\tilde{\sigma}}{\Delta\tilde{\varepsilon}} = [C] - \frac{[C]\cdot {}^{\partial\emptyset}/_{\partial\tilde{\sigma}} \otimes [C]\cdot {}^{\partial\emptyset}/_{\partial\tilde{\sigma}}}{\left({}^{\partial\emptyset}/_{\partial\tilde{\sigma}}\right)^{T}\cdot\left([C]\cdot {}^{\partial\emptyset}/_{\partial\tilde{\sigma}}\right) + \left({}^{\partial\emptyset}/_{\partial\tilde{\sigma}}\right)^{T}\cdot([H]\cdot\tilde{m})} \qquad \textbf{(5.31)}$$

in which $\otimes$ operates the dyadic product of two vectors.

5.5 Results and discussion

In order to demonstrate the capability of the proposed phenomenological constitutive model for various applications of wrought Mg alloys, two types of experiments are considered: proportional and non-proportional biaxial cyclic tests (B-C) as well as compression tests with different tensile pre-strains (T-C). First, using experimental data on two Mg alloy extrusions, AZ31B under B-C conditions and AM30 subjected to T-C tests, procedure for the extraction of model parameters is explained. Then, calibrated model is validated by predicting the response of wrought Mg alloys.

5.5.1 Model calibration

Finding proper functions for the components of $[H]$ matrix, Equation (5.32), will complete the development of the new model. To this end, consistency condition (necessitating the stress state to remain on the yield surface during plastic loading) in conjunction with flow rule and yield criterion, can be employed to give following equation for the plastic multiplier:

$$\zeta = \frac{\widetilde{N}^T \cdot \Delta\tilde{\sigma}}{\widetilde{N}^T \cdot ([H] \cdot \tilde{m})} \tag{5.32}$$

Bearing in mind that the plastic multiplier for von Mises plasticity equals to equivalent plastic strain increment, Δp, from normality rule multiaxial plastic modulus function is obtained from:

$$h_p = \widetilde{N}^T \cdot ([H] \cdot \tilde{m}) \tag{5.33}$$

Equation (5.33) implies that during multiaxial loading, the hardening rate at each time increment is decided by the relative share of applied loading (determined through $\tilde{m}$) experienced by material along each direction. Furthermore, Equation (5.33) allows for calibrating the components of the $[H]$ matrix corresponding to material properties in different directions, as follows.

In order to calibrate model parameters for different types of magnesium alloys, it is needed to find proper forms of mathematical functions to fit experimental plastic modulus data exhibited by material during simple uniaxial tension-compression as well as pure shear cyclic tests. It should be noted that plastic moduli matrix, $[H]$, in Voigt notation is a diagonal matrix with independent components each referring to the plastic modulus of the material along one specific direction.

$$[H] = \begin{bmatrix} H_{11} & 0 & 0 & 0 & 0 & 0 \\ 0 & H_{22} & 0 & 0 & 0 & 0 \\ 0 & 0 & H_{33} & 0 & 0 & 0 \\ 0 & 0 & 0 & H_{12} & 0 & 0 \\ 0 & 0 & 0 & 0 & H_{13} & 0 \\ 0 & 0 & 0 & 0 & 0 & H_{23} \end{bmatrix} \tag{5.34}$$

First, uniaxial cyclic tension-compression will be considered. For condition of uniaxial tension-compression (UTC) loading in 11-direction, since the first components of stress and thereby back stress are the only non-zero components, $\widetilde{m}$ may be written from Equation (5.13):

$$\widetilde{m}^T = [1 \quad 0 \quad 0 \quad 0 \quad 0 \quad 0] \tag{5.35}$$

As a result of incompressibility assumption, it is known that the plastic strain increment is a deviatoric quantity. Thus, under uniaxial loading conditions, the plastic strain increment is defined by:

$$(\Delta\tilde{\varepsilon}^p)^T = \left[\Delta\varepsilon_{11}^p \quad -\Delta\varepsilon_{11}^p/2 \quad -\Delta\varepsilon_{11}^p/2 \quad 0 \quad 0 \quad 0\right] \tag{5.36}$$

where $\Delta\varepsilon_{11}^p$ is the component of plastic strain increment vector in the loading direction (11-direction). We may now determine the components of $\widetilde{N}$, outward normal to the yield surface at loading point, employing Equations (5.8) and (5.9):

$$\widetilde{N}^T = \left[1 \quad -1/2 \quad -1/2 \quad 0 \quad 0 \quad 0\right] \tag{5.37}$$

Subsequently, the uniaxial plastic modulus can be calculated by substituting Equations (5.35) and (5.37) into Equation (5.33):

$$h_p^{UTC} = N_{11}H_{11}m_{11} = H_{11} \tag{5.38}$$

Equation (5.38) means that an empirical fit function can be used to represent the evolution of experimental plastic modulus with progression of uniaxial cyclic plastic straining along 11-direction.

To account for yield asymmetry observed in wrought Mg alloys during tension and compression, a general function for the plastic modulus in 11-direction is assumed to take the following form:

$$H_{11} = [H_0 + \nabla H_L\, \vartheta(N_{11}) + \nabla H_U\, \vartheta(-N_{11})]\, |m_{11}| \tag{5.39}$$

where subscripts $\blacksquare_L$ and $\blacksquare_U$ denote functions for loading (tensile) and unloading (compressive) reversals, respectively, H_0 is a material parameter and ϑ is a Heaviside step function as follows:

$$\vartheta(x) = \begin{cases} 1 & x \geq 0 \\ 0 & x < 0 \end{cases} \tag{5.40}$$

A typical uniaxial tension-compression stabilized hysteresis loop for AZ31B Mg alloy extrusion is shown in Figure 5.3. To be able to clearly see the evolution of plastic modulus with plastic strain, the curves of flow stress and plastic modulus variations against plastic strain for tensile and compressive reversals in Figure 5.3, are separated and illustrated in Figure 5.4. Note that for each reversal, stress-total strain curve in absolute value is first transferred to the origin and then the plastic strain is computed from the total strain.

As is seen in Figure 5.4(a), plastic modulus corresponding to compressive reversal is initially high and gradually reduces with further straining. The metal under this condition is believed to be deforming predominantly by twinning mechanism [22,182]. Similar trend for tensile reversal is observed in Figure 5.4(b) up to a point, after which the plastic modulus is rapidly increasing. This is attributed to the exhaustion of de-twinning and transition of predominant mechanism to slip [26,183].

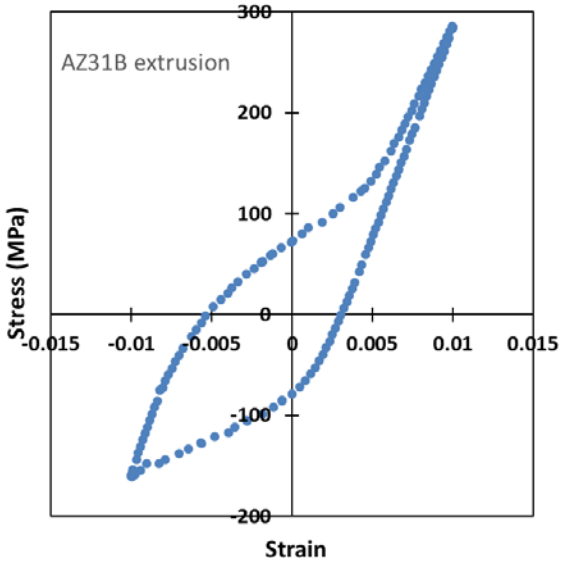

Figure 5.3 Typical uniaxial stabilized hysteresis for AZ31B Mg alloy extrusion [28]**.**

To correctly fit the experimental *S*-shaped hysteresis loops, sigmoid fit functions must be considered. In this study, hyperbolic tangent functions of the following form have been utilized to capture different features of plastic modulus curves:

$$\nabla H_{L,U} = \frac{h_{L,U}}{2}\left[1 + tanh\left(\frac{\sigma_{11} - z_{L,U}}{d_{L,U}}\right)\right] \tag{5.41}$$

where $h_{L,U}$, $z_{L,U}$ and $d_{L,U}$ are material parameters to be calibrated based on the experimental results and σ_{11} is the component of stress in 11-direction. $h_{L,U}$ adjusts the overall strength of the plastic modulus function; $z_{L,U}$, $d_{L,U}$ control, respectively, the position and width of inflection point, relating to twinning/de-twinning saturation. With regard to the compressive reversal, Figure 5.4(a), a single-sigmoid function is sufficient for fitting experimental curve, whereas, a double-sigmoid function is needed to capture two peaks observed in Figure 5.4(b). It is noteworthy that, in general, a double-peak function is required for compressive reversal, as well,

due to the occurrence of twinning exhaustion at high enough compressive strains [134]. That being said, to reduce the number of constants to be found, a single-peak function is chosen for the compressive reversal.

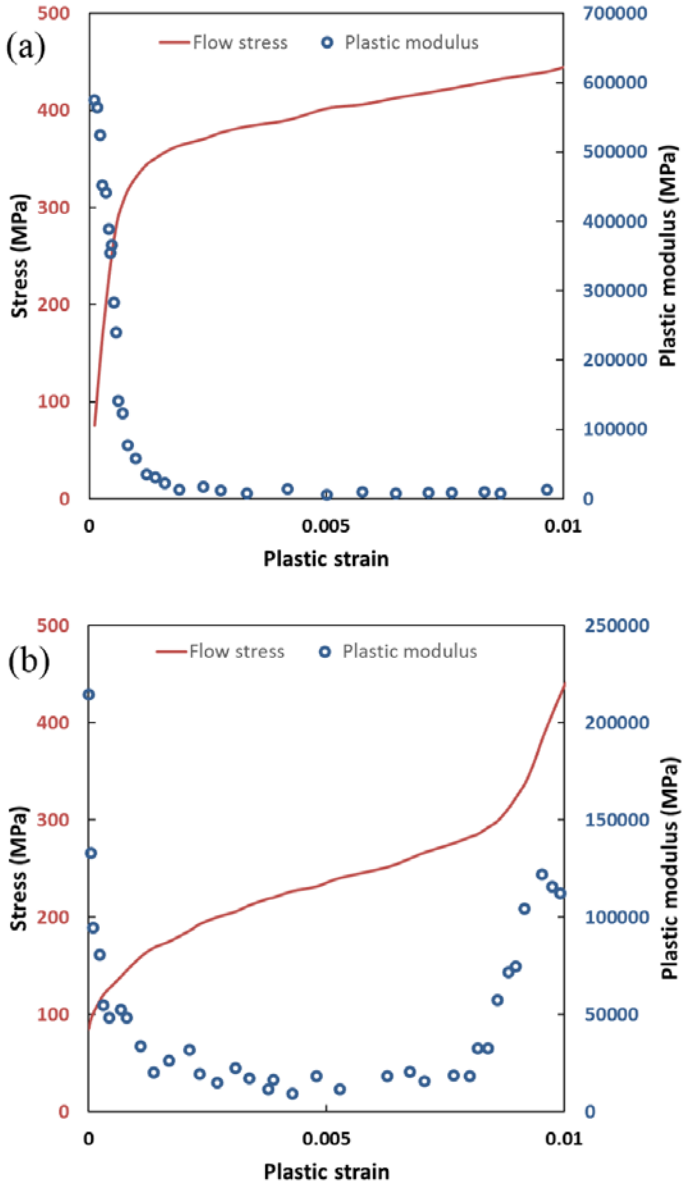

Figure 5.4 Flow stresses and plastic moduli of AZ31B extrusion [28] **as a function of absolute plastic strain for (a) compressive and (b) tensile reversals.**

Under pure shear (PS) conditions, Equation (5.33) reduces to:

$$h_p^{PS} = {}^{1}\!/_{\sqrt{6}} H_{12} \tag{5.42}$$

where h_p^{PS} is the experimental plastic modulus during cyclic pure shear loading in 12-direction. As is known, unlike the axial behaviour, the shear behaviour of magnesium alloys can be approximated to be symmetric. In addition, it is safe to assume Masing behaviour for wrought magnesium alloys under pure shear loading. Taking these assumptions into consideration, therefore, a Ramberg-Osgood power relation is proposed as fitting function for experimental shear plastic modulus:

$$H_{12} = 2^{(1-n_s')} n_s' K_s' \left(\frac{2^{(n_s'-1)} \Sigma_{12}}{K_s'} \right)^{\frac{n_s'-1}{n_s'}} \left(\sqrt{2} |m_{12}| \right) \tag{5.43}$$

where, n_s' and K_s' are cyclic shear strain hardening exponent and cyclic shear strength coefficient, respectively, and Σ_{12} is the translated shear stress component in 12-direction given by:

$$\Sigma_{12} = \left| |\sigma_{12}^R| + Sgn(N_{12}) \sigma_{12} \right| \tag{5.44}$$

$$Sgn(x) = \begin{cases} 1 & x \geq 0 \\ -1 & x < 0 \end{cases} \tag{5.45}$$

in which, σ_{12}^R is the value of σ_{12} at first reversing point. The Ramberg-Osgood coefficients can be extracted from the plot of cyclic shear stress-true plastic shear strain in a logarithmic scale.

Using the uniaxial cyclic tension-compression tests along ED as well as cyclic pure shear tests at various strain amplitudes, the model parameters in Equations (5.41) and (5.43) are

calibrated for AZ31B Mg alloy extrusion and listed in Table 5.1, in which ε_{11}^{R} represents axial strain component in 11-direction at reversing point.

Employing parameters from Table 5.1, the cyclic uniaxial tension-compression and pure shear tests are reproduced and superposed to the experimental results for AZ31B extrusion in Figure 5.5. Open symbols and solid lines show the experimental and simulation results, respectively. Three different strain amplitudes are selected for each loading condition. According to Figure 5.5, the measured and simulated hysteresis loops are in good agreement. Significantly, a smooth transient behaviour from elastic to plastic region and tensile reversal with upward concavity are correctly captured.

Table 5.1 Parameters of the proposed model for stabilized cyclic response of AZ31B Mg alloy extrusion.

Parameters	First term (MPa)	Second term (MPa)
h_L	-247000	$1.05 \times 10^9 {\varepsilon_{11}^R}^2 - 2.58 \times 10^7 \varepsilon_{11}^R + 229500$
z_L	$5 \times 10^6 {\varepsilon_{11}^R}^2 - 95000\varepsilon_{11}^R + 360$	$-2.9 \times 10^6 {\varepsilon_{11}^R}^2 + 57916\varepsilon_{11}^R - 157$
d_L	80	20
h_U	596000	$-$
z_U	$-2.9 \times 10^6 {\varepsilon_{11}^R}^2 + 57916\varepsilon_{11}^R - 262$	$-$
d_U	-50	$-$
Shear	$K_s^{'} = 384.27\ MPa, n_s^{'} = 0.3077$	

The proposed model is also calibrated in the same way through T-C tests performed on AM30 extrusion at strains of 0.004 and 0.02, along ED and TD, and obtained parameters are listed in Table 5.2. Figure 5.6 shows comparisons of the predicted T-C flow curves (solid lines) at different strains along different directions, with those obtained experimentally (symbols). As is seen, there is a good accordance between calculated and experimental results, even for the tests not used for parameter extraction.

Table 5.2 Parameters of Equation (5.41) for T-C response of AM30 Mg alloy extrusion.

Parameters	First term (MPa)		Second term (MPa)	
	ED	TD	ED	TD
h_L	-348000	-10^6	$-$	$-$
z_L	180	30	$-$	$-$
d_L	10	42	$-$	$-$
h_U	-99000	-98500	4×10^5	$\begin{cases}60000 & \varepsilon_{22}^R > 0.004\\ 120000 & \varepsilon_{22}^R \le 0.004\end{cases}$
z_U	-180	-150	$\begin{cases}75 & \varepsilon_{11}^R > 0.004\\ 70 & \varepsilon_{11}^R \le 0.004\end{cases}$	$\begin{cases}60 & \varepsilon_{22}^R > 0.004\\ 75 & \varepsilon_{22}^R \le 0.004\end{cases}$
d_U	10	10	10	10

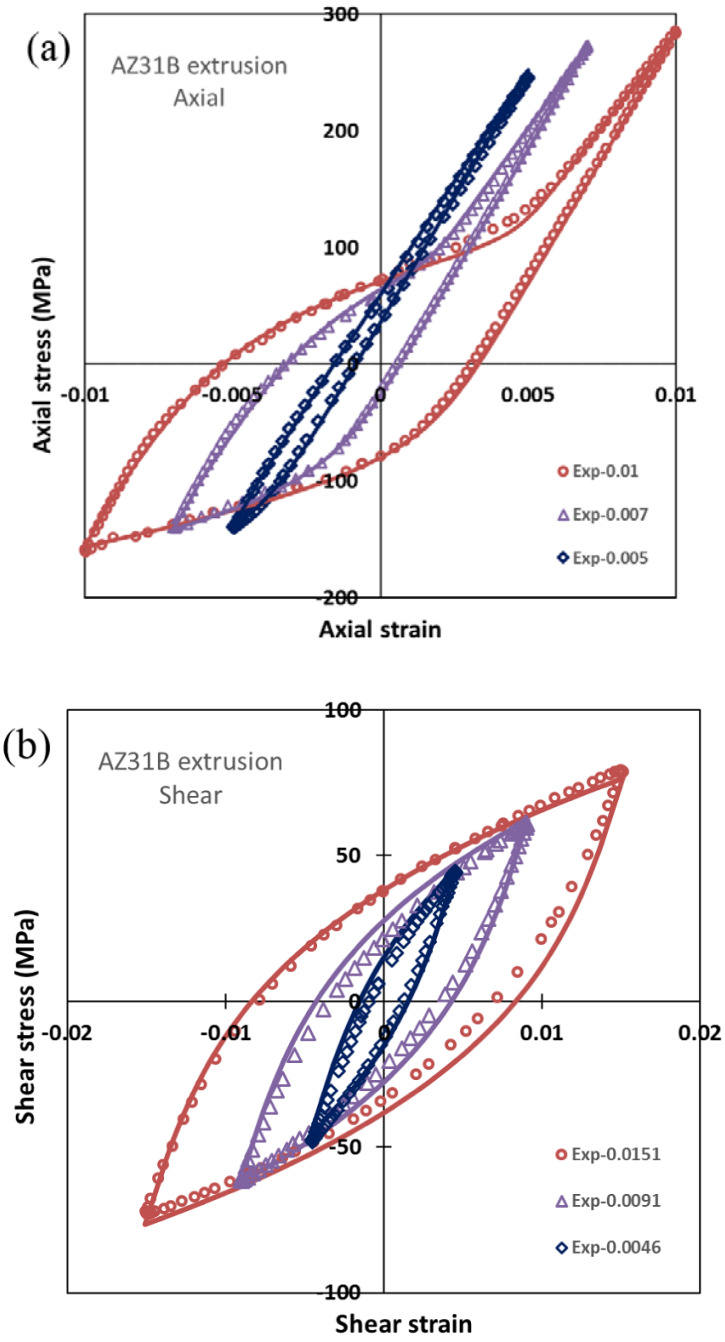

Figure 5.5 Comparisons of measured [28] **and modelled stabilized stress-strain responses for AZ31B extrusion during cyclic (a) uniaxial tension-compression and (b) pure shear loading.**

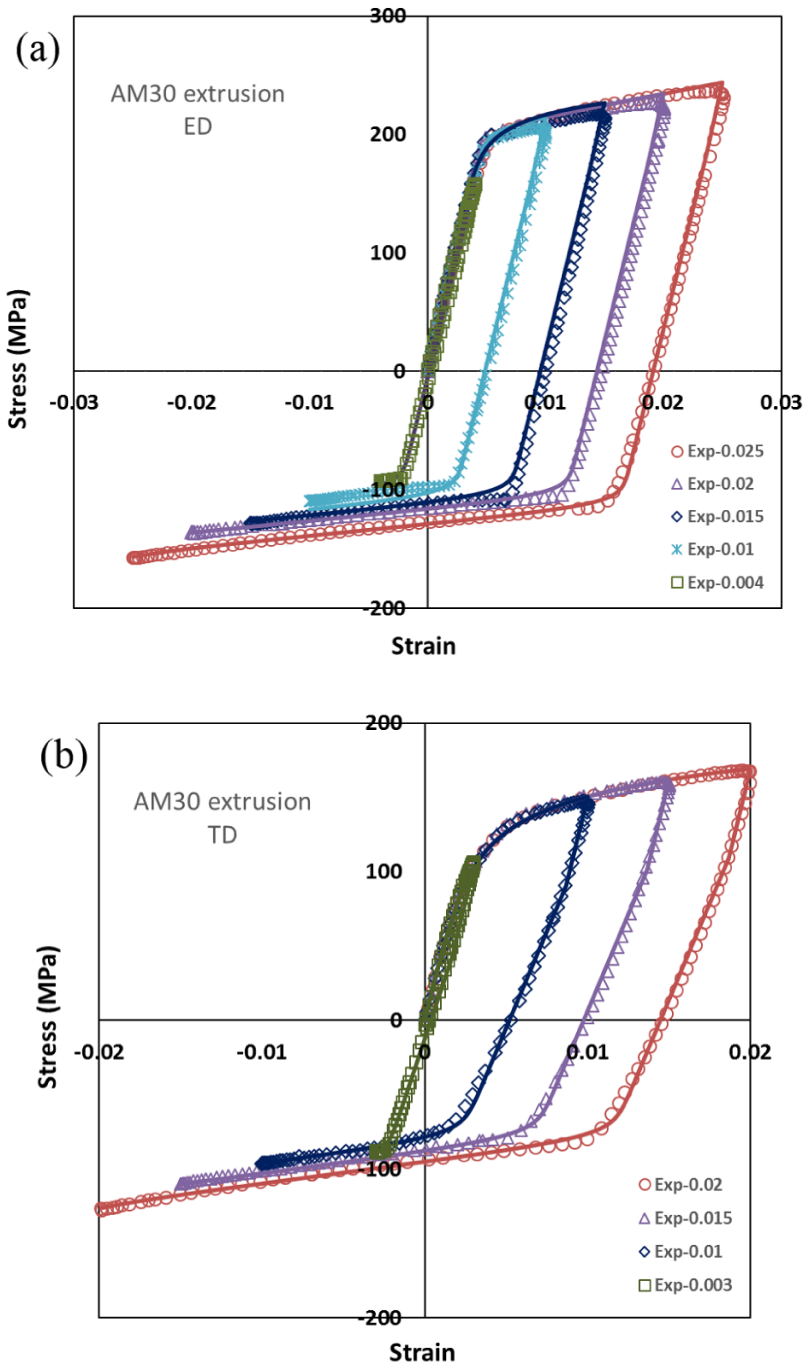

Figure 5.6 Experimental stress-strain curves of AM30 extrusion during compression tests with various tensile pre-strains along ED and TD, compared with simulation results.

5.5.2 Model verification

For verification purposes, experimental results from axial-torsional cyclic tests and notched plate loading-unloading test have been employed to assess various aspects of the proposed model. Evaluating the proposed model using multiaxial cyclic test results proves that the model can be geared towards providing an accurate prediction of stabilized hysteresis loops under complex loading paths for improving the fatigue life assessment of wrought magnesium alloys. Moreover, validation with notched plate loading-unloading test results confirms the accuracy and efficiency of numerical implementation in evaluating a real-life structure via commercial FEM packages. It also shows that the developed model can be applied to industrial forming operations, accounting for anisotropy and deformation path changes.

5.5.2.1 Biaxial axial-torsional strain-controlled cyclic tests

Having the model parameters calibrated through fitting plastic moduli curves along different directions, it is speculated that the stabilized cyclic plastic behaviour of the material subjected to combined complex loading paths can be predicted. To confirm the generality of the proposed model, in addition to generated data by authors on AM30 extrusion, biaxial axial-torsional stabilized cyclic test results on AZ31B [28] and AZ61A [107] magnesium alloy extrusions under various loading conditions are reproduced from literature. The developed numerical algorithm is implemented into MATLAB® code, which gives the same output as a single-element finite element simulation via UMAT code.

Axial and shear response predictions of AZ31B, AZ61A and AM30 Mg alloy extrusions under proportional (in-phase) B-C loading conditions are compared with the measured

stabilized responses in Figure 5.7 and Figure 5.8. Two different combinations of axial and shear strain amplitudes for each material are selected for validation. Overall, the proposed model successfully predicts the stabilized axial and shear stress-strain curves of all three wrought Mg alloys during combined loading conditions. The sigmoidal-shaped hardening response and asymmetric behaviour in tension and compression under axial plastic deformation are well captured. More interestingly, asymmetric shear behaviour due to the occurrence of twinning and de-twinning saturation during axial tensile reversal (multiaxial deformation effects as explained by authors in Chapter 4) is properly modelled. This can best be observed in Figure 5.8(b), where model prediction closely accords with experimental results showing a semi-sigmoidal-shaped shear hysteresis. It is also to be noted that some deviations from experimental data are exhibited by simulated results, especially for axial hysteresis loops in Figure 5.7(b) and Figure 5.8(b).

In order to further validate the proposed model capabilities under general loading conditions, 90° out-of-phase non-proportional axial-torsional cyclic experiments are utilized. This loading path is selected since no elastic unloading would take place upon strain/load reversal, thus, the stability of the developed plasticity algorithm would rigorously be scrutinized [168,184]. The simulated stabilized responses of three wrought Mg alloys during non-proportional cyclic tests are plotted in Figure 5.9, along with their actual responses from experiment. In general, agreement between model predictions and experimental results is satisfactory, bearing in mind the complexities associated with 90° out-of-phase loading path. In particular, continuous reversal points showing plastic unloading are well represented by the

proposed model. However, discrepancy between calculated and experimentally obtained results in Figure 5.9 is greater than that in the case of in-phase loading path (Figure 5.7 and Figure 5.8). This should be explored, in more details, in future studies to possibly introduce a means of including non-proportional effects.

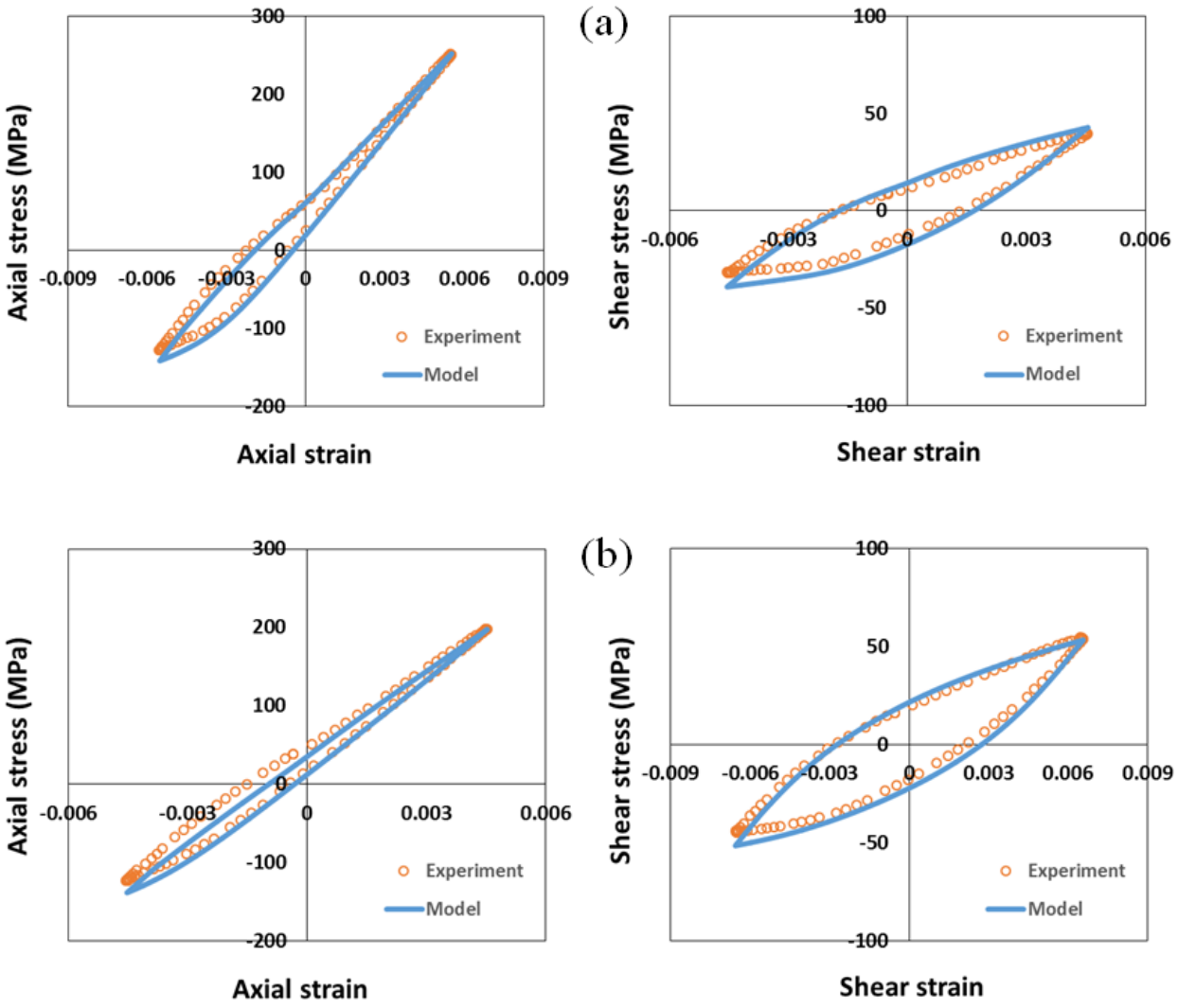

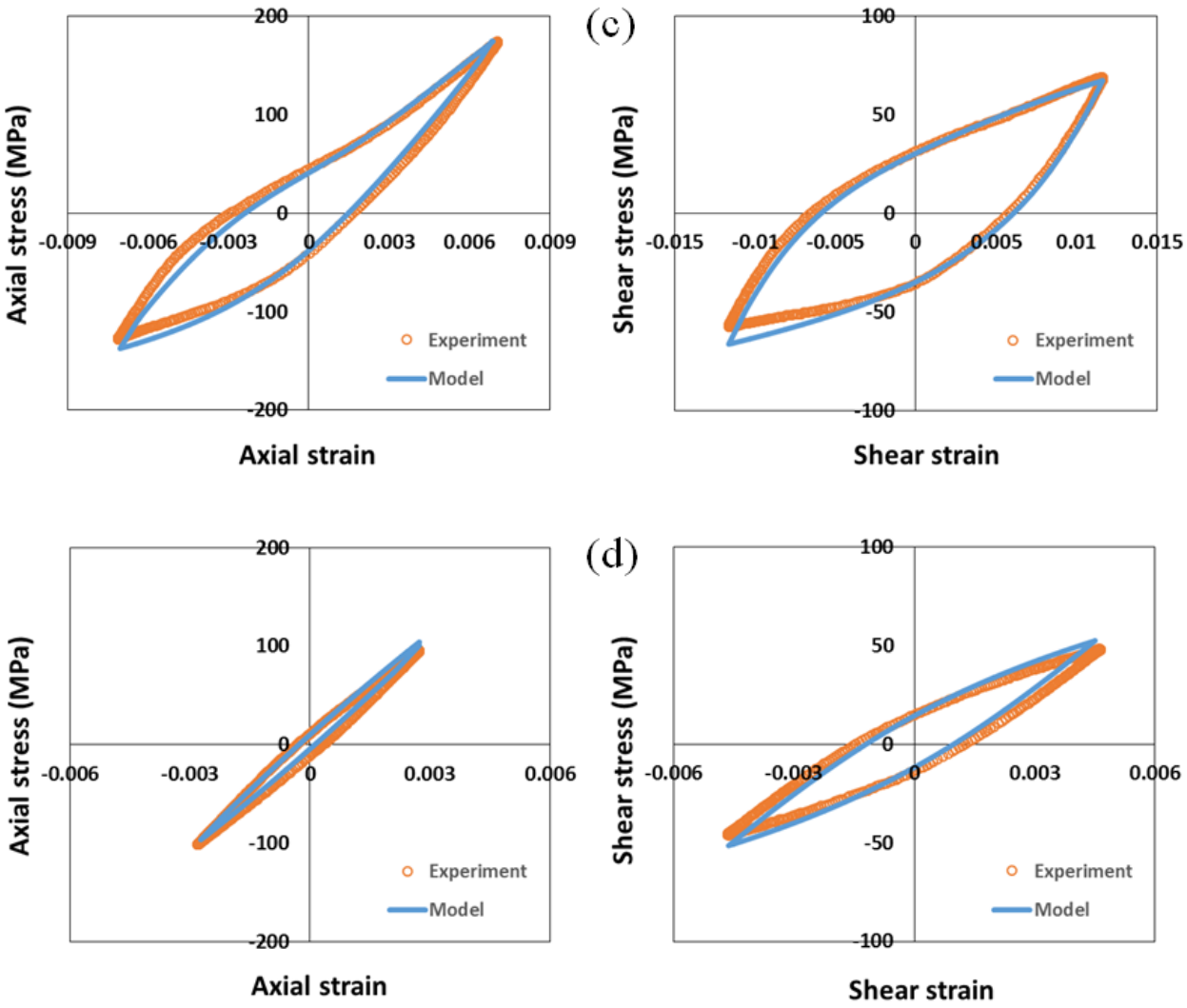

Figure 5.7 Experimental results vs. model predictions for proportional multiaxial cyclic tests on AZ31B [28]**: (a)** $\boldsymbol{\varepsilon_a = 0.55\%, \gamma_a = 0.45\%}$**, (b)** $\boldsymbol{\varepsilon_a = 0.45\%, \gamma_a = 0.65\%}$**, and AZ61A** [107]**: (c)** $\boldsymbol{\varepsilon_a = 0.70\%, \gamma_a = 1.16\%}$**, (c)** $\boldsymbol{\varepsilon_a = 0.27\%, \gamma_a = 0.46\%}$**.**

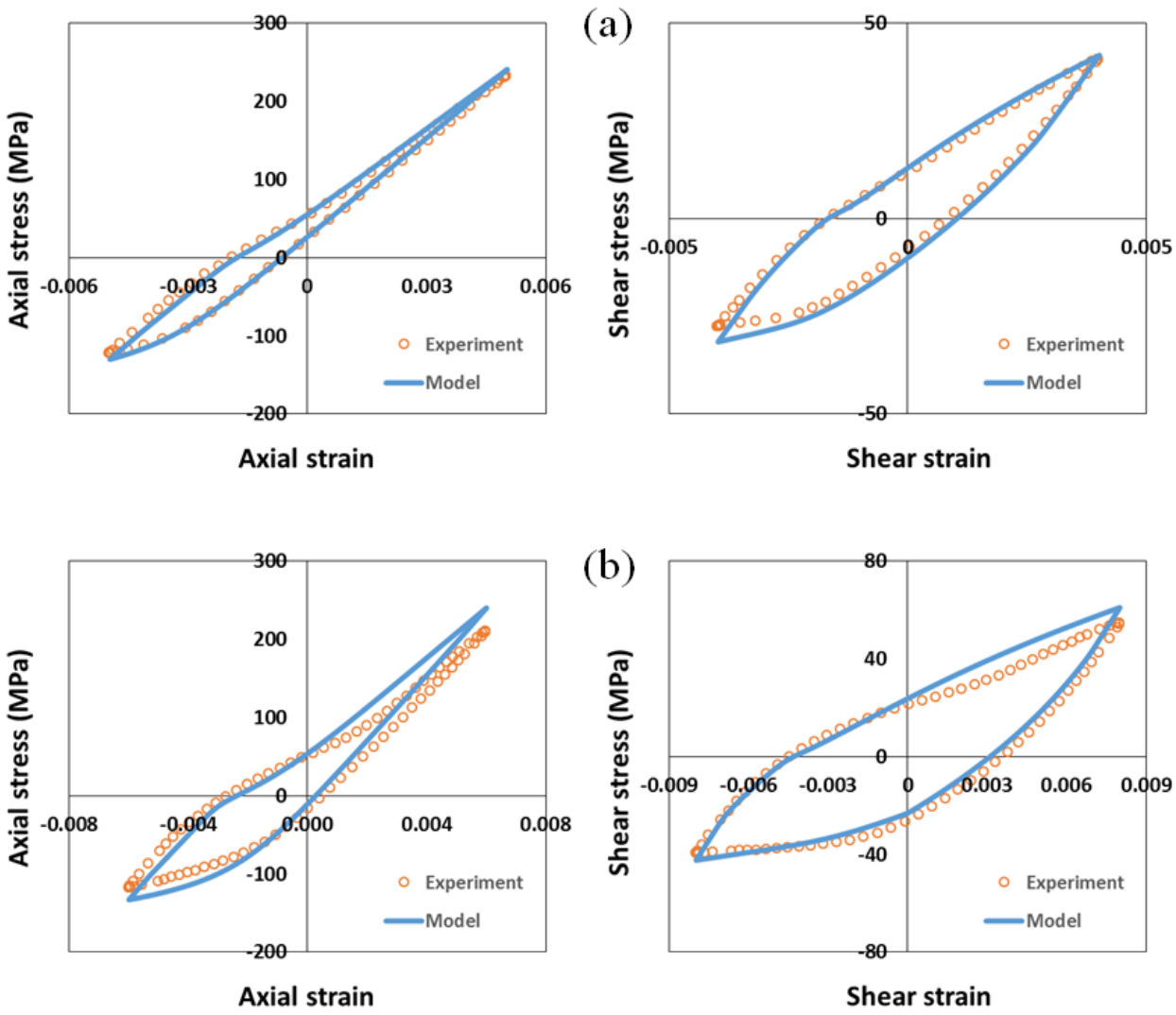

Figure 5.8 Experimental results vs. model predictions for proportional B-C tests on AM30 extrusion: (a) $\varepsilon_a = 0.50\%, \gamma_a = 0.40\%$, (b) $\varepsilon_a = 0.60\%, \gamma_a = 0.80\%$.

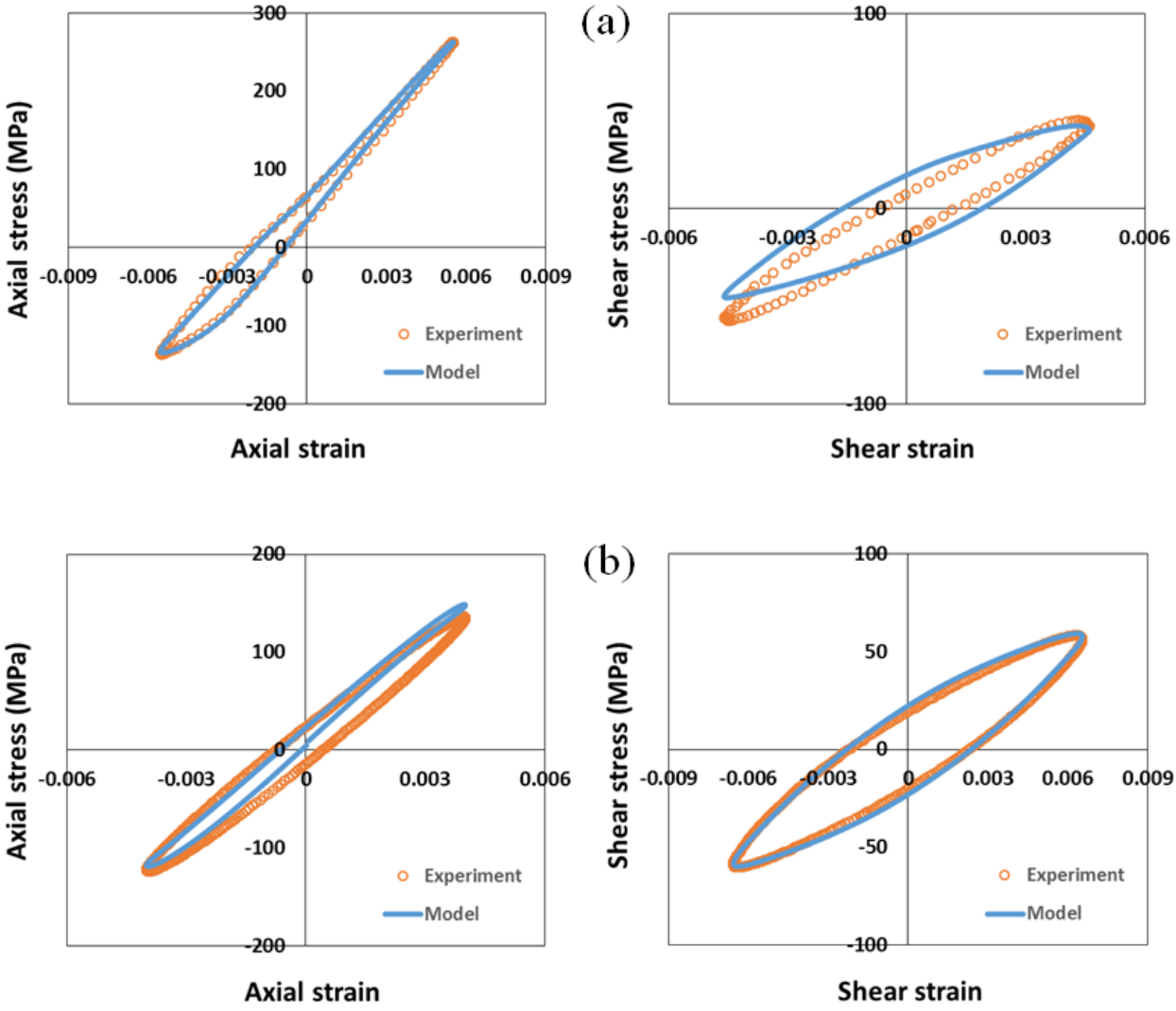
(a)
Axial stress (MPa)
300
200
100
0
-100
-200
-0.009
-0.006
-0.003
0
0.003
0.006
0.009
Experiment
Model
Axial strain
Shear stress (MPa)
100
0
-100
-0.006
-0.003
0
0.003
0.006
Experiment
Model
Shear strain
(b)
Axial stress (MPa)
200
100
0
-100
-200
-0.006
-0.003
0
0.003
0.006
Experiment
Model
Axial strain
Shear stress (MPa)
100
50
0
-50
-100
-0.009
-0.006
-0.003
0
0.003
0.006
0.009
Experiment
Model
Shear strain

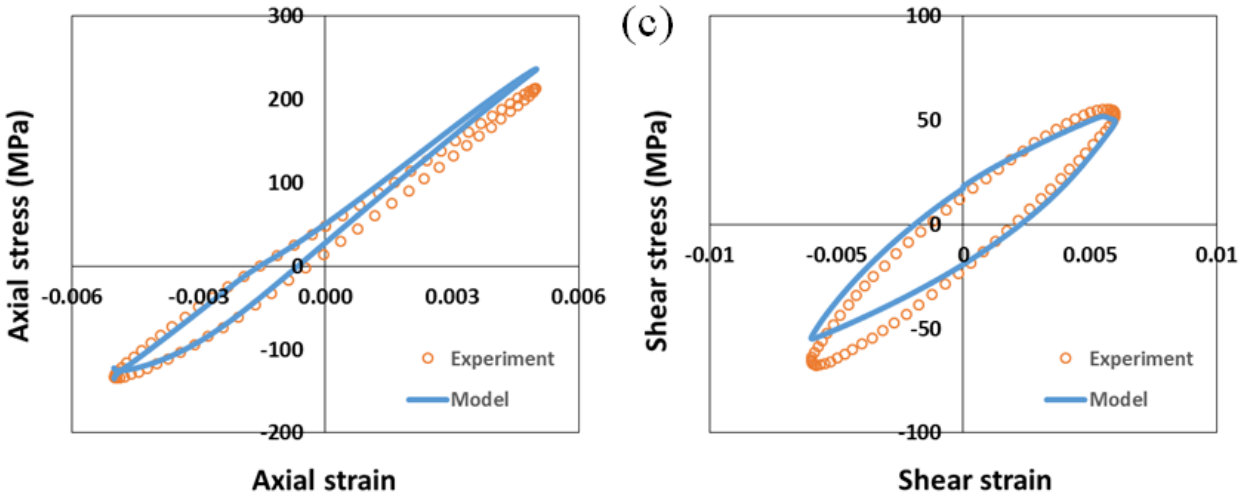

Figure 5.9 Experimental results vs. model predictions for non-proportional B-C tests on (a) AZ31B [28]**:** $\boldsymbol{\varepsilon_a = 0.55\%, \gamma_a = 0.46\%}$**, (b) AZ61A** [107]**:** $\boldsymbol{\varepsilon_a = 0.40\%, \gamma_a = 0.66\%}$**, and (c) AM30:** $\boldsymbol{\varepsilon_a = 0.50\%, \gamma_a = 0.60\%}$**.**

5.5.2.2 Notched plate loading-unloading

To conduct a component-level verification of the proposed model as well as the numerical algorithm coded into UMAT, a multi-element notched plate simulation is also carried out via Abaqus®/Standard. Fully integrated 20-node continuum quadratic brick elements (C3D20) are used in a partitioned region around the notch with the radius of four times notch radius. Specifying appropriate symmetry boundary conditions at the top and left sides of sketch in Figure 5.10, a quarter of the plate is modelled. Gross nominal pressure of $144\ MPa$ equivalent to the net nominal stress of $180\ MPa$ (90% of yield stress in tension) is applied along longitudinal direction coaxial with ED and then released.

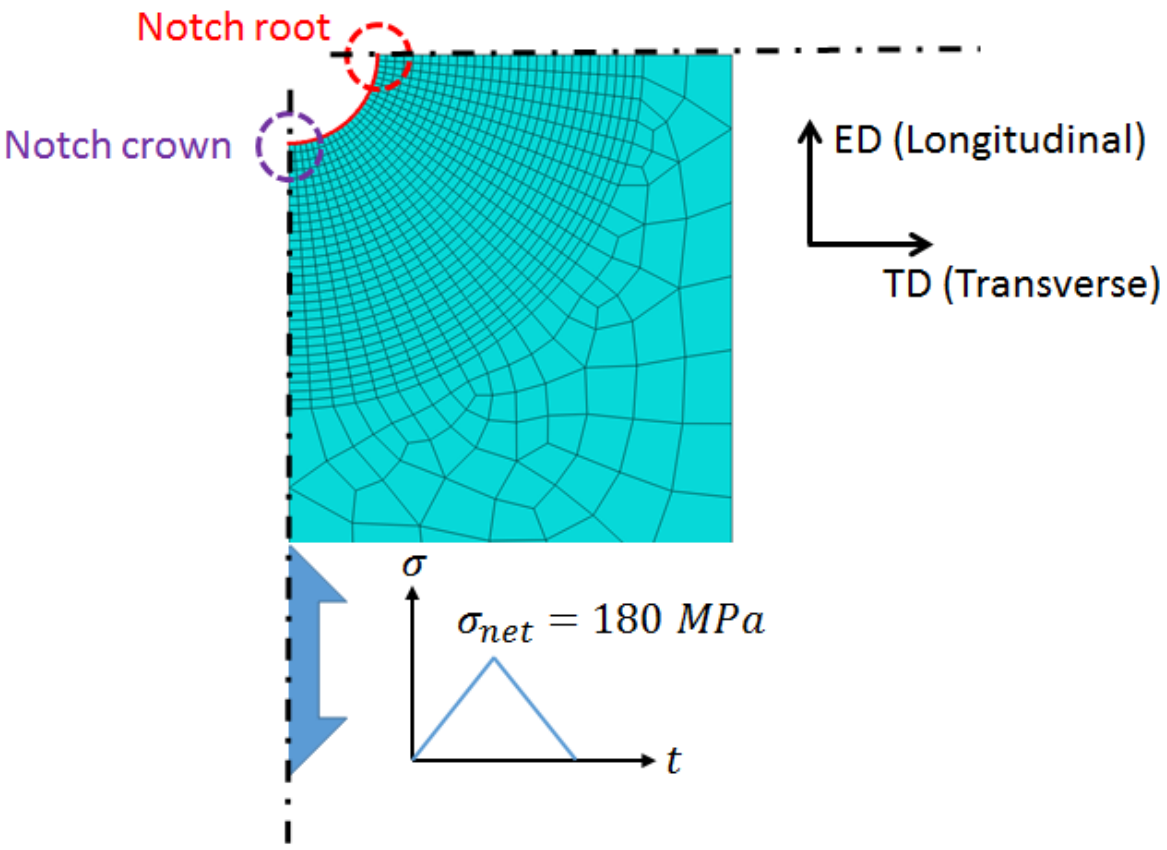

Figure 5.10 FE mesh of notched plate with quarter symmetry.

With the aim of finding the optimum number of elements in the region of interest, a mesh size study is performed by recording longitudinal strain value at a specific point, resulted from a number of preliminary simulations with varying element sizes. According to graph in Figure 5.11, having 7500 elements in notch vicinity will give a solution which is independent of element size.

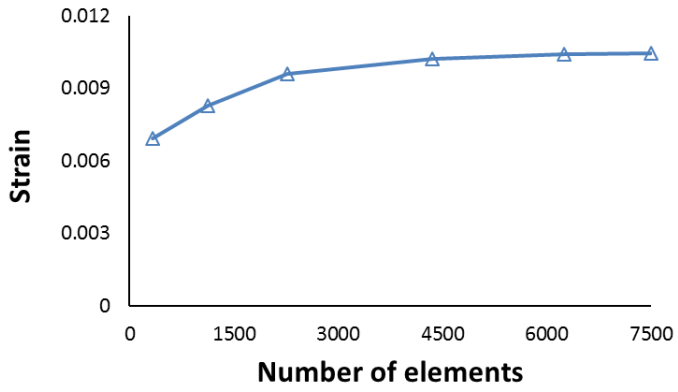

Figure 5.11 Mesh convergence study results.

Strain values from FE model, for comparison with measured values from experiment, are probed at the notch edge. To this end, a nodal path is defined around the notch, starting at notch root and ending to notch crown, as highlighted in Figure 5.10. Each node is labeled with its relative X-coordinate (horizontal distance from notch root), such that the nodes at notch root and notch crown are given $X = 0$ and $X = 3\,mm$, respectively. Figure 5.12 presents the variations of both longitudinal (ED) and transverse (TD) strain values around the notch, predicted by the proposed model at the end of loading as well as upon unloading. It is noticeable that maximum longitudinal and (absolute value of) transverse strains, and thereby, residual strains, do not happen at the notch root, but at node $X \cong 0.8\,mm$. This is confirmed by DIC measurements (see also Figure 5.13) and will be further discussed later. The maximum longitudinal strains at the end of loading are calculated and measured to be 0.0168 and 0.0164, respectively. The corresponding residual strain values from FEA and DIC are, respectively, 0.0094 and 0.0095. For comparison purposes, points around the notch are selected and their corresponding strain values at the end of loading and upon unloading, acquired from experiment

through DIC are superimposed on plots of Figure 5.12. The results show a good correlation of predictions with experimental measurements.

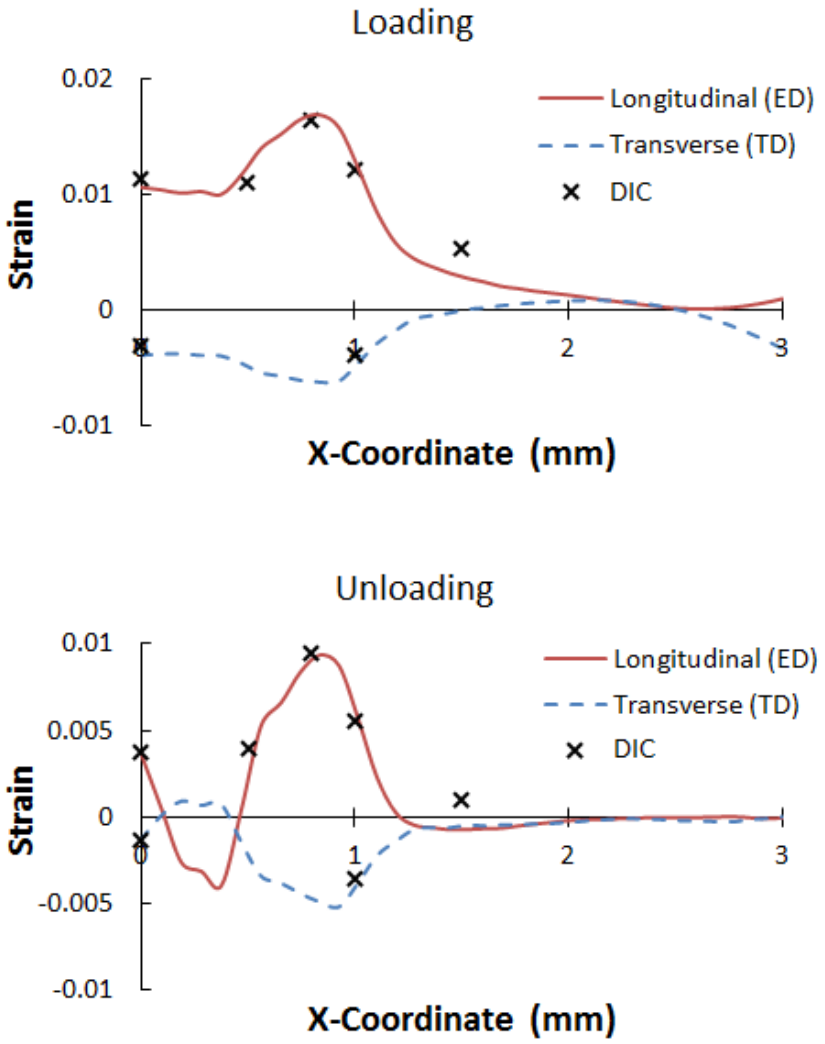

Figure 5.12 The variations of longitudinal (ED) and transverse (TD) strains calculated by FEA around the notch: (a) at the end of loading, and (b) upon unloading. DIC measurements are superimposed on both plots.

In Figure 5.13 the contour of longitudinal (ED) strain at the end of loading calculated by the proposed model via UMAT is qualitatively compared with the experimentally measured contour by DIC for AM30 extrusion notched plate. Note that colour spectrums for both contours are showing the same limits of strain. As can be seen, the prediction by the proposed plasticity model closely agrees with experimental strain field around the notch. Notably, strain hot spot is correctly captured to be away from the notch root.

To demonstrate the influence of including anisotropy in FE simulations of wrought magnesium alloys, second simulation is run, neglecting anisotropic behaviour of AM30 extrusion, and assigning ED properties to all axial directions. This means that in the plastic moduli matrix $[H]$, in Equation (5.34), H_{22}, and H_{33} components will be assumed equal to H_{11}. The longitudinal strain contour at the end of loading from isotropic simulation is illustrated in Figure 5.14. As expected, the result based on isotropic behaviour predicts the hot spot exactly at the notch root, which is obviously in contrast with experimental observation in Figure 5.13(b). Since fatigue cracks are most likely to initiate at hot spots, incorporating anisotropy into plasticity model appears to be of great importance in the fatigue analysis of components made of wrought magnesium alloys under cyclic loading.

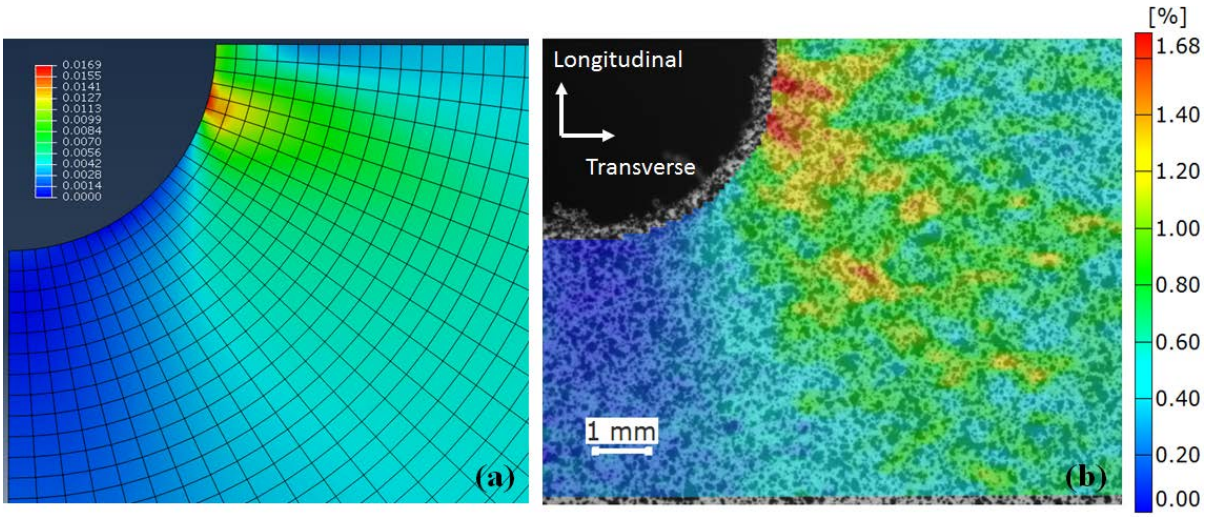

Figure 5.13 The longitudinal strain field at notch vicinity at the end of loading for AM30 notched plate: (a) calculated by FEA, and (b) measured by DIC.

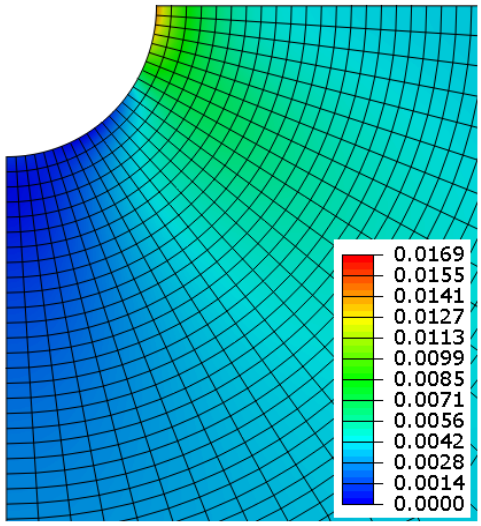

Figure 5.14 Longitudinal strain contour at the end of loading resulted from isotropic simulation.

5.5.3 Modelling considerations and next steps

In the proposed model, to abide by phenomenological plasticity framework, no explicit reference to the microstructural deformation mechanisms of wrought Mg alloys, i.e., slip, twinning, and de-twinning is made while developing corresponding constitutive relations. However, their incorporation into the model is implied through their macroscopic flow curve manifestation i.e., variations in experimental plastic moduli leading to changes in the concavity of flow curves.

The developed numerical algorithm incorporated into the UMAT, can be extended to assess the fatigue life of a load-bearing component under cyclic loading. To this end, a fatigue damage model such as Jahed-Varvani energy-based model [139], which uses axial and shear strain energy densities from corresponding stabilized hysteresis loops to estimate the fatigue life, can be integrated into the UMAT. It is worth mentioning that the capability of Jahed-Varvani model in the fatigue life assessment of AM30 Mg alloy extrusion under multiaxial loading has been confirmed by the authors [8].

In this research, the proposed anisotropic model has been calibrated and successfully verified using different properties of AM30 extrusion along different directions (i.e., ED and TD). In-depth validation of the model under triaxial loading conditions requires characterisation of AM30 extrusion along the third direction, i.e., normal direction (ND), which can be further explored in future.

5.6 **Conclusions**

Phenomenological plasticity technique has been exploited to develop a new constitutive cyclic plastic model for wrought magnesium alloys, capable of capturing their unique plastic flow features. An isotropic von Mises yield surface coupled with an anisotropic kinematic hardening rule based on Ziegler's rule constitute the essential elements of the proposed model. Following statements outline presented results and discussion:

- Key phenomenological concept in the proposed model is the plastic moduli matrix containing hardening or plastic moduli along different directions.
- Plastic moduli matrix embedded in the kinematic hardening rule can be independently calibrated along each axial/shear directions. Under multiaxial loading, material properties in directions along which, applied load has a non-zero component, will contribute to the overall plastic response of the material.
- The hardening rule accounts for the yield asymmetry of wrought Mg alloys by means of separate plastic modulus functions activating under tension/compression.
- An efficient and stable numerical algorithm is devised to implement the proposed model into MATLAB® code as well as UMAT to run with commercial FE software Abaqus®/Standard.
- Model predictions of stabilized hysteresis loops under in-phase and 90° out-of-phase biaxial axial-torsional loadings are conforming to experimental results for three different Mg alloy extrusions, namely, AZ31B, AZ61A, and AM30.

- Simulating a multi-element notched plate under tensile loading/unloading, predicted strain field around the notch is seen to be in excellent agreement with experimental measurements by DIC. In particular, the model promisingly predicts strain hot spot to be away from the notch root, which is validated by experimental observation.

Chapter 6

Recommendations for future works

In continuation of current research, the following subjects are recommended for further investigation:

1) To complement the direction-dependent fatigue and cyclic characterisation of wrought magnesium alloy under investigation (AM30 extrusion), experimental data along normal direction (ND) is also needed. This would make a worthwhile contribution to twin study, since extension twinning is expected to profusely happen during tension along ND. Furthermore, employing ND data, available fatigue damage models as well as the proposed cyclic plasticity model can comprehensively be verified.

2) Multiaxial cyclic and fatigue behaviour of AM30 extrusion has been investigated in present research by conducting biaxial axial-torsional cyclic experiments on tubular specimens. This subject can be further pursued through biaxial tension-compression tests on cruciform specimens. Biaxial tension-compression tests would also provide valuable experimental data for verifying the proposed cyclic plasticity model. In regard to specimen preparation, a cruciform specimen has been designed, in collaboration with University of Lisbon in Portugal, and machined from AM30 extrusion section with arms along ED and TD. The geometry and dimensions of the designed cruciform specimen for biaxial tension-compression experiments is depicted in Figure 6.1.

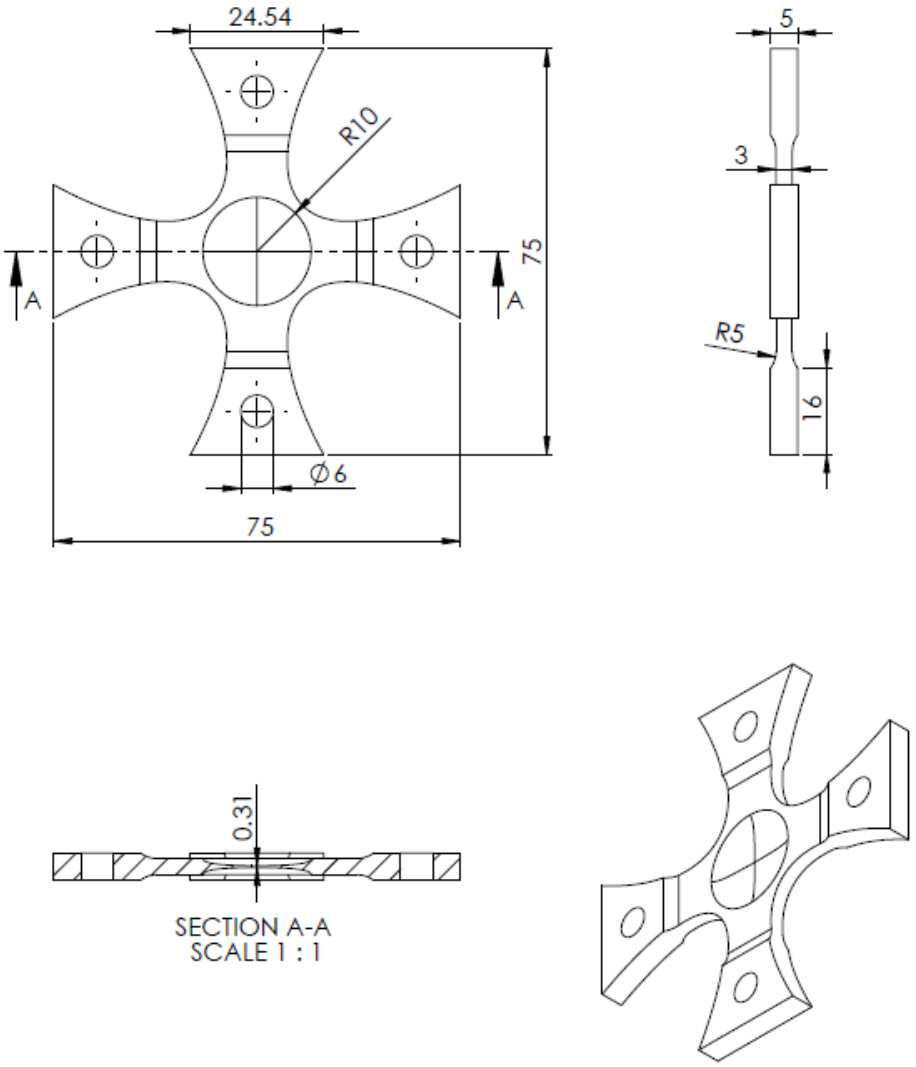

Figure 6.1 Geometry and dimensions (in *mm*) of cruciform specimen to be used for cyclic biaxial tension-compression tests.

3) The proposed cyclic plasticity model implemented in the UMAT code has been shown to successfully predict axial and shear stabilized hysteresis loops of wrought magnesium alloys under multiaxial loading condition. Incorporating a suitable fatigue damage criterion in the developed numerical procedure, will enable the model to be applied to fatigue analysis of a component to predict crack initiation life and location.

Bibliography

[1] H. Friedrich, S. Schumann, Research for a “new age of magnesium” in the automotive industry, Journal of Materials Processing Technology. 117 (2001) 276–281. doi:10.1016/S0924-0136(01)00780-4.

[2] D. Eliezer, E. Aghion, F.H. (Sam) Froes, Magnesium Science, Technology and Applications, Advanced Performance Materials. 5 (1998) 201–212. doi:10.1023/A:1008682415141.

[3] A.A. Luo, A.K. Sachdev, Development of a New Wrought Magnesium-Aluminum-Manganese Alloy AM30, Metallurgical and Materials Transactions A. 38 (2007) 1184–1192. doi:10.1007/s11661-007-9129-2.

[4] S. Begum, D.L. Chen, S. Xu, A.A. Luo, Strain-Controlled Low-Cycle Fatigue Properties of a Newly Developed Extruded Magnesium Alloy, Metallurgical and Materials Transactions A. 40 (2009) 255–255. doi:10.1007/s11661-008-9722-z.

[5] T.J. Luo, Y.S. Yang, W.H. Tong, Q.Q. Duan, X.G. Dong, Fatigue deformation characteristic of as-extruded AM30 magnesium alloy, Materials & Design. 31 (2010) 1617–1621. doi:10.1016/j.matdes.2009.08.042.

[6] M.K. Kulekci, Magnesium and its alloys applications in automotive industry, The International Journal of Advanced Manufacturing Technology. 39 (2008) 851–865. doi:10.1007/s00170-007-1279-2.

[7] A.A. Roostaei, H. Jahed, Role of loading direction on cyclic behaviour characteristics of AM30 extrusion and its fatigue damage modelling, Materials Science and Engineering: A. 670 (2016) 26–40. doi:10.1016/j.msea.2016.05.116.

[8] A.A. Roostaei, H. Jahed, Multiaxial cyclic behaviour and fatigue modelling of AM30 Mg alloy extrusion, International Journal of Fatigue. 97 (2017) 150–161. doi:10.1016/j.ijfatigue.2016.12.037.

[9] C. Bettles, M. Gibson, Current wrought magnesium alloys: Strengths and weaknesses, JOM. 57 (2005) 46–49. doi:10.1007/s11837-005-0095-0.

[10] E. Doege, K. Dröder, Sheet metal forming of magnesium wrought alloys — formability and process technology, Journal of Materials Processing Technology. 115 (2001) 14–19. doi:10.1016/S0924-0136(01)00760-9.

[11] M. Easton, W. Qian Song, T. Abbott, A comparison of the deformation of magnesium alloys with aluminium and steel in tension, bending and buckling, Materials & Design. 27 (2006) 935–946. doi:10.1016/j.matdes.2005.03.005.

[12] S.R. Agnew, J.W. Senn, J.A. Horton, Mg sheet metal forming: Lessons learned from deep drawing Li and Y solid-solution alloys, JOM. 58 (2006) 62–69. doi:10.1007/s11837-006-0026-8.

[13] S.R. Agnew, Ö. Duygulu, Plastic anisotropy and the role of non-basal slip in magnesium alloy AZ31B, International Journal of Plasticity. 21 (2005) 1161–1193. doi:10.1016/j.ijplas.2004.05.018.

[14] B.L. Mordike, T. Ebert, Magnesium Properties - applications - potential, Materials Science and Engineering A. 302 (2001) 37–45. doi:10.1016/S0921-5093(00)01351-4.

[15] C. Roberts, Magnesium and its alloys, Wiley, New York/London, 1996.

[16] S. Kleiner, P.. Uggowitzer, Mechanical anisotropy of extruded Mg–6% Al–1% Zn alloy, Materials Science and Engineering: A. 379 (2004) 258–263. doi:10.1016/j.msea.2004.02.020.

[17] J. Koike, T. Kobayashi, T. Mukai, H. Watanabe, M. Suzuki, K. Maruyama, et al., The activity of non-basal slip systems and dynamic recovery at room temperature in fine-grained AZ31B magnesium alloys, Acta Materialia. 51 (2003) 2055–2065. doi:10.1016/S1359-6454(03)00005-3.

[18] J. Koike, R. Ohyama, Geometrical criterion for the activation of prismatic slip in AZ61 Mg alloy sheets deformed at room temperature, Acta Materialia. 53 (2005) 1963–1972. doi:10.1016/j.actamat.2005.01.008.

[19] S.R. Agnew, M.H. Yoo, C.N. Tomé, Application of texture simulation to understanding mechanical behavior of Mg and solid solution alloys containing Li or Y, Acta Materialia. 49 (2001) 4277–4289. doi:10.1016/S1359-6454(01)00297-X.

[20] M.H. Yoo, J.R. Morris, K.M. Ho, S.R. Agnew, Nonbasal deformation modes of HCP metals and alloys: Role of dislocation source and mobility, Metallurgical and Materials Transactions A. 33 (2002) 813–822. doi:10.1007/s11661-002-1013-5.

[21] G.I. Taylor, Plastic strain in metals, Twenty-Eighth May Lecture to the Institute of Metals. 62 (1938) 307–325.

[22] X. LOU, M. LI, R. BOGER, S. AGNEW, R. WAGONER, Hardening evolution of AZ31B Mg sheet, International Journal of Plasticity. 23 (2007) 44–86. doi:10.1016/j.ijplas.2006.03.005.

[23] M.H. Yoo, Slip, twinning, and fracture in hexagonal close-packed metals, Metallurgical Transactions A. 12 (1981) 409–418. doi:10.1007/BF02648537.

[24] M. Gharghouri, G. Weatherly, J. Embury, J. Root, Study of the mechanical properties of Mg-7.7at.% Al by in-situ neutron diffraction, Philosophical Magazine A. 79 (1999) 1671–1695. doi:10.1080/01418619908210386.

[25] C. Cáceres, T. Sumitomo, M. Veidt, Pseudoelastic behaviour of cast magnesium AZ91 alloy under cyclic loading–unloading, Acta Materialia. 51 (2003) 6211–6218. doi:10.1016/S1359-6454(03)00444-0.

[26] J. Albinmousa, H. Jahed, S. Lambert, Cyclic axial and cyclic torsional behaviour of extruded AZ31B magnesium alloy, International Journal of Fatigue. 33 (2011) 1403–1416. doi:10.1016/j.ijfatigue.2011.04.012.

[27] J.H. Kim, D. Kim, Y.S. Lee, M.G. Lee, K. Chung, H.Y. Kim, et al., A temperature-dependent elasto-plastic constitutive model for magnesium alloy AZ31 sheets, International Journal of Plasticity. 50 (2013) 66–93. doi:10.1016/j.ijplas.2013.04.001.

[28] J. Al Bin Mousa, Multiaxial Fatigue Characterization and Modeling of AZ31B Magnesium Extrusion, University of Waterloo, 2011.

[29] H. Jahed, J. Albinmousa, Multiaxial behaviour of wrought magnesium alloys – A review and suitability of energy-based fatigue life model, Theoretical and Applied Fracture Mechanics. 73 (2014) 97–108. doi:10.1016/j.tafmec.2014.08.004.

[30] R.A. Lebensohn, C.N. Tomé, A self-consistent viscoplastic model: prediction of rolling textures of anisotropic polycrystals, Materials Science and Engineering: A. 175 (1994) 71–82. doi:10.1016/0921-5093(94)91047-2.

[31] R. Lebensohn, C. Tomé, A self-consistent anisotropic approach for the simulation of plastic deformation and texture development of polycrystals: application to zirconium alloys, Acta Metallurgica et Materialia. 41 (1993) 2611–2624.

[32] D. Steglich, Y. Jeong, M.O. Andar, T. Kuwabara, Biaxial deformation behaviour of AZ31 magnesium alloy: Crystal-plasticity-based prediction and experimental validation, International Journal of Solids and Structures. 49 (2012) 3551–3561. doi:10.1016/j.ijsolstr.2012.06.017.

[33] A. Staroselsky, L. Anand, A constitutive model for hcp materials deforming by slip and twinning: Application to magnesium alloy AZ31B, International Journal of Plasticity. 19 (2003) 1843–1864. doi:10.1016/S0749-6419(03)00039-1.

[34] K. Chung, T. Park, Consistency condition of isotropic–kinematic hardening of anisotropic yield functions with full isotropic hardening under monotonously proportional loading, International Journal of Plasticity. 45 (2013) 61–84. doi:10.1016/j.ijplas.2012.10.012.

[35] D. Banabic, F. Barlat, O. Cazacu, T. Kuwabara, Advances in anisotropy and formability, International Journal of Material Forming. 3 (2010) 165–189. doi:10.1007/s12289-010-0992-9.

[36] A. V. Hershey, The plasticity of an isotropic aggregate of anisotropic face-centered cubic crystals, Journal of Applied Mechanics. 21 (1954) 241–249.

[37] D. Drucker, Relation of experiments to mathematical theories of plasticity, Journal of Applied Mechanics. 16 (1949) 349–357.

[38] R. Hill, A Theory of the Yielding and Plastic Flow of Anisotropic Metals, Proceedings of the Royal Society of London A: Mathematical, Physical and Engineering Sciences. 193 (1948) 281–297. doi:10.1098/rspa.1948.0045.

[39] R. Hill, Constitutive modelling of orthotropic plasticity in sheet metals, Journal of the Mechanics and Physics of Solids. 38 (1990) 405–417.

[40] R. Hill, Theoretical plasticity of textured aggregates, Math. Proc. Cambridge Philos.

Soc. 85 (1979) 179–191.

[41] W. Hosford, A generalized isotropic yield criterion, Journal of Applied Mechanics Transactions of ASME. 39 (1972) 607–609.

[42] W. Hosford, Texture strengthening, Metals Eng Quart. 6 (1966) 13–19.

[43] C. Liu, Y. Huang, M.G. Stout, On the asymmetric yield surface of plastically orthotropic materials: A phenomenological study, Acta Materialia. 45 (1997) 2397–2406. doi:10.1016/S1359-6454(96)00349-7.

[44] O. Cazacu, F. Barlat, A criterion for description of anisotropy and yield differential effects in pressure-insensitive metals, International Journal of Plasticity. 20 (2004) 2027–2045. doi:10.1016/j.ijplas.2003.11.021.

[45] O. Cazacu, F. Barlat, Modeling Plastic Anistropy and Strength Differential Effects in Metallic Materials, in: O. Cazacu (Ed.), Multiscale Modeling of Heterogenous Materials: From Microstructure to Macro-Scale Properties, ISTE Ltd., London, UK, 2010. doi:10.1002/9780470611364.ch5.

[46] W. Hosford, T. Allen, Twinning and directional slip as a cause for a strength differential effect, Metallurgical and Materials Transactions B. 4 (1973) 1424–1425.

[47] O. Cazacu, F. Barlat, Generalization of Drucker's Yield Criterion to Orthotropy, Mathematics and Mechanics of Solids. 6 (2001) 613–630. doi:10.1177/108128650100600603.

[48] E. Kelley, W. Hosford, The deformation characteristics of textured magnesium, Transactions of the Metallurgical Society of AIME. 242 (1968) 654–660.

[49] O. Cazacu, B. Plunkett, F. Barlat, Orthotropic yield criterion for hexagonal closed packed metals, International Journal of Plasticity. 22 (2006) 1171–1194. doi:10.1016/j.ijplas.2005.06.001.

[50] B. Plunkett, O. Cazacu, F. Barlat, Orthotropic yield criteria for description of the anisotropy in tension and compression of sheet metals, International Journal of Plasticity. 24 (2008) 847–866. doi:10.1016/j.ijplas.2007.07.013.

[51] J.W. Yoon, Y. Lou, J. Yoon, M. V. Glazoff, Asymmetric yield function based on the stress invariants for pressure sensitive metals, International Journal of Plasticity. 56 (2014) 184–202. doi:10.1016/j.ijplas.2013.11.008.

[52] D. Ghaffari Tari, M.J. Worswick, U. Ali, M.A. Gharghouri, Mechanical response of AZ31B magnesium alloy: Experimental characterization and material modeling considering proportional loading at room temperature, International Journal of Plasticity. 55 (2014) 247–267. doi:10.1016/j.ijplas.2013.10.006.

[53] M.N. Mekonen, D. Steglich, J. Bohlen, D. Letzig, J. Mosler, Mechanical characterization and constitutive modeling of Mg alloy sheets, Materials Science & Engineering A. 540 (2012) 174–186. doi:10.1016/j.msea.2012.01.122.

[54] M.A. Khayamian, B. Behravesh, H. Jahed, Incorporation of asymmetric yield and hardening behaviour in axisymmetric elastoplastic problems, Materials & Design. 99 (2016) 490–499. doi:10.1016/j.matdes.2016.03.089.

[55] H. Jahed, R.N. Dubey, An Axisymmetric Method of Elastic-Plastic Analysis Capable of Predicting Residual Stress Field, Journal of Pressure Vessel Technology. 119 (1997) 264. doi:10.1115/1.2842303.

[56] H. Jahed, R. Sethuraman, R.N. Dubey, A variable material property approach for solving elastic-plastic problems, International Journal of Pressure Vessels and Piping. 71 (1997) 285–291. doi:10.1016/S0308-0161(96)00079-8.

[57] P. Tomlinson, H. Azizi-Alizamini, W.J. Poole, C.W. Sinclair, M.A. Gharghouri, Biaxial Deformation of the Magnesium Alloy AZ80, Metallurgical and Materials Transactions A. 44 (2013) 2970–2983. doi:10.1007/s11661-013-1707-x.

[58] E. Kalatehmollaei, H. Mahmoudi-Asl, H. Jahed, An asymmetric elastic–plastic analysis of the load-controlled rotating bending test and its application in the fatigue life estimation of wrought magnesium AZ31B, International Journal of Fatigue. 64 (2014) 33–41. doi:10.1016/j.ijfatigue.2014.02.012.

[59] B. Marzbanrad, E. Toyserkani, H. Jahed, Cyclic hysteresis of AZ31B extrusion under load-control tests using embedded sensor technology, Fatigue & Fracture of Engineering Materials & Structures. 40 (2017) 221–232. doi:10.1111/ffe.12488.

[60] W. Prager, The theory of plasticity: a survey of recent achievements, Proceedings of the Institution of Mechanical Engineers. 169 (1955) 41–57.

[61] R.T. Shield, H. Ziegler, On Prager's hardening rule, ZAMP Zeitschrift Für Angewandte Mathematik Und Physik. 9 (1958) 260–276. doi:10.1007/BF02033030.

[62] A. Khan, S. Huang, Continuum theory of plasticity, John Wiley & Sons, INC, New York, 1995.

[63] C. Frederick, P. Armstrong, A mathematical representation of the multiaxial Bauschinger effect, Materials at High Temperatures. 24 (2007) 1–26.

[64] J.L. Chaboche, Time-independent constitutive theories for cyclic plasticity, International Journal of Plasticity. 2 (1986) 149–188. doi:10.1016/0749-6419(86)90010-0.

[65] L. Geng, R.H. Wagoner, Role of plastic anisotropy and its evolution on springback, International Journal of Mechanical Sciences. 44 (2002) 123–148. doi:10.1016/S0020-7403(01)00085-6.

[66] B.K. Chun, J.T. Jinn, J.K. Lee, Modeling the Bauschinger effect for sheet metals, part I: theory, International Journal of Plasticity. 18 (2002) 571–595. doi:10.1016/S0749-6419(01)00046-8.

[67] B.K. Chun, H.Y. Kim, J.K. Lee, Modeling the Bauschinger effect for sheet metals, part II: applications, International Journal of Plasticity. 18 (2002) 597–616.

doi:10.1016/S0749-6419(01)00047-X.

[68] J.C. Moosbrugger, Anisotropic nonlinear kinematic hardening rule parameters from reversed proportional axial-torsional cycling, Trans. ASME: J. Engng Mater. Technol. 122 (2000) 18–28.

[69] M. Noban, J. Albinmousa, H. Jahed, S. Lambert, A Continuum-Based Cyclic Plasticity Model for AZ31B Magnesium Alloy under Proportional loading, Procedia Engineering. 10 (2011) 1366–1371. doi:10.1016/j.proeng.2011.04.227.

[70] M. Li, X.Y. Lou, J.H. Kim, R.H. Wagoner, An efficient constitutive model for room-temperature, low-rate plasticity of annealed Mg AZ31B sheet, International Journal of Plasticity. 26 (2010) 820–858. doi:10.1016/j.ijplas.2009.11.001.

[71] Z. Mróz, On the description of anisotropic work hardening, J. Mech. Phys. Solids. 15 (1967) 163–175.

[72] Z. Mróz, An attempt to describe the behavior of metals under cyclic loads using a more general workhardening model, Acta Mechanica. 7 (1969) 199–212. doi:10.1007/BF01176668.

[73] Y. Dafalias, E. Popov, Plastic internal variables formalism of cyclic plasticity, ASME, Transactions, Series E-Journal of Applied Mechanics. 98 (1976) 645–651.

[74] R. Krieg, A practical two surface plasticity theory, Journal of Applied Mechanics, ASME. 42 (1975) 641–646.

[75] M.-G. Lee, R.H. Wagoner, J.K. Lee, K. Chung, H.Y. Kim, Constitutive modeling for anisotropic/asymmetric hardening behavior of magnesium alloy sheets, International Journal of Plasticity. 24 (2008) 545–582. doi:10.1016/j.ijplas.2007.05.004.

[76] M. Lee, S. Kim, R. Wagoner, K. Chung, H. Kim, Constitutive modeling for anisotropic/asymmetric hardening behavior of magnesium alloy sheets: Application to sheet springback, International Journal of Plasticity. 25 (2009) 70–104. doi:10.1016/j.ijplas.2007.12.003.

[77] S.B. Behravesh, H. Jahed, S.B. Lambert, M. Chengji, Constitutive Modeling for Cyclic Behavior of AZ31B Magnesium Alloy and its Application, Advanced Materials Research. 891–892 (2014) 809–814. doi:10.4028/www.scientific.net/AMR.891-892.809.

[78] S. Behravesh, H. Jahed, S. Lambert, Cyclic Plasticity Constitutive Modelling of AZ31B, in: International Symposium of Plasticity, Freeport, Bahamas, 2014.

[79] S.B. Behravesh, Fatigue Characterization and Cyclic Plasticity Modeling of Magnesium Spot-Welds, University of Waterloo, 2013.

[80] N.T. Nguyen, M.G. Lee, J.H. Kim, H.Y. Kim, A practical constitutive model for AZ31B Mg alloy sheets with unusual stress-strain response, Finite Elements in Analysis and Design. 76 (2013) 39–49. doi:10.1016/j.finel.2013.08.008.

[81] W. Muhammad, M. Mohammadi, J. Kang, R.K. Mishra, K. Inal, An elasto-plastic constitutive model for evolving asymmetric/anisotropic hardening behavior of AZ31B and ZEK100 magnesium alloy sheets considering monotonic and reverse loading paths, International Journal of Plasticity. 70 (2015) 30–59. doi:10.1016/j.ijplas.2015.03.004.

[82] B. Plunkett, R.A. Lebensohn, O. Cazacu, F. Barlat, Anisotropic yield function of hexagonal materials taking into account texture development and anisotropic hardening, Acta Materialia. 54 (2006) 4159–4169. doi:10.1016/j.actamat.2006.05.009.

[83] F. Barlat, J.J. Gracio, M.G. Lee, E.F. Rauch, G. Vincze, An alternative to kinematic hardening in classical plasticity, International Journal of Plasticity. 27 (2011) 1309–1327. doi:10.1016/j.ijplas.2011.03.003.

[84] J. Lee, S.-J. Kim, Y.-S. Lee, J.-Y. Lee, D. Kim, M.-G. Lee, Distortional hardening concept for modeling anisotropic/asymmetric plastic behavior of AZ31B magnesium alloy sheets, International Journal of Plasticity. 94 (2017) 74–97. doi:10.1016/j.ijplas.2017.02.002.

[85] F. Mokdad, D.L. Chen, Cyclic deformation and anelastic behavior of ZEK100 magnesium alloy: Effect of strain ratio, Materials Science and Engineering: A. 640 (2015) 243–258. doi:10.1016/j.msea.2015.05.110.

[86] J. Albinmousa, H. Jahed, S. Lambert, Cyclic behaviour of wrought magnesium alloy under multiaxial load, International Journal of Fatigue. 33 (2011) 1127–1139. doi:10.1016/j.ijfatigue.2011.01.009.

[87] W. Yuan, R.S. Mishra, Grain size and texture effects on deformation behavior of AZ31 magnesium alloy, Materials Science and Engineering: A. 558 (2012) 716–724. doi:10.1016/j.msea.2012.08.080.

[88] S. Begum, D.L. Chen, S. Xu, A.A. Luo, Low cycle fatigue properties of an extruded AZ31 magnesium alloy, International Journal of Fatigue. 31 (2009) 726–735.

[89] Z. Bin Sajuri, Y. Miyashita, Y. Hosokai, Y. Mutoh, Effects of Mn content and texture on fatigue properties of as-cast and extruded AZ61 magnesium alloys, International Journal of Mechanical Sciences. 48 (2006) 198–209. doi:10.1016/j.ijmecsci.2005.09.003.

[90] S.H. Park, S.-G. Hong, J. Yoon, C.S. Lee, Influence of loading direction on the anisotropic fatigue properties of rolled magnesium alloy, International Journal of Fatigue. 87 (2016) 210–215. doi:10.1016/j.ijfatigue.2016.01.026.

[91] S.H. Park, S.-G. Hong, W. Bang, C.S. Lee, Effect of anisotropy on the low-cycle fatigue behavior of rolled AZ31 magnesium alloy, Materials Science and Engineering: A. 527 (2010) 417–423. doi:10.1016/j.msea.2009.08.044.

[92] F. Lv, F. Yang, Q.Q. Duan, Y.S. Yang, S.D. Wu, S.X. Li, et al., Fatigue properties of rolled magnesium alloy (AZ31) sheet: Influence of specimen orientation, International Journal of Fatigue. 33 (2011) 672–682. doi:10.1016/j.ijfatigue.2010.10.013.

[93] F. Lv, F. Yang, Q.Q. Duan, T.J. Luo, Y.S. Yang, S.X. Li, et al., Tensile and low-cycle fatigue properties of Mg–2.8% Al–1.1% Zn–0.4% Mn alloy along the transverse and rolling directions, Scripta Materialia. 61 (2009) 887–890. doi:10.1016/j.scriptamat.2009.07.023.

[94] J.B. Jordon, J.B. Gibson, M.F. Horstemeyer, H. El Kadiri, J.C. Baird, A.A. Luo, Effect of twinning, slip, and inclusions on the fatigue anisotropy of extrusion-textured AZ61 magnesium alloy, Materials Science and Engineering: A. 528 (2011) 6860–6871. doi:10.1016/j.msea.2011.05.047.

[95] S. Ishihara, Z. Nan, T. Goshima, Effect of microstructure on fatigue behavior of AZ31 magnesium alloy, Materials Science and Engineering: A. 468–470 (2007) 214–222. doi:10.1016/j.msea.2006.09.124.

[96] S. Ishihara, S. Taneguchi, H. Shibata, T. Goshima, A. Saiki, Anisotropy of the fatigue behavior of extruded and rolled magnesium alloys, International Journal of Fatigue. 50 (2013) 94–100. doi:10.1016/j.ijfatigue.2012.02.011.

[97] Y.C. Lin, X.-M. Chen, Z.-H. Liu, J. Chen, Investigation of uniaxial low-cycle fatigue failure behavior of hot-rolled AZ91 magnesium alloy, International Journal of Fatigue. 48 (2013) 122–132. doi:10.1016/j.ijfatigue.2012.10.010.

[98] X.M. Chen, Y.C. Lin, J. Chen, Low-cycle fatigue behaviors of hot-rolled AZ91 magnesium alloy under asymmetrical stress-controlled cyclic loadings, Journal of Alloys and Compounds. 579 (2013) 540–548. doi:10.1016/j.jallcom.2013.07.049.

[99] J.B. Jordon, H.R. Brown, H. El Kadiri, H.M. Kistler, R.L. Lett, J.C. Baird, et al., Investigation of fatigue anisotropy in an extruded magnesium alloy, International Journal of Fatigue. 51 (2013) 8–14. doi:10.1016/j.ijfatigue.2013.01.006.

[100] C.L. Fan, D.L. Chen, A.A. Luo, Dependence of the distribution of deformation twins on strain amplitudes in an extruded magnesium alloy after cyclic deformation, Materials Science and Engineering: A. 519 (2009) 38–45. doi:10.1016/j.msea.2009.04.048.

[101] J. Albinmousa, A. Pascu, H. Jahed, M.F. Horstemeyer, A. Luo, D. Chen, et al., Monotonic and Fatigue Behavior of Magnesium Extrusion Alloy AM30: An International Benchmark Test in the “Magnesium Front End Research and Development Project,” in: SAE Technical Paper 2010-01-0407, 2010. doi:10.4271/2010-01-0407.

[102] M. Lugo, J.B. Jordon, J. Bernard, M. Horstemeyer, Microstructure-Sensitive Fatigue Modeling of an Extruded AM30 Magnesium Alloy, in: SAE Technical Paper 2013-01-0980, 2013. doi:10.4271/2013-01-0980.

[103] A. Akhtar, E. Teghtsoonian, Solid solution strengthening of magnesium single crystals—ii the effect of solute on the ease of prismatic slip, Acta Metallurgica. 17 (1969) 1351–1356. doi:10.1016/0001-6160(69)90152-7.

[104] C.H. Cáceres, D.M. Rovera, Solid solution strengthening in concentrated Mg–Al alloys, Journal of Light Metals. 1 (2001) 151–156. doi:10.1016/S1471-5317(01)00008-6.

[105] Z. Keshavarz, M.R. Barnett, EBSD analysis of deformation modes in Mg–3Al–1Zn, Scripta Materialia. 55 (2006) 915–918. doi:10.1016/j.scriptamat.2006.07.036.

[106] Y. Xiong, Q. Yu, Y. Jiang, Multiaxial fatigue of extruded AZ31B magnesium alloy, Materials Science and Engineering A. 546 (2012) 119–128. doi:10.1016/j.msea.2012.03.039.

[107] J. Zhang, Q. Yu, Y. Jiang, Q. Li, An experimental study of cyclic deformation of extruded AZ61A magnesium alloy, International Journal of Plasticity. 27 (2011) 768–787. doi:10.1016/j.ijplas.2010.09.004.

[108] L. Wu, A. Jain, D.W. Brown, G.M. Stoica, S.R. Agnew, B. Clausen, et al., Twinning–detwinning behavior during the strain-controlled low-cycle fatigue testing of a wrought magnesium alloy, ZK60A, Acta Materialia. 56 (2008) 688–695. doi:10.1016/j.actamat.2007.10.030.

[109] Q. Yu, J. Zhang, Y. Jiang, Fatigue damage development in pure polycrystalline magnesium under cyclic tension–compression loading, Materials Science and Engineering: A. 528 (2011) 7816–7826. doi:10.1016/j.msea.2011.06.064.

[110] X.Z. Lin, D.L. Chen, Strain controlled cyclic deformation behavior of an extruded magnesium alloy, Materials Science and Engineering: A. 496 (2008) 106–113. doi:10.1016/j.msea.2008.05.016.

[111] S. AGNEW, D. BROWN, C. TOME, Validating a polycrystal model for the elastoplastic response of magnesium alloy AZ31 using in situ neutron diffraction, Acta Materialia. 54 (2006) 4841–4852. doi:10.1016/j.actamat.2006.06.020.

[112] L. Jiang, J.J. Jonas, R.K. Mishra, A.A. Luo, A.K. Sachdev, S. Godet, Twinning and texture development in two Mg alloys subjected to loading along three different strain paths, Acta Materialia. 55 (2007) 3899–3910. doi:10.1016/j.actamat.2007.03.006.

[113] L. Jiang, J.J. Jonas, A.A. Luo, A.K. Sachdev, S. Godet, Twinning-induced softening in polycrystalline AM30 Mg alloy at moderate temperatures, Scripta Materialia. 54 (2006) 771–775. doi:10.1016/j.scriptamat.2005.11.029.

[114] M. Niewczas, Lattice correspondence during twinning in hexagonal close-packed crystals, Acta Materialia. 58 (2010) 5848–5857. doi:10.1016/j.actamat.2010.06.059.

[115] F. Wang, S.R. Agnew, Dislocation transmutation by tension twinning in magnesium alloy AZ31, International Journal of Plasticity. 81 (2016) 63–86. doi:10.1016/j.ijplas.2016.01.012.

[116] H. El Kadiri, C.D. Barrett, J. Wang, C.N. Tomé, Why are $\{10\bar{1}2\}$ twins profuse in magnesium?, Acta Materialia. 85 (2015) 354–361. doi:10.1016/j.actamat.2014.11.033.

[117] Y. Chino, K. Kimura, M. Hakamada, M. Mabuchi, Mechanical anisotropy due to twinning in an extruded AZ31 Mg alloy, Materials Science and Engineering: A. 485

(2008) 311–317. doi:10.1016/j.msea.2007.07.076.

[118] D. Sarker, D.L. Chen, Dependence of compressive deformation on pre-strain and loading direction in an extruded magnesium alloy: Texture, twinning and de-twinning, Materials Science and Engineering: A. 596 (2014) 134–144. doi:10.1016/j.msea.2013.12.038.

[119] D. Sarker, J. Friedman, D.L. Chen, Influence of pre-strain on de-twinning activity in an extruded AM30 magnesium alloy, Materials Science and Engineering: A. 605 (2014) 73–79. doi:10.1016/j.msea.2014.03.046.

[120] D. Sarker, D.L. Chen, Texture transformation in an extruded magnesium alloy under pressure, Materials Science and Engineering: A. 582 (2013) 63–67. doi:10.1016/j.msea.2013.06.048.

[121] S. Begum, D.L. Chen, S. Xu, A.A. Luo, Effect of strain ratio and strain rate on low cycle fatigue behavior of AZ31 wrought magnesium alloy, Materials Science and Engineering: A. 517 (2009) 334–343. doi:10.1016/j.msea.2009.04.051.

[122] L. Wu, S.R. Agnew, D.W. Brown, G.M. Stoica, B. Clausen, A. Jain, et al., Internal stress relaxation and load redistribution during the twining-detwinning dominated cyclic deformation of a wrought magnesium alloy, Acta Mater. 56 (2008) 3699–3707.

[123] U. Essmann, U. Gösele, H. Mughrabi, A model of extrusions and intrusions in fatigued metals I. Point-defect production and the growth of extrusions, Philosophical Magazine A. 44 (1981) 405–426. doi:10.1080/01418618108239541.

[124] H. Mughrabi, R. Wang, K. Differt, U. Essmann, Fatigue Crack Initiation by Cyclic Slip Irreversibilities in High-Cycle Fatigue, Fatigue Mechanisms: Advances in Quantitative Measurement of Physical Damage, ASTM STP 811, J. Lankford, D. L. Davidson, W. L. Morris, and R. P. Wei, Eds., American Society for Testing and Materials. (1983) 5–45.

[125] A. Galiyev, R. Kaibyshev, G. Gottstein, Correlation of plastic deformation and dynamic recrystallization in magnesium alloy ZK60, Acta Materialia. 49 (2001) 1199–1207. doi:10.1016/S1359-6454(01)00020-9.

[126] K. Gall, G. Biallas, H.J. Maier, P. Gullett, M.F. Horstemeyer, D.L. McDowell, In-situ observations of low-cycle fatigue damage in cast AM60B magnesium in an environmental scanning electron microscope, Metallurgical and Materials Transactions A. 35 (2004) 321–331. doi:10.1007/s11661-004-0133-5.

[127] K. Gall, G. Biallas, H.J. Maier, P. Gullett, M.F. Horstemeyer, D.L. McDowell, et al., In-situ observations of high cycle fatigue mechanisms in cast AM60B magnesium in vacuum and water vapor environments, International Journal of Fatigue. 26 (2004) 59–70. doi:10.1016/S0142-1123(03)00079-3.

[128] G. Murugan, K. Raghukandan, U.T.S. Pillai, B.C. Pai, K. Mahadevan, High cyclic fatigue characteristics of gravity cast AZ91 magnesium alloy subjected to transverse

load, Materials & Design. 30 (2009) 2636–2641. doi:10.1016/j.matdes.2008.10.032.

[129] F. Wang, J. Dong, M. Feng, J. Sun, W. Ding, Y. Jiang, A study of fatigue damage development in extruded Mg–Gd–Y magnesium alloy, Materials Science and Engineering: A. 589 (2014) 209–216. doi:10.1016/j.msea.2013.09.089.

[130] Y. Xiong, Y. Jiang, Fatigue of ZK60 magnesium alloy under uniaxial loading, International Journal of Fatigue. 64 (2014) 74–83. doi:10.1016/j.ijfatigue.2014.02.019.

[131] D.L. Chen, A.R. Emami, A.A. Luo, Cyclic deformation of extruded AM30 magnesium alloy in the transverse direction, Journal of Physics: Conference Series. 240 (2010) 12048. doi:10.1088/1742-6596/240/1/012048.

[132] J.D. Bernard, J.B. Jordon, M.F. Horstemeyer, H. El Kadiri, J. Baird, D. Lamb, et al., Structure–property relations of cyclic damage in a wrought magnesium alloy, Scripta Materialia. 63 (2010) 751–756. doi:10.1016/j.scriptamat.2010.05.048.

[133] W. Song, H.J. Martin, A. Hicks, D. Seely, C.A. Walton, W.B. Lawrimore II, et al., Corrosion behaviour of extruded AM30 magnesium alloy under salt-spray and immersion environments, Corrosion Science. 78 (2014) 353–368. doi:10.1016/j.corsci.2013.10.020.

[134] Y. Xiong, Q. Yu, Y. Jiang, An experimental study of cyclic plastic deformation of extruded ZK60 magnesium alloy under uniaxial loading at room temperature, International Journal of Plasticity. 53 (2014) 107–124. doi:10.1016/j.ijplas.2013.07.008.

[135] J. Albinmousa, H. Jahed, Multiaxial effects on LCF behaviour and fatigue failure of AZ31B magnesium extrusion, International Journal of Fatigue. 67 (2014) 103–116. doi:10.1016/j.ijfatigue.2014.01.025.

[136] Y.C. Lin, Z.-H. Liu, X.-M. Chen, J. Chen, Stress-based fatigue life prediction models for AZ31B magnesium alloy under single-step and multi-step asymmetric stress-controlled cyclic loadings, Computational Materials Science. 73 (2013) 128–138. doi:10.1016/j.commatsci.2013.02.023.

[137] D.F. Socie, Multiaxial Fatigue Damage Models, Journal of Engineering Materials And Technology-Transactions Of The ASME. 109 (1987) 293–298.

[138] R.N. Smith, P. Watson, T.H. Topper, A Stress Strain Function for the Fatigue of Metals, J. of Materials JMLSA. 5 (1970) 767–778.

[139] H. Jahed, A. Varvani-Farahani, Upper and lower fatigue life limits model using energy-based fatigue properties, International Journal of Fatigue. 28 (2006) 467–473. doi:10.1016/j.ijfatigue.2005.07.039.

[140] K. Golos, F. Ellyin, A Total Strain Energy Density Theory for Cumulative Fatigue Damage, Journal of Pressure Vessel Technology. 110 (1988) 36–41. doi:10.1115/1.3226012.

[141] S. Bentachfine, G. Pluvinage, L.S. Toth, Z. Azari, Biaxial low cycle fatigue under non-

proportional loading of a magnesium-lithium alloy, Engineering Fracture Mechanics. 54 (1996) 513–522. doi:10.1016/0013-7944(95)00223-5.

[142] Q. Yu, J. Zhang, Y. Jiang, Q. Li, Multiaxial fatigue of extruded AZ61A magnesium alloy, International Journal of Fatigue. 33 (2011) 437–447. doi:10.1016/j.ijfatigue.2010.09.020.

[143] F. Castro, Y. Jiang, Fatigue life and early cracking predictions of extruded AZ31B magnesium alloy using critical plane approaches, International Journal of Fatigue. 88 (2016) 236–246. doi:10.1016/j.ijfatigue.2016.04.002.

[144] H. Li, G. Kang, Y. Liu, H. Jiang, Non-proportionally multiaxial cyclic deformation of AZ31 magnesium alloy: Experimental observations, Materials Science and Engineering: A. 671 (2016) 70–81. doi:10.1016/j.msea.2016.06.043.

[145] C.M. Sonsino, Influence of material's ductility and local deformation mode on multiaxial fatigue response, International Journal of Fatigue. 33 (2011) 930–947. doi:10.1016/j.ijfatigue.2011.01.010.

[146] D.W. Brown, S.R. Agnew, M.A.M. Bourke, T.M. Holden, S.C. Vogel, C.N. Tomé, Internal strain and texture evolution during deformation twinning in magnesium, Materials Science and Engineering: A. 399 (2005) 1–12. doi:10.1016/j.msea.2005.02.016.

[147] W. Wu, P.K. Liaw, K. An, Unraveling cyclic deformation mechanisms of a rolled magnesium alloy using in situ neutron diffraction, Acta Materialia. 85 (2015) 343–353. doi:10.1016/j.actamat.2014.11.030.

[148] A. Fatemi, D.F. Socie, A Critical Plane Approach To Multiaxial Fatigue Damage Including Out-of-Phase Loading, Fatigue & Fracture of Engineering Materials and Structures. 11 (1988) 149–165. doi:10.1111/j.1460-2695.1988.tb01169.x.

[149] M. Noban, H. Jahed, E. Ibrahim, A. Ince, Load path sensitivity and fatigue life estimation of 30CrNiMo8HH, International Journal of Fatigue. 37 (2012) 123–133. doi:10.1016/j.ijfatigue.2011.10.009.

[150] Y. Jiang, O. Hertel, M. Vormwald, An experimental evaluation of three critical plane multiaxial fatigue criteria, International Journal of Fatigue. 29 (2007) 1490–1502. doi:10.1016/j.ijfatigue.2006.10.028.

[151] B.-R. You, S.-B. Lee, A critical review on multiaxial fatigue assessments of metals, International Journal of Fatigue. 18 (1996) 235–244. doi:10.1016/0142-1123(96)00002-3.

[152] K. Liu, A Method Based on Virtual Strain-Energy Parameters for Multiaxial Fatigue Life Prediction, in: D.L. McDowell, J. Ellis (Eds.), Advances in Multiaxial Fatigue, ASTM International, 100 Barr Harbor Drive, PO Box C700, West Conshohocken, PA 19428-2959, 1993: pp. 67-67–18. doi:10.1520/STP24796S.

[153] A. Gryguc, S.K. Shaha, S.B. Behravesh, H. Jahed, M. Wells, B. Williams, et al.,

Monotonic and cyclic behaviour of cast and cast-forged AZ80 Mg, International Journal of Fatigue. (2017). doi:10.1016/j.ijfatigue.2017.06.038.

[154] M. Noban, H. Jahed, A. Varvani-Farahani, The choice of cyclic plasticity models in fatigue life assessment of 304 and 1045 steel alloys based on the critical plane-energy fatigue damage approach, International Journal of Fatigue. 43 (2012) 217–225. doi:10.1016/j.ijfatigue.2012.03.014.

[155] M.W. Brown, K.J. Miller, A theory for fatigue failure under multiaxial stress–strain conditions, Proceedings of the Institution of Mechanical Engineers 1847-1982 (Vols 1-196). 187 (1973) 745–755. doi:10.1243/PIME_PROC_1973_187_161_02.

[156] D.F. Socie, G.B. Marquis, Multiaxial Fatigue, SAE International, Warrendale, Pa, 2000.

[157] Y. Jiang, H. Sehitoglu, Fatigue and stress analysis of rolling contact, College of Engineering, University of Illinois at Urbana-Champaign. Rep no.161 (1992).

[158] F. Ellyin, K. Golos, Z. Xia, In-Phase and Out-of-Phase Multiaxial Fatigue, Journal of Engineering Materials and Technology. 113 (1991) 112. doi:10.1115/1.2903365.

[159] H. Jahed, A. Varvani-Farahani, M. Noban, I. Khalaji, An energy-based fatigue life assessment model for various metallic materials under proportional and non-proportional loading conditions, International Journal of Fatigue. 29 (2007) 647–655. doi:10.1016/j.ijfatigue.2006.07.017.

[160] S. Graff, W. Brocks, D. Steglich, Yielding of magnesium: From single crystal to polycrystalline aggregates, International Journal of Plasticity. 23 (2007) 1957–1978. doi:10.1016/j.ijplas.2007.07.009.

[161] G. Zhou, M.K. Jain, P. Wu, Y. Shao, D. Li, Y. Peng, Experiment and crystal plasticity analysis on plastic deformation of AZ31B Mg alloy sheet under intermediate temperatures: How deformation mechanisms evolve, International Journal of Plasticity. 79 (2016) 19–47. doi:10.1016/j.ijplas.2015.12.006.

[162] J. Lévesque, K. Inal, K.W. Neale, R.K. Mishra, Numerical modeling of formability of extruded magnesium alloy tubes, International Journal of Plasticity. 26 (2010) 65–83. doi:10.1016/j.ijplas.2009.05.001.

[163] A. Styczynski, C. Hartig, J. Bohlen, D. Letzig, Cold rolling textures in AZ31 wrought magnesium alloy, Scripta Materialia. 50 (2004) 943–947. doi:10.1016/j.scriptamat.2004.01.010.

[164] G. Proust, C.N. Tomé, A. Jain, S.R. Agnew, Modeling the effect of twinning and detwinning during strain-path changes of magnesium alloy AZ31, International Journal of Plasticity. 25 (2009) 861–880. doi:10.1016/j.ijplas.2008.05.005.

[165] T. Hama, H. Takuda, Crystal-plasticity finite-element analysis of inelastic behavior during unloading in a magnesium alloy sheet, International Journal of Plasticity. 27 (2011) 1072–1092. doi:10.1016/j.ijplas.2010.11.004.

[166] F. Dunne, N. Petrinic, Introduction to Computational Plasticity, Oxford University Press Inc., New York, USA, 2006. doi:10.1088/0305-4470/39/14/B02.

[167] F. Barlat, D.J. Lege, J.C. Brem, A six-component yield function for anisotropic materials, International Journal of Plasticity. 7 (1991) 693–712. doi:10.1016/0749-6419(91)90052-Z.

[168] Y. Jiang, P. Kurath, Characteristics of the Armstrong-Frederick type plasticity models, International Journal of Plasticity. 12 (1996) 387–415. doi:10.1016/S0749-6419(96)00013-7.

[169] M. Ardeljan, I.J. Beyerlein, B.A. McWilliams, M. Knezevic, Strain rate and temperature sensitive multi-level crystal plasticity model for large plastic deformation behavior: Application to AZ31 magnesium alloy, International Journal of Plasticity. 83 (2016) 90–109. doi:10.1016/j.ijplas.2016.04.005.

[170] M. Knezevic, A. Levinson, R. Harris, R.K. Mishra, R.D. Doherty, S.R. Kalidindi, Deformation twinning in AZ31: Influence on strain hardening and texture evolution, Acta Materialia. 58 (2010) 6230–6242. doi:10.1016/j.actamat.2010.07.041.

[171] J. Casey, H. Jahedmotlagh, The strength-differential effect in plasticity, International Journal of Solids and Structures. 20 (1984) 377–393. doi:10.1016/0020-7683(84)90047-7.

[172] J.P. Nobre, U. Noster, M. Kornmeier, a. M. Dias, B. Scholtes, Deformation Asymmetry of AZ31 Wrought Magnesium Alloy, Key Engineering Materials. 230–232 (2002) 267–270. doi:10.4028/www.scientific.net/KEM.230-232.267.

[173] S. Dong, Q. Yu, Y. Jiang, J. Dong, F. Wang, L. Jin, et al., Characteristic cyclic plastic deformation in ZK60 magnesium alloy, International Journal of Plasticity. (2017) 1–23. doi:10.1016/j.ijplas.2017.01.005.

[174] K. Hashiguchi, Constitutive Equations of Elastoplastic Materials With Anisotropic Hardening and Elastic-Plastic Transition, Journal of Applied Mechanics. 48 (1981) 297. doi:10.1115/1.3157612.

[175] H. Ziegler, A Modification of Prager's hardening rule, Quarterly of Applied Mathematics. 17 (1959) 55–65.

[176] M. Noban, H. Jahed, A Cyclic Plasticity Model for Multiaxial Behavior of Magnesium, in: The 10th International Conference on Multiaxial Fatigue & Fracture, Kyoto, Japan, 2013.

[177] M. Noban, H. Jahed, Modeling the Cyclic Plasticity Behavior of Wrought Mg Alloys, in: 9th International Conference on Magnesium Alloys and Their Applications, Vancouver, 2012.

[178] Abaqus, Version 6.14-2 Documentation, Dassault Systèmes Simulia Corp., Providence, RI, USA, 2014.

[179] T. Belytschko, W. Liu, B. Moran, Nonlinear finite elements for continua and structures,

2000. doi:10.1016/S0065-230X(09)04001-9.

[180] M. Vrh, M. Halilovič, B. Štok, Improved explicit integration in plasticity, International Journal for Numerical Methods in Engineering. 81 (2010) 910–938. doi:10.1002/nme.2737.

[181] M.G. Lee, D. Kim, C. Kim, M.L. Wenner, R.H. Wagoner, K. Chung, A practical two-surface plasticity model and its application to spring-back prediction, International Journal of Plasticity. 23 (2007) 1189–1212. doi:10.1016/j.ijplas.2006.10.011.

[182] H. Qiao, S.R. Agnew, P.D. Wu, Modeling twinning and detwinning behavior of Mg alloy ZK60A during monotonic and cyclic loading, International Journal of Plasticity. 65 (2015) 61–84. doi:10.1016/j.ijplas.2014.08.010.

[183] Y.N. Wang, J.C. Huang, The role of twinning and untwinning in yielding behavior in hot-extruded Mg-Al-Zn alloy, Acta Materialia. 55 (2007) 897–905. doi:10.1016/j.actamat.2006.09.010.

[184] Y. Jiang, P. Kurath, A theoretical evaluation of plasticity hardening algorithms for nonproportional loadings, Acta Mechanica. 118 (1996) 213–234. doi:10.1007/BF01410518.

Appendix A

Flowchart for the numerical implementation of the proposed plasticity model

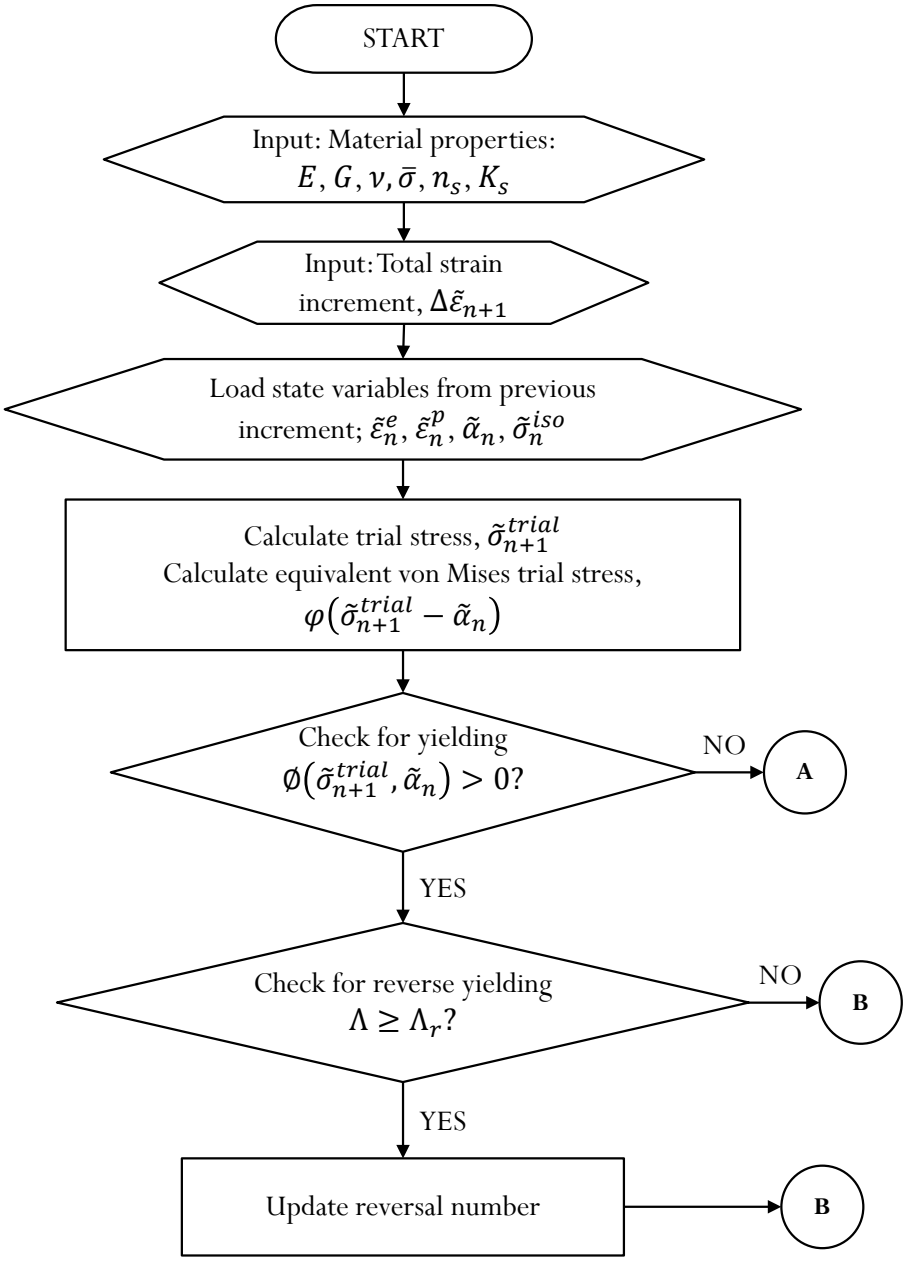

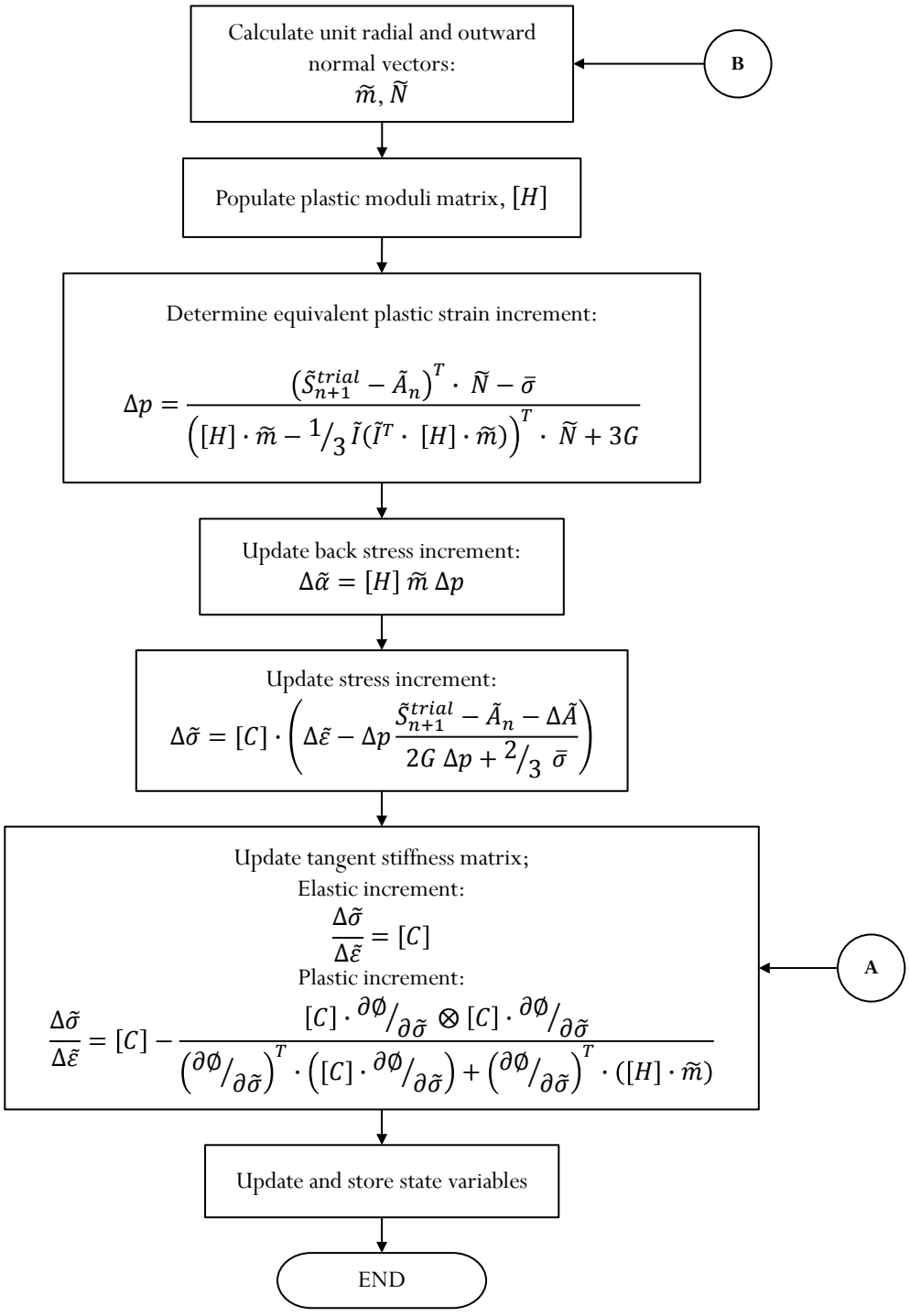

Figure A.1 Flowchart for the numerical implementation of the proposed cyclic plasticity model in UMAT.